nature portfolio

https://doi.org/10.1038/s41586-022-05296-7

Supplementary information

Pivotal role of reversible NiO_6 geometric conversion in oxygen evolution

In the format provided by the authors and unedited

Supplementary Materials for

Pivotal role of reversible NiO_6 geometric conversion in oxygen evolution

Authors: Xiaopeng Wang[1], Shibo Xi[2*], Pengru Huang[1,3], Yonghua Du[4], Haoyin Zhong[1], Qing Wang[1], Armando Borgna[2], Yong-Wei Zhang[5], Zhenbo Wang[6], Hao Wang[7*], Zhi Gen Yu[5*], Wee Siang Vincent Lee[1*] and Junmin Xue[1*]

Affiliations:

[1] Department of Materials Science and Engineering, National University of Singapore, Singapore, 117575.

[2] Institute of Chemical and Engineering Sciences, Agency for Science, Technology and Research, Singapore, 627833.

[3] Guangxi Collaborative Innovation Center of Structure and Property for New Energy, Guangxi Key Laboratory of Information Materials, School of Material Science and Engineering, Guilin University of Electronic Technology, Guilin, 541000, China.

[4] National Synchrotron Light Source II, Brookhaven National Laboratory, Upton, New York, USA, 11973.

[5] Institute of High Performance Computing, Agency for Science, Technology and Research, Singapore, 138632.

[6] School of Chemistry and Chemical Engineering, Harbin Institute of Technology, Heilongjiang Sheng, China, 150006.

[7] Department of Mechanical Engineering, National University of Singapore, Singapore, 117575.

*Correspondence to: msexuejm@nus.edu.sg (Junmin Xue); xi_shibo@ices.a-star.edu.sg (Shibo Xi); yuzg@ihpc.a-star.edu.sg (Zhi Gen Yu); mseleew@nus.edu.sg (Wee Siang Vincent Lee); mpewhao@nus.edu.sg (Hao Wang);

Contents

Materials and Methods

Sample preparations

NR-NiOOH, NiFe LDH, and traditional $Ni(OH)_2$ samples were prepared using the following methods:

1. Preparation of NR-NiOOH electrode on carbon cloth. **Electrodeposition of Ni on carbon cloth**. Firstly, the carbon cloth (CC) was heat-treated at 500 ºC for 30 minutes in air. Then, Ni was coated on CC *via* electrodeposition, with CC as the working electrode and graphite paper as the counter electrode, respectively. The solution used in the electrodeposition contained 0.15 M $NiSO_4$ and 0.6 M H_3BO_4. Then, electrodeposition was conducted under a constant current of -10 mA cm^{-2} for 1 hour. After electrodeposition, the sample was washed using DI water and dried at 60 ºC for 4 hours in air. **Formation of NiS_2.** The as-obtained Ni-coated CC sample was then heat-treated with 0.1 g sulfur at 400˚C under N_2 atmosphere for 1 hour. After cooling down to room temperature, the sample was washed with DI water, and then it was dried at 80 ˚C for 1 hour. **Electro-oxidation of NiS_2 in 1 M KOH solution to form NR-NiOOH**. Electro-oxidation was conducted using a three-electrode configuration, with NiS_2 (grown onto CC), Pt, and Hg/HgO electrode as the working electrode, counter electrode, and reference electrode, respectively, under a constant current density of 10 mA cm^{-2} for about 8 hours. After the electro-oxidation, NR-NiOOH on CC was obtained. According to our previous work, very weak S signal can be observed in the sample (*1*).

2. Coating of NR-NiOOH on FTO (Fluorine-doped Tin Oxide) glass. **Collection of NR-NiOOH powder.** In order to collect NR-NiOOH powder, NR-NiOOH on CC sample was subjected to sonication for 5 minutes in DI water. The sonication and washing process were repeated 9 times. The solution used during the solution was then dried at 60 ˚C for 10 hours. **Coating NR-NiOOH on FTO.** The collected black powders were coated onto FTO using Nafion as the binder.

3. Preparation of NiFe LDH electrode. CC was heat-treated at 500˚C for 1 hour in air to increase its wettability. Then, DI water was used to clean the CC several times. After which, the cleaned CC was immersed into 30 mL aqueous solution containing 4 mmol $Ni(NO_3)_2 \cdot 6H_2O$, 1 mmol $Fe(NO_3)_3$, and 10 mmol HMT. Then, the aqueous solution and CC were transferred into a

Teflon-lined stainless-steel autoclave and the system was maintained at 100˚C for 10 hours. Finally, the prepared samples were washed using DI water, and dried at 60˚C for 6 hours in air.

4. Preparation of traditional $Ni(OH)_2$ on carbon cloth. To minimize the effects of Fe impurities on the structure and OER activity of NiOOH, all glass components were cleaned with H_2SO_4 before conducting the experiment. At the same time, the commercial concentrated KOH solution was used to prepare the KOH electrolyte. CC was heat-treated at 500˚C for 1 hour in the air to increase its wettability. Then, DI water was used to clean the CC several times. After which, the cleaned CC was immersed into 30 mL aqueous solution containing 4 mmol $Ni(NO_3)_2 \cdot 6H_2O$ (99.999%) and 10 mmol HMT. Then, the aqueous solution and CC were transferred into a Teflon-lined stainless-steel autoclave, and the system was maintained at 100˚C for 10 hours. The prepared samples were washed with DI water, and then they were dried at 60˚C for 6 hours in air. The prepared sample was then analysed using inductively coupled plasma (ICP) analysis to determine the Fe content in the samples. The result showed that Fe contents in the samples before and after OER were lower than 0.1 wt%. This result suggests that the effect of Fe on the structure and measured OER activity and can be ignored.

5. Preparation of NiCr, NiMn, NiV, NiCo, NiCu, CoMn, CoMn and CoV LDH. These samples were prepared using methods shown in NiFe LDH. The raw materials were $Ni(NO_3)_2 \cdot 6H_2O$, $Mn(NO_3)_2 \cdot 4H_2O$, VCl_3, $CoCl_2 \cdot 6H_2O$ and $Cu(NO_3)_2 \cdot 3H_2O$.

OER measurements

Electrochemical measurements were performed using a three-electrode system, with the as-prepared sample as the working electrode, Hg/HgO as the reference electrode, and Pt as the counter electrode. All the reference electrodes used in this experiment are calibrated *vs.* reversible hydrogen electrode (RHE), based on our previously reported methods (*1*). The electrochemical workstation used for these electrochemical measurements was VMP3 (Bio-Logic Inc), with built-in electrochemical impedance spectroscopy (EIS) analyser. The EIS spectra was conducted at 0V (*vs.* open circuit voltage), and the frequency ranged from 100 kHz to 100 Hz. The electrochemical cell used in the OER measurement was presented in Fig. S4a,

whereby it involved a thermostatic bath with cooling water to keep the temperature constant. Quartz glass with high light transmittance was used as the optical window.

CA measurement. In the dark situation, all electrochemical measurements are conducted in a dark box. A solar simulator (NBeT Solar-500, 300 W) was used as the light source as to match AM 1.5G. The intensity of the light irradiated on the electrocatalyst was 100 mW cm^{-2} as calibrated by a light power meter (Newport 843-R). Before evaluating the OER activity, all samples are subjected to chronopotentiometry measurements at a current density of 10 mA cm^{-2} under dark for 24 hours to ensure the complete oxidation of Ni^{2+} to Ni^{3+}.

LSV measurement. Since the potential range of oxygen evolution is close to that of the redox regions of nickel (Ni^{2+} to Ni^{3+}, 1.1 V ~ 1.34 V *vs.* RHE), the measured OER current value may consist of redox current (*I*). Thus, two electrochemical steps are employed to minimize the impact of the redox reaction of nickel on the measured OER value. First, prior to the LSV measurement, chronoamperometry measurements are conducted for both samples that are subjected to and without light irradiation, at a constant potential of 1.42 V for 24 hours under light or in the dark, respectively. This process is to ensure the complete oxidation of NR-$Ni(OH)_2$ to NR-NiOOH. Secondly, during the LSV measurement, to ensure the measurement of OER before Ni redox regions, LSV is conducted by sweeping negatively from 1.55 V to 1.1 V *vs.* RHE.

ECSA measurement. During the electrochemical surface area (ECSA) experiment, the measurement window was selected between 1.00 V to 1.15 V vs RHE, whereby neither the electrode nor the electrolyte undergoes the electrochemical process. 90% *iR* correction (R = 1.38 ohm, the resistance of the catalytic material) was used to correct the measured potentials. The scan rates used for the ECSA measurement were 10 mV/s, 20 mV/s, 30 mV/s, 40 mV/s, 50 mV/s, 60 mV/s, 70 mV/s, 80 mV/s, 90 mV/s, 100 mV/s, 200 mV/s and 300 mV/s. For each scan rate, several consecutive CVs were measured until no changes were observed, and the last CV result was used for further data analysis. The ideal capacitor model (Y = bX, where Y is the current and X is the scan rate) was used to determine the double layer capacitance (C_{DL}), whereby a fitting value of 2.47 mF cm^{-2} (R-factor ~ 0.9996) was achieved. Then, the ESCA was determined based on the equation ECSA = C_{DL}/C_s (C_s is the specific capacitance with the widely used value 0.04 mF cm^{-2}).

Photocatalytic measurements

10 mg NR-NiOOH powder was suspended in 20 mL phosphate buffer solution (0.1 M, pH =7) containing 0.1 M $K_2S_2O_8$. Prior to the photocatalytic experiment, the suspension was bubbled with nitrogen gas (10.0 mL/min) for 10 hours in an air-tight tube to remove all dissolved O_2 in the solution. When all traces of oxygen were removed, the suspension was illuminated with a light source, supplied by a 300 W Xenon lamp equipped with AM 1.5 filter (NBeT, Solar-500, Beijing). The intensity of the light was 100 mW cm^{-2} calibrated by a light power meter (Newport 843-R). It is worth noting that the suspension was stirred at a rate of 800 r/min under illumination. Then, the gas product was manually collected and subsequently analyzed by gas chromatography.

Operando X-ray absorption fine structure

The *operando* and *ex-situ* Ni *K*-edge X-ray absorption fine structure (XAFS) and high-resolution X-ray absorption fine structure (HR-XAFS) data were collected at the XAFCA beamline of Singapore Synchrotron Light Source (SSLS) under transmission mode. The device for *operando* XAFS is shown as the Fig. S9b, using Hg/HgO electrode as the reference electrode and Pt as the counter electrode. The storage ring of SSLS was running at 0.7 GeV with an electron current of 200 mA. Energy calibrations were carried out using standard Ni foil. Athena was used for the energy calibration, background removal, and Fourier Transform (FT). Detailed parameters are shown below:

FT of the EXAFS:

Energy range: 30-450 eV above absorption edge.

Window function: Hanning

K range: 3-11 $Å^{-1}$.

K-weight: 3

Fitting parameters:

Method: least-squares

Space: R

K range: 3-11 $Å^{-1}$

R rang: 1-3 Å

Software: Artemis

Initial structure: standard β-$Ni(OH)_2$.

Theoretical scattering path calculation code: FEFF6

$S0^2$: 0.7, obtained from EXAFS fitting of standard Ni Foil.

E_0 used to convert from E space to K space: 8344.9 eV for NR-NiOOH dark; 8343.5 eV for NR-NiOOH light-c NR-NiOOH sample.

K weight during EXAFS fitting: 1,2,3

K weight used in plot: 3

Theoretical Calculations

1. Computational method. All calculations were carried out using the density functional theory (DFT) with the generalized Perdew-Burke-Ernzerhof (PBE) and DFT+U (U_{eff}=U-J=5.3), and the projector augmented-wave (PAW) pseudopotential plane wave method as implemented in the VASP code. For the PAW pseudopotential, we included $3d^7 4s^1$, $3d^8 4s^2$, $2s^2 2p^4$, and $1s^1$ as valence electrons for Fe, Ni, O, and H atoms, respectively. In this study, PBE wavefunctions and eigenvalues of bulk NiOOH, NR-NiOOH, and NiFe LDH were used as the inputs for the G_0W_0 calculations. **Bulk NiOOH.** A 12×12×10 Monkhorst-Pack (MP) k-point grid was used for NiOOH unitcell geometry optimization calculations. Good convergence was obtained with these parameters, and the total energy was converged to 1×10^{-6} eV per atom. Energy convergence with respect to the plane wave cutoff was tested by varying this setting between 300 and 600 eV considering the electron spin polarization. Convergence to within 10 meV was achieved with a cutoff energy of 500 eV for NiOOH unitcell. **NR-NiOOH.** The optimized bulk NiOOH layer was used to build monolayer NiOOH. Based on the optimized NiOOH monolayer, NR-NiOOH model was constructed by cutting along *x*-direction, with OH termination. This model was further optimized by constraining the lattice constants. NiFe, NiCr, NiMn, NiV, NiCo, NiCu LDH models were constructed replacing one Ni using one metal atom (M=Fe, Cr, Mn, V, Co and Cu) in NR-NiOOH, and geometry optimized by constraining the lattice constants.

2. Calculation of LOM and COM in NR-NiOOH. We carried out calculations with the van der Waals (vdW) correction by employing the optPBE-vdW functional.

LOM:

$\Delta G_{L1} = \Delta G_{[O\text{-}O]} - \Delta G_{[OH^*+O^*]} - eU + \Delta G_{pH}$

$\Delta G_{L2} = \Delta G_{[OO^*+OH^*]} - \Delta G_{[O\text{-}O]} - eU + \Delta G_{pH}$

$\Delta G_{L3} = 4.92\ eV - \Delta G_{[OO^*+OH^*]} + \Delta G_{[OH^*+OH^*]} - eU + \Delta G_{pH}$

$\Delta G_{L4} = \Delta G_{[OH^*+O^*]} - \Delta G_{[OH^*+OH^*]} - eU + \Delta G_{pH}$

COM:

$\Delta G_{C1} = \Delta G_{[O^*+O^*]} - \Delta G_{[OH^*+O^*]} - eU + \Delta G_{pH}$

$\Delta Gc_2 = \Delta G_{[O\text{-}O]} - \Delta G_{[O^*+O^*]}$ **(light dominated process)**

$\Delta G_{C3} = \Delta G_{[OO^*+OH^*]} - \Delta G_{[O\text{-}O]} - eU + \Delta G_{pH}$

$\Delta G_{C4} = 4.92\ eV - \Delta G_{[OO^*+OH^*]} + \Delta G_{[OH^*+OH^*]} - eU + \Delta G_{pH}$

$\Delta G_{C5} = \Delta G_{[OH^*+O^*]} - \Delta G_{[OH^*+OH^*]} - eU + \Delta G_{pH}$

To better describe the actual OER process, we have calculated free energies considering the solvent effect based on U = 0 V, 1.23 V and the lowest bias potential vs RHE. The solvent effect was considered using the implicit solvation model implemented in the vasp code (*2*). The detail calculation results are summarized as shown in Table S6. All coordinates of the simulated slabs with and without the adsorbates (POSCAR) have been provided in the Appendix.

3. The energy barrier of geometry conversion from octahedral to square planar. The reaction paths of geometry conversion were calculated by means of the Nudged Elastic Band (NEB) method. The calculated energy barrier of octahedral to square planar is shown in Fig. S22. To realize the geometry conversion from octahedron to square planar, two neighboring (O-O) coupling will have to occur. For this calculation, two possible pathways were considered, i.e., these two (O-O) couplings occur asynchronously or simultaneously.

Supplementary Discussion

Discussion on the redox activities in conventional AEM and LOM

The metal bands near the Fermi level act as the redox centres for the OER process and such electron transfer process is classified as adsorbate evolution mechanism (AEM). The conventional AEM follows the pathway of OH^*, O^*, OOH^*, and O_2. The redox activities in this proposed OER mechanism were analyzed by deciphering the electron transfer process, as shown in Fig. S3a. In the deprotonation step (from OH^- to O^{2-}), the cleavage of oxygen-hydrogen bond is accompanied by one electron and proton transfer. The electron transfer from metal orbitals to the external circuit leads to an increase in metal valence. In the OOH^- formation process, the adsorption of OH^- from the electrolyte leads to the transfer of one electron and proton. To fulfill the 8-electron configuration of oxygen, two inner electrons must be transferred from oxygen to metal, and this decreases the metal valence. In the subsequent deprotonation step (from OOH^- to OO^{2-}), the cleavage of oxygen-hydrogen chemical bond leads to a concerted electron and proton transfer. In this process, the electron is transferred from the metal orbitals to the external circuit, whereby the valence of Ni increases. In the oxygen evolution step, two types of electron transfer can occur: Removal of one electron from the metal orbitals to the external circuit, and the removal of two inner electrons from oxygen orbitals to the metal orbitals. Hence, during this step, the valence of the metal decreases. Consequently, it can be understood that metal acts solely as the redox center during the entire OER process.

The oxygen bands near the Fermi level act as the redox centres for the OER process and this electron transfer process is classified as lattice oxygen oxidation mechanism (LOM). Currently, it is widely known that LOM is a type of oxygen redox reaction. The sole oxygen redox activities within LOM were verified by researchers in the study of perovskite, using *operando* oxygen *K*-edge and metal *L*-edge X-ray absorption spectra (*3*). The sole oxygen redox activities could be further understood based on the electron transfer process. As shown in Fig. S3b, conventional LOM process involves deprotonation, O-O coupling, and O_2 release. During the deprotonation step, hydrogen-oxygen chemical bond is firstly broken, and then one proton is removed from the adsorbed OH^- group. Concurrently, the adsorbed OH^- will change into O^{2-}.

In the subsequent electron transfer process, O^{2-} will transform into O^{-}, to realize O-O coupling. It is well known the O-O coupling step is a chemical process that proceeds by hybridizing the non-bonding oxygen states in the neighboring O^{-}. As a result, the electron configuration of O^{-} is less than 8 which is a type of oxidized oxygen state. Consequently, as O^{2-} is converted to O^{-}, one electron is transferred from the oxygen orbitals of O^{2-} into the external circuit, whereby oxygen acts as the redox center. During the oxygen evolution step, two electrons have to be removed from the oxygen orbitals of $(O\text{-}O)^{2-}$ to achieve the electronic structure of O_2. Consequently, oxygen acts as the redox center during this process. As such, according to our analyses, a two-electron transfer from oxygen orbitals occurs during the deprotonation step, while the other two-electron transfer from oxygen orbitals occurs during the generation of O_2, which sums up to the four-electron transfer process during OER. Thus, based on this discussion, LOM is a type of oxygen redox reaction. At the same time, the sole oxygen redox activities within LOM.

In conventional OER routes, the types of electronic states around the Fermi level in electrocatalysts are fixed. Hence, as a result of this constraint, the OER mechanisms reported in previous studies proceed either solely via a metal redox chemistry (AEM, with metal bands around the Fermi level) or an oxygen redox chemistry (LOM, with oxygen bands around the Fermi level).

Discussion on the bottlenecks of conventional AEM and LOM

In AEM routes, the existence of potential-limiting step (PLS), *i.e.*, O-O bonding, can cause the overall process to become sluggish (*1, 4*). Hence, O-O bonding step in the AEM route is often considered as one of the main culprits behind the poor OER performance exhibited by AEM-based electrocatalyst. Unlike AEM, LOM involves a direct oxygen-oxygen (O-O) bond, which can bypass the limitation of AEM, and this highlights the merit of LOM as compared to AEM (*5*). When the non-bonding oxygen states become accessible, the OER process would proceed *via* LOM pathway (*4*) (Fig. S2). Even though LOM is able to avoid the potential-limiting step of AEM, the deprotonation step during LOM is still an energy-demanding process, and therefore it is considered as the PLS for LOM (*4*). This is largely due to the localization of the

electrons in the non-bonding hydroxide states, which requires more energy for the electron transfer, and consequently increases the deprotonation energy. Hence, the electron transfer efficiencies of both AEM and LOM are still fundamentally plagued by their respective PLS, which may be considered as one of the bottlenecks in the OER electrocatalyst development.

Discussion on possible reasons for the enhanced OER activity triggered by light

There are several possible reasons for this unique phenomenon, *i. e.* (1) the influx of photon helps to decrease the ohmic resistance, (2) the generation of holes by light that become available for OER, and (3) light induced conversion of OER routes. To investigate the feasibility of the first possibility, electrochemical impedance spectroscopy (EIS) test was conducted for both samples subjected to and without light irradiation. According to Fig. S4c, the resistances of these two samples were nearly identical, which excludes the likelihood of lower catalyst resistance due to photon influx. To investigate the feasibility of second possibility, OER photocatalytic behavior of NR-NiOOH was analyzed by determining the potential of the light-induced holes. Generally, the requirements of the overall water-splitting photocatalysts are stringent, and no response can be obtained if the conditions of either oxygen evolution or hydrogen evolution reaction are not met. Performing trial oxygen evolution reaction in the presence of sacrificial electron acceptors is one way to assess the suitability of the band position of a specific composition to act as an OER photocatalyst. The potential of the holes was examined using gas chromatography with $K_2S_2O_8$ as the electron acceptor, and no oxygen was detected within 2.5 hours of operation (Fig. S4d). This result indicates that the enhanced OER activity in NR-NiOOH is not attributed to the generation of light-induced holes. At the same time, a repeated light on/off experiment under pro-longed operation was demonstrated in our work (Fig. S4b). Interestingly, we found that the light-induced behavior, *i.e.*, the enhancement in the current densities under light irradiation and reduction in the current densities once the light was switched off, is highly repeatable. Such a repeatable light-induced behavior observed in our work is unlikely to be due to crystal growth, since crystal growth is regarded to be an irreversible process. To summarize the novelty of our work, we have presented the key idea flow of our work in Fig. S7 and 8, whereby we have demonstrated a

new OER mechanism involving switchable metal and oxygen redox activities under light irradiation.

To elucidate the underlying mechanism of the light-triggered OER performance enhancement in our work, the structural geometry under light irradiation was investigated by *operando* XAFS (Fig. 3a and b). According to our experimental result, there was a significant reduction in the Ni valence state, which is different from conventional OER process. Further analyses indicated that this reduction in Ni valence state was caused by the reversible geometrical conversion from octahedron to square planar under light irradiation, as identified according to the pre-edge and white line in XAFS and FT-EXAFS (Fig. S10 to 12). To the best of our knowledge, this is a new finding in OER electrocatalyst research which has yet to be reported. In addition, based on the collective results obtained from TMA^+ probe combining XAFS, ^{18}O isotope measurement, and calculations, as NiOOH converted to square planar geometry, there was a change in the redox center from metal to oxygen (Fig. 3c to d and Fig. S14 to 19). As such, a new OER mechanism-coupled oxygen mechanism that proceeds *via* an optimized energy pathway was proposed in this work (Fig. 4). In this optimized energy pathway, deprotonation occurred at the metal bands, while O-O coupling process occurred at the oxygen states. To further explore the underlying science of COM, the electronic structures of NR-NiOOH and bulk NiOOH were analyzed (Fig. S13 and 32). It was demonstrated that only when there was a non-overlapping region arising from the partial overlapping of d_{z^2} orbitals with a_{1g}^* bands, electron could then be transferred from (M-O) to d_{z^2} orbitals to complete the as-proposed COM (Fig. 5a). Interestingly, we found that COM can also be extended to other materials such as NiFeOOH, NiCrOOH, NiMnOOH, NiVOOH, NiCoOOH, NiCuOOH, *etc.*, and Co-based oxyhydroxide, *i.e.*, CoMnOOH and CoVOOH (Fig. S38 to 39).

Discussion on the experiments in the revelation of COM

Two types of redox activities, *i.e.*, metal redox activities with electron removal from metal electronic states and oxygen redox activities with electron removal from non-bonding oxygen states, are possible during the oxygen evolution catalytic reaction. Generally, the removal of electrons from the metal orbitals is accompanied by the variations in the metal valence, which

can be effectively identified using *operando* metal *K*-edge XAFS, *etc*. As the electrons are removed from the oxygen orbitals, oxygen will be oxidized, and this can be subsequently stabilized *via* the chemical oxygen-oxygen coupling. Since the oxygen-oxygen coupling bond is formed through the hybridization of non-bonding oxygen states in the neighboring oxygen atoms, this process requires the participation of lattice oxygen atoms. Thus, the emergence of oxidized oxygen states and participation of lattice oxygen atoms are the characteristic features of oxygen redox activities.

The flow chart depicting our experimental approach is shown in Fig. S8. To determine the involvement of metal redox activities in our new mechanism, we firstly conducted *operando* Ni *K*-edge XANES. According to our experimental results, there was a significant reduction in the Ni valence state under light irradiation (Fig. 3a). As the current stabilized, a Ni valence of about 2.2 was recorded, which indicates the co-existence of Ni^{2+} and Ni^{3+} (Fig. 3b). This is greatly different from the traditional OER process, whereby a co-existence of Ni^{3+} and Ni^{4+} is usually observed during the catalytic reaction. Meanwhile, based on the pre-edge and white line in XANES and FT-EXAFS, the variation in Ni valence state was caused by the reversible geometrical conversion from octahedron to square planar under light irradiation (Fig. S10 to 12). According to the molecular orbital diagram, such a geometry conversion is realized by the transfer of electron from (M-O) to d_{z^2} orbital induced by light (Fig. S12c). Then, the geometry of square planar was studied. Based on the calculations, as the sample converted to the square planar structure, its electronic states around the Fermi level will change to the oxygen orbital, and this implies the existence of oxygen redox activity during the OER process (Fig. S14 to 15). Next, the oxidized oxygen states were confirmed by using TMA^+ probe combined with XAFS, while oxygen-oxygen coupling was identified using isotope technology (Fig. 3c and d). Thus, according to the collective results, oxygen evolution step is based on oxygen redox activities, and this process involves a two-electron transfer mechanism.

To achieve the oxidized oxygen states, electron must transfer from oxygen orbitals to the external circuit (oxygen redox) or metal orbitals during the deprotonation step. Since metal redox activities were also identified in this OER process, this type of electron transfer is

unlikely to be due to oxygen redox. Hence, the oxidized oxygen is realized through electron transfer from oxygen to metal orbitals, which is intrinsically the light-induced electron transfer from (M-O) to d_{z^2} orbital. To further analyze the deprotonation step, pH dependence was employed (Fig. S21). Based on the experimental results, deprotonation is a non-concerted proton-electron transfer process, which involves a proton transfer and a subsequent electron transfer from (M-O) to d_{z^2} orbital. Since the deprotonation step involves the light-induced geometry conversion from octahedron to square planar, the geometric conversion back to octahedron from square planar must be satisfied during the OH^- refilling process. To achieve the geometric conversion back to octahedron from square planar, electrons that are stored in the d_{z^2} orbital must be released into the external circuit where metal acts as the redox center. Moreover, since two OH^- ions that are participating in the O_2 generation process are within the neighboring square planar unit cells, these two square planar unit cells can be converted into octahedral unit cells per O_2 generated. Such a step involves a two-electron transfer.

According to the collective results, the proposed light-induced OER process with switchable metal and oxygen redox centers is illustrated in Fig. 4. In our OER route, three electron transfer processes are involved: (1) light-induced electron transfer from (M-O) to d_{z^2} orbital, (2) electron transfer from (O-O) coupling bands to the external circuit (oxygen redox), and (3) electron transfer from the d_{z^2} orbital to the external circuit (metal redox). Thus, our OER route involves both oxygen and metal redox reactions, which is termed as coupled oxygen evolution mechanism (COM). Our OER process can be summarized with these sequential steps: (1) Proton transfer occurring in octahedral NiO_6. (2) Under light irradiation, there is a geometric conversion of octahedral NiO_6 to square planar NiO_4 induced by the photon. (3) The hybridization of the formed ONB leads to oxygen-oxygen coupling to form an oxygen band. (4) Release of oxygen resulting in OH^- vacancy sites. (5) Refilling of these vacancy sites with OH^-. (6) As a result of the OH^- refilling process, there is a concomitant geometric conversion of the square planar NiO_4 to octahedral NiO_6 configuration.

Discussion on experiment to identify square planar

In our work, the square planar geometry is verified in view of electronic states, Ni-O coordination numbers, and Ni-O bond length.

1), Electronic states

As shown in orbital diagram (Fig. S10a), when the electronic state of Ni^{3+} changes into low spin Ni^{2+}, d_{z^2} orbital will be fully occupied while $d_{x^2-y^2}$ orbital will be empty, which subsequently becomes a localized state. To investigate Ni^{2+} in NR-NiOOH under light irradiation, *operando* XANES (X-ray absorption fine structure) and HR-XANES (high-resolution X-ray absorption fine structure) were employed (Fig 3a and Fig. S10c). The pre-edge peak intensity (8330 to 8340 eV, corresponding to the localized $d_{x^2-y^2}$ orbital) of the sample under light condition significantly increases, as compared to that of NR-NiOOH in the dark condition. This result indicates that the localization of $d_{x^2-y^2}$ orbital, which implies the formation of low spin Ni^{2+}. At the same time, the low spin Ni^{2+} electronic configuration follows a square planar geometry due to its high crystal field splitting energy between d_{z^2} and $d_{x^2-y^2}$ orbitals, where its 4*p* orbitals *i.e.*, p_x, p_y and p_z, become more splitting as compared with that of Ni^{3+} (Fig. S10a). *Operando* XANES and HR-XANES results show that the white line (8340 to 8360 eV, corresponding to the Ni 4*p* orbitals) of NR-NiOOH under light irradiation becomes broader with lower intensity as compared to that of NR-NiOOH in the dark condition, which suggests the increased splitting of Ni 4*p* orbitals (Fig. S10 and 11). These results clearly indicates that Ni^{2+} in NR-NiOOH possessed a low spin Ni^{2+} configuration when subjected to light irradiation.

2) Coordination numbers

It is well known that Ni-O coordination numbers will be reduced from six to four when the geometry of NiO_6 changes from octahedron to square planar. Hence, the variation of coordination numbers is a very powerful evidence to identify the square planar geometry. To estimate the average Ni coordination numbers of light sample (light-c in Fig. 3a), it is necessary to determine the ratios of Ni^{2+}/Ni^{3+} in the sample by analyzing the Ni valence. Here, the valence

of NR-NiOOH is around 3+ (dark in Fig. 3a) and the valence of low spin Ni^{2+} is set as 2+. Given that the measured Ni valence of light sample is about 2.2, the ratio of Ni^{2+}/Ni^{3+} in the light sample is estimated to be 8:2. If the Ni^{2+} in NR-NiOOH is in low spin Ni^{2+} configuration, the average Ni coordination numbers of light sample could be calculated as following: 0.2*5.1+0.8*4 = 4.22 (the average Ni coordination numbers of NR-NiOOH under dark is 5.1 in Table S5). This value is in the range of the experiment value 3.8±0.6 (Table S5). This clearly indicates that Ni^{2+} in NR-NiOOH possessed a low spin Ni^{2+} configuration when subjected to light irradiation.

3) Ni-O bond length

In our work, the bond length variations of NR-NiOOH sample were studied using calculations and FT-EXAFS measurement as the geometry changes from octahedron to square planar. Based on the calculations, two neighboring O-O coupling state is the most stable square planar geometry model, which was used to analyze the variations of bond length (Fig. S11d). It shows that the bond length of square planar unit cell is slightly small than that of octahedral unit cell, while the Ni-O bond length adjacent to O-O coupling becomes much larger than that of octahedral unit cell. The slight decrease in the bond length of the square planar unit cell is due to the increased Ni-O bonding energy. Based on ligand field theory, when the geometry is converted from octahedral to square planar, the crystal field splitting energy would greatly increase, resulting in a stronger Ni-O bonding. The increase of bond length is related to the hybridization of non-bonding oxygen states, which would result in the extension of Ni-O bond length for the subsequent O-O coupling. Next, the average of bond length in octahedral and square planar NR-NiOOH models are calculated. It shows that the calculated value of square planar is 1.953 Å, which is 0.023 Å lager than that of octahedral (1.930 Å). At the same time, the *operando* FT-EXAFS results show that under light irradiation the Ni-O bond length becomes slightly larger (Fig. S11b). The consistent variations of bond length in calculation and experiment results clearly indicates that Ni^{2+} in NR-NiOOH possessed a low spin Ni^{2+} configuration when subjected to light irradiation.

<u>Discussion on the accessibility of COM route in NR-NiOOH</u>

In contrast to the conventional OER process, the (O-O) coupling step in our proposed COM pathway was realized *via* photon-induced geometry conversion from octahedron to square planar. To realize the geometry conversion from octahedron to square planar, two neighboring (O-O) coupling will have to occur. In this calculation, two possible pathways were considered, *i.e.,* these two (O-O) couplings can occur either asynchronously or simultaneously. The simulation results showed that the calculated kinetic barrier based on asynchronous pathway was 1.741 eV, which is smaller than that of simultaneous pathway (2.148 eV) (Fig. S22 c and d). Since the kinetic barrier based on asynchronous pathway is lower than that of simultaneous pathway, the asynchronous pathway was considered, which means that a kinetic energy barrier of 1.741 eV must be overcome to achieve geometry conversion. In our proposed COM route, the geometry conversion from octahedron to square planar was triggered by light, which was realized by the photon-induced ligand-to-metal charge transfer (LMCT), electron transfer from (M-O) (ligand like character) to the non-overlapping region of d_{z^2} orbitals with a_{1g}^* band (metal like character), as shown in in Fig. 5a. As shown in our PDOS results, the energy required for this type of electron transfer was 1.85 eV, which is larger than the energy barrier (1.7412 eV) of the geometry conversion from octahedron to square planar (Fig. S13d). This means that such a geometry conversion is feasible as long as the photon can provide sufficient energy to trigger the electron transfer from (M-O) to the non-overlapping region of d_{z^2} orbitals with a_{1g}^* band (despite the high kinetic energy barrier).

The photon response measurement results show that the lowest wavelength to trigger COM is in the range of 750 nm to 800 nm (1.550 eV to 1.653 eV) (Fig. S23). In our work, a solar simulator (NBeT Solar-500, 300 W) was used as the light source to simulate AM 1.5G, and it could provide sufficient energy to trigger the electron transfer from (M-O) to the non-overlapping region of d_{z^2} orbitals with a_{1g}* band. To prove the ability of photon in overcoming the high kinetic energy barrier required for geometry conversion, various factors such as electronic states, Ni-O coordinates numbers and Ni-O bond length were considered by conducting *operando* XAFS measurement (Fig. 3a and Fig. S9 to S13). Hence, based on the theoretical and experimental results, we have shown that (O-O) coupling could be triggered by light irradiation, which indicates that our proposed COM route was accessible under light

conditions. The accessibility of COM route under light irradiations was further identified using operando XAFS, TMA^+ probe and isotope measurements (Fig. 3 c and d).

Discussion on the accessibility of AEM and LOM routes in NR-NiOOH

To determine the actual process, *i.e.*, O-O coupling via LOM or OOH formation *via* AEM, that is more favorable for our NR-NiOOH sample (dark), the kinetics of each process was considered. (O-O) coupling *via* the LOM pathway is a chemical process (potential independent), which is typically related to temperature. At room temperature, the hard limit for a surmountable barrier is 0.75 eV (*5*). Hence, for (O-O) coupling *via* LOM to proceed, it is necessary to fulfill both conditions; (1) $\Delta G_{[O\text{-}O]}$ must be smaller than $\Delta G_{[O^*]}$ and (2) the activation energy from $\Delta G_{[O^*]}$ to $\Delta G_{[O\text{-}O]}$ (E_a) must be smaller than 0.75 eV (*4*). To determine the accessibility of O-O coupling, we calculated the free energy of the two isometric intermediates of $\Delta G_{[O^*]}$ and $\Delta G_{[O\text{-}O]}$ (Fig. S22a). Based on the calculations, $\Delta G_{[O\text{-}O]}$ (0.158 eV) is larger than $\Delta G_{[O^*]}$, which indicates that O-O coupling was thermodynamically unfeasible. Furthermore, the energy barrier from $\Delta G_{[O^*]}$ to $\Delta G_{[O\text{-}O]}$ was 0.794 eV, which is higher than the activation energy limit for facile kinetics, *i.e.*, 0.75 eV (*5*). As such, based on these two conditions, O-O coupling is not accessible for NR-NiOOH without considering the light effect (LOM is inaccessible for NR-NiOOH). On the other hand, OOH formation is an electrochemical process, and the activation energy of OOH formation reduces with increasing applied potentials (*6*).

Thus, by considering the nature of OOH formation (potential dependent) with that of O-O coupling (potential independent), OOH formation will become more accessible in NR-NiOOH during OER without considering light effect. To further verify our conclusion, we have conducted TMA^+ probe and isotope measurement (Fig. 3c and d) and proved the proceeding of AEM route in our NR-NiOOH under dark conditions. Based on our experimental results, OER process can only proceed *via* the AEM route in NR-NiOOH under dark conditions, which is consistent with our DFT results that revealed O-O coupling is thermodynamically unfeasible. Thus, by considering the accessibility of O-O coupling, a more meaningful conclusion can be drawn, *i.e.*, O-O coupling is thermodynamically unfeasible in NR-NiOOH under dark

conditions, and OOH formation (AEM route) is more likely to occur, especially at high potentials.

Discussion on the Tafel slope

Theoretical Tafel slope can also be calculated based on the formula derived by Fletcher (*7*):

$$\frac{2.303RT}{\alpha F}$$

In this equation $\alpha = n_p + n_q\beta_f$, where n_p is defined as the number of electrons transferred prior to the rate-determining step, n_q is the number of electrons transferred during the rate-determining step, and β_f is the fundamental term describing the rate-determining step of a single electron transfer reaction. Here, we used OH^* adsorption step as the starting step and assumed the deprotonation step as the rate determining step. In our proposed COM, a two-electron transfer from d_{z^2} orbital to the external circuit occurs during the OH^* adsorption step, and another two-electron transfer from the (O-O) coupling bands are transferred to the external circuit during oxygen evolution step. Hence, n_p is 2 and n_p is 0. Based on these conditions, the Tafel slope value is 29.5.

In our work, the theoretical value agrees well with the measured Tafel slope value obtained from the sample under light irradiation, *i.e.*, 31 (Fig. S5d). Previous report has shown that the calculated Tafel slope in the case of high O^* surface coverage was 60 mV dec^{-1} when OOH^* is the rate-determining step (*8*). This value is in good agreement with the Tafel slope value obtained from the sample in dark condition, *i.e.*, 63 (Fig. S5d). These results clearly indicate that the rate determining step changes from the typical OOH^* formation to proton transfer when being subjected to light. This phenomenon is highly consistent with our proposed light induced OER mechanism as it switches from AEM to COM under light irradiation. The variations in the rate determining step under light can be further identified *via* TMAOH measurement. TMA^+ can block the formation of (O-O) coupling, which further inhibits the COM process. It shows that the Tafel slope of NR-NiOOH under light irradiation decreased from 31 mV dec^{-1} to 60 mV dec^{-1} after adding TMAOH, which indicates the reverting of the OER mechanism from COM back to AEM (Figure S18).

Discussion on the reaction order

Identification of the pH dependence of OER activity can provide insights into the reaction path, *i.e.*, a zero-order reaction shows a concerted electron and proton transfer, and a first-order reaction indicates a non-concerted electron and proton transfer (*9*). In conventional AEM route, proton and electron transfer is a concerted process, while in our proposed COM route, deprotonation step becomes a non-concerted process. The deprotonation step involves (1) the occurrence of proton transfer at the octahedron, and (2) subsequent light-induced electron transfer from (M-O) to d_{z^2} orbital. According to these discussions, as compared to NR-NiOOH under dark conditions, NR-NiOOH under light irradiation is expected to exhibit an OER activity with significant pH dependence. To verify this, OER performances of the samples under and without light irradiation were recorded at various pH values (Fig. S21). The experiment results shows that the reaction order of NR-NiOOH subjected to light irradiation is 0.36, which is three times larger than that under dark conditions, *i.e.*, 0.12. The significant increase in the reaction order indicates the presence of non-concerted proton and electron transfer during OER process for the sample under light irradiation.

Discussion on the inconsistencies in previous reports regarding the OER route of NiFe LDH

Even though this work reports for the first time the insight into light as the triggering factor in NiOOH-based materials in their adaption towards COM, it can also offer an explanation to the inconsistencies in previous reports regarding the observed OER route, *i. e.*, (O-O) coupling was found in NiFe LDH in some reports (*10-12*), while others reported that NiFe LDH exhibited AEM (*13*). Such contradictory observations may inevitably cast a veil of confusion in the research community, which in turn hinders the progression of OER catalyst development. According to our proposed light-induced COM conversion mechanism, light is a crucial factor for the switchable AEM-COM behavior exhibited by NiFe LDH. When considering all previous works that reported the (O-O) coupling NiFe LDH, these experiments were conducted under natural room lighting (*10-12*). Natural room lighting is able to provide photon with sufficient wavelength to trigger COM in NiFe LDH. Interestingly, for those contradicting works that reported the traditional AEM route for NiFe LDH using ^{18}O labelling technology,

these experiments were conducted in a dark situation (in the stagnant thin layer electrochemistry cell) (*13*). Thus, instead of idealizing a distinct OER route in NiFe LDH (which led to the rise of inconsistent reports), it is proven in this work that NiFe LDH possesses a switchable AEM-COM transition that can be triggered by a light stimulus. Hence, based on the collective findings in this work, light is a triggering factor for the switch in electron transfer mechanism from AEM to COM in $Ni(OH)_2$-based materials, resulting in their enhanced OER activities.

Discussion on the pro-long light induced activation process

The pro-longed light-induced LOM activation process is analysed using *operando* XAFS (Fig. 3). A gradual red shift in the absorption edge for the sample after the activation process is observed, with a broader peak located at around 8360 eV (Fig. 3a). Furthermore, the intensities of both Ni-O and Ni-Ni bonds gradually decrease (Fig. S11b). These indicates a gradual geometry conversion from octahedral to square planar during the activation process. It is worth noting that due to the three-dimensional nature of our material, certain parts of the NR-NiOOH may not be exposed to the light source, which inevitably requires a longer activation duration. However, for the NR-NiOOH that is grown on a FTO (fluorine-doped tin oxide) glass, the activation process still requires a long time (>50 s) (Fig. S41).

Discussions on COM in the electrolyzer stacks

In typical electrolyzer stacks, it is difficult to trigger light-induced COM due to the limited penetration of light. Recently, Zhang *et. al*. developed a redox decoupled water splitting device which can facilitate the COM mechanism in electrolyzer stacks (*14*). It enables the decoupling of HER and OER from the electrodes to spatially separated catalyst bed reactions *via* a pair of redox mediators. Oxygen evolution for this redox decoupled water splitting device occurs at the oxygen evolution tank, which can be made of transparent material. This option of choosing transparent material for the construction of the oxygen evolution tank implies the possibility of actualizing our proposed COM in this redox decoupled water splitting device. Furthermore, the electrocatalyst powders can be directly dispersed in the electrolyte without the need to coat on a substrate. This can then enable the effective utilization of light by the catalyst, and the photon

can then be used to effectively trigger COM. Thus, based on these considerations, the proposed COM can be actualized in this redox coupled water-splitting technology.

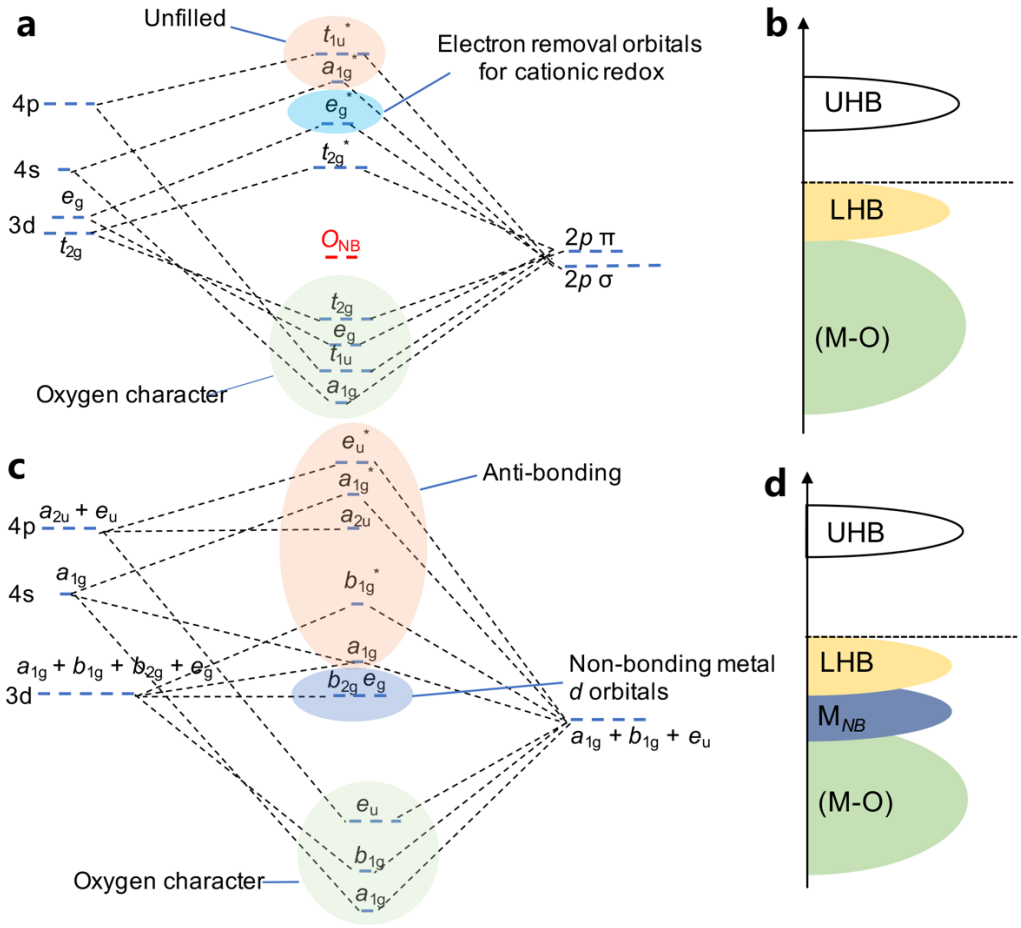

Fig. S1. The molecular orbital diagram of octahedral NiO_6 and square planar NiO_4. (a) Schematic illustration of the molecular orbitals of octahedral NiO_6. (b) Schematic illustration of the energy band of octahedral NiO_6 with the consideration of Mott-Hubbard splitting. The bonding bands including a_{1g}, t_{1u}, e_g, and t_{2g} exhibit oxygen character (denoted as M-O), while the antibonding bands $(M\text{-}O)^*$, *i.e.*, t_{2g}^*, a_{1g}^*, t_{1u}^*, and e_g^* show metal character. Among these electronic bands, M-O and t_{2g}^* are fully occupied, while e_g^* is partially occupied with one spin-up electron. Here, t_{2g}^* contains d_{xy}, d_{yz} and d_{xz} orbitals and e_g^* includes d_{z^2} and $d_{x^2-y^2}$ orbitals, respectively. Due to the on-site electron repulsion within the *d* orbitals, antibonding bands will split into an empty upper- and filled lower-Hubbard bands (denoted as UHB and LHB, respectively), with an energy difference U. As indicated in Fig. 1a and Fig. S1b, the traditional AEM route involves the removal of electron from the LHB, where Ni acts as the redox centre. (c) Schematic illustration of the molecular orbitals of square planar NiO_4. In the square planar NiO_4 structure, Ni-O bond is formed through the hybridization of O 2*p* and Ni

3*d*, 4*s*, and 4*p* orbitals (Fig. S1c). The bonding orbitals included e_u, b_{1g}, and a_{1g} (denoted as M-O), while the antibonding orbitals included e_u^*, a_{1g}^*, a_{2u}, b_{1g}^* and a_{1g}, and non-bonding metal 3*d* orbitals (M_{NB}) that involved b_{2g} and e_g. Among these electronic bands, M-O, M_{NB} and a_{1g} are fully occupied, while e_u^*, a_{1g}^*, a_{2u}, and b_{1g}^* are empty (Fig. S1c). (d) Schematic illustration of the energy band of square planar NiO_4 with consideration of Mott-Hubbard splitting. Due to the on-site electron replusion within the 3*d* orbitals, antibonding bands in square planar NiO_4 structure will split into an empty upper- and filled lower-Hubbard bands, with an energy difference as indicated by U (Fig. S1d).

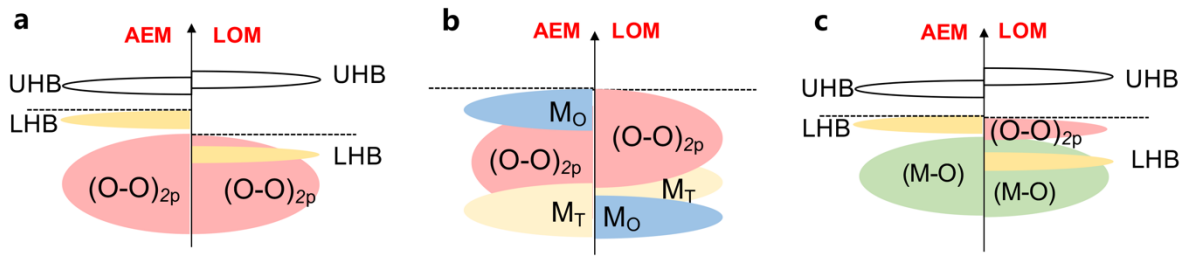

Fig. S2. The energy diagrams of AEM and LOM in perovskite (a), spinel oxides (b), and transitional metal oxyhydroxide (c). Here, $(O\text{-}O)_{2p}$ refers to the non-bonding oxygen states. In perovskite ABO_3 system (a), B is located at an octahedral enviroment and its $\boldsymbol{d_{z^2}}$ and $\boldsymbol{d_{x^2-y^2}}$orbitals spatially overlap with oxygen, forming bonding and antibond bands. Affected by the perovskite structure symmetry, some oxygen orbitals may not hybridize with metal, which results in the formation of $(O\text{-}O)_{2p}$ bands. When $(O\text{-}O)_{2p}$ bands are lower than the lower Hubbard band (LHB), OER is based on the adsorbate evolution mechanim (AEM) route. However, when $(O\text{-}O)_{2p}$ bands are above the lower Hubbard band (LHB), OER follows the lattice oxygen oxidation mechanism (LOM). In this case, non-bonding oxygen states would become accessible. In spinel oxides (AB_2O_4) structure (b), three metal cations (five *d* orbitals each) and four oxygens (three 2*p* orbitals each) are incorporated into the spinel structure and some oxygen orbitals may not hybridize with the metallic states, which results in the formation of $(O\text{-}O)_{2p}$ bands. Here, the metal electronic state of tetragonal cation is denoted as (M_T) and metal state of octahedral cation is denoted as (M_O). When $(O\text{-}O)_{2p}$ bands are above M_T, its OER route follows LOM. As a result, non-bonding oxygen states become accessible. In CoZn oxyhydroxide (c), when part of the metal atoms are replaced by low-coordinated metal element (Zn), it will form non-bonding oxygen states (O_{NB}) and increase the covalency of M-O. This would lead to formation of $(O\text{-}O)_{2p}$ bands above LHB and these non-bonding oxygen states become accessible for LOM. From the above discussion, the key to realize LOM is to trigger the accessibility of these non-bonding oxygen states.

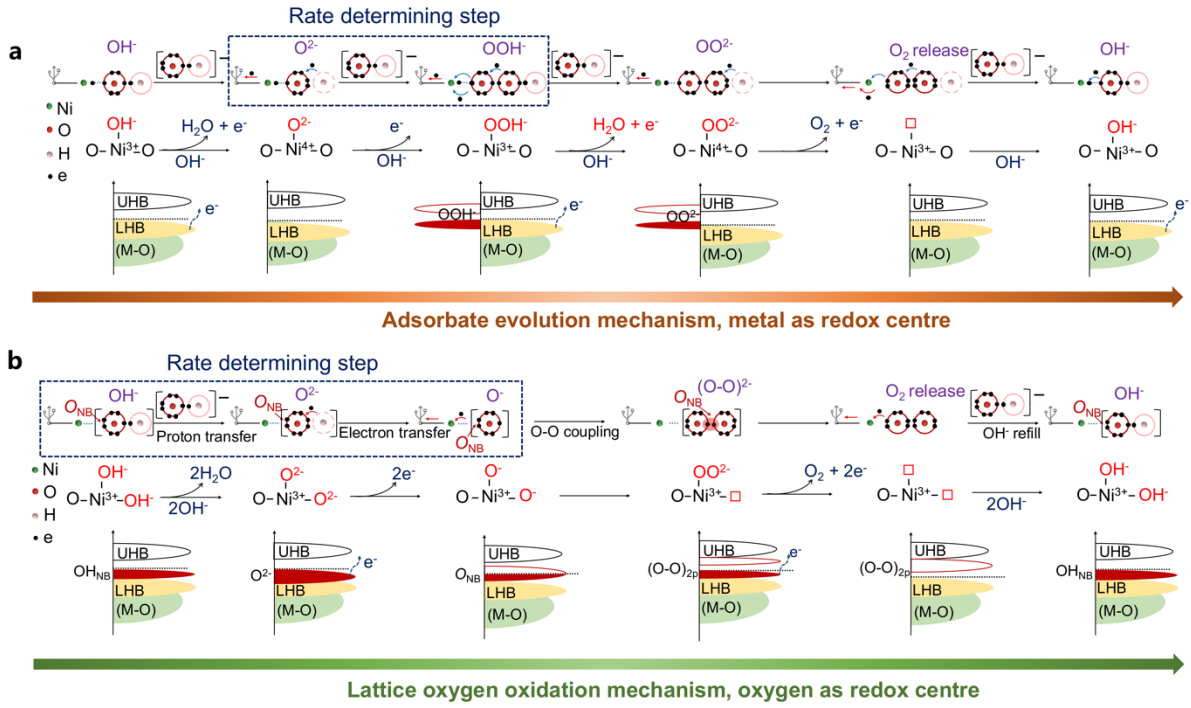

Fig. S3. Electron transfer pathways of traditional AEM (metal redox) and LOM (oxygen redox) OER routes. (a) Electron transfer pathway of traditional AEM route, where metal acts as the redox center. (b) The electron transfer pathway of conventional LOM route, where oxygen acts as the redox center. The bonding bands exhibiting oxygen character is denoted as (M-O). Due to the on-site electron repulsion within the *d* orbitals, antibonding bands will split into empty upper- and filled lower-Hubbard bands (denoted as UHB and LHB, respectively). OH_{NB} and O_{NB} show the non-bonding hydroxide and non-bonding oxygen states, respectively. $(O\text{-}O)_{2p}$ represents the O-O hybridized band. In the traditional AEM route, LHB is around Fermi level, while in the LOM route non-bonding oxygen band is around Fermi level. The detailed orbital diagram of the octahedron is shown in Fig. S1a.

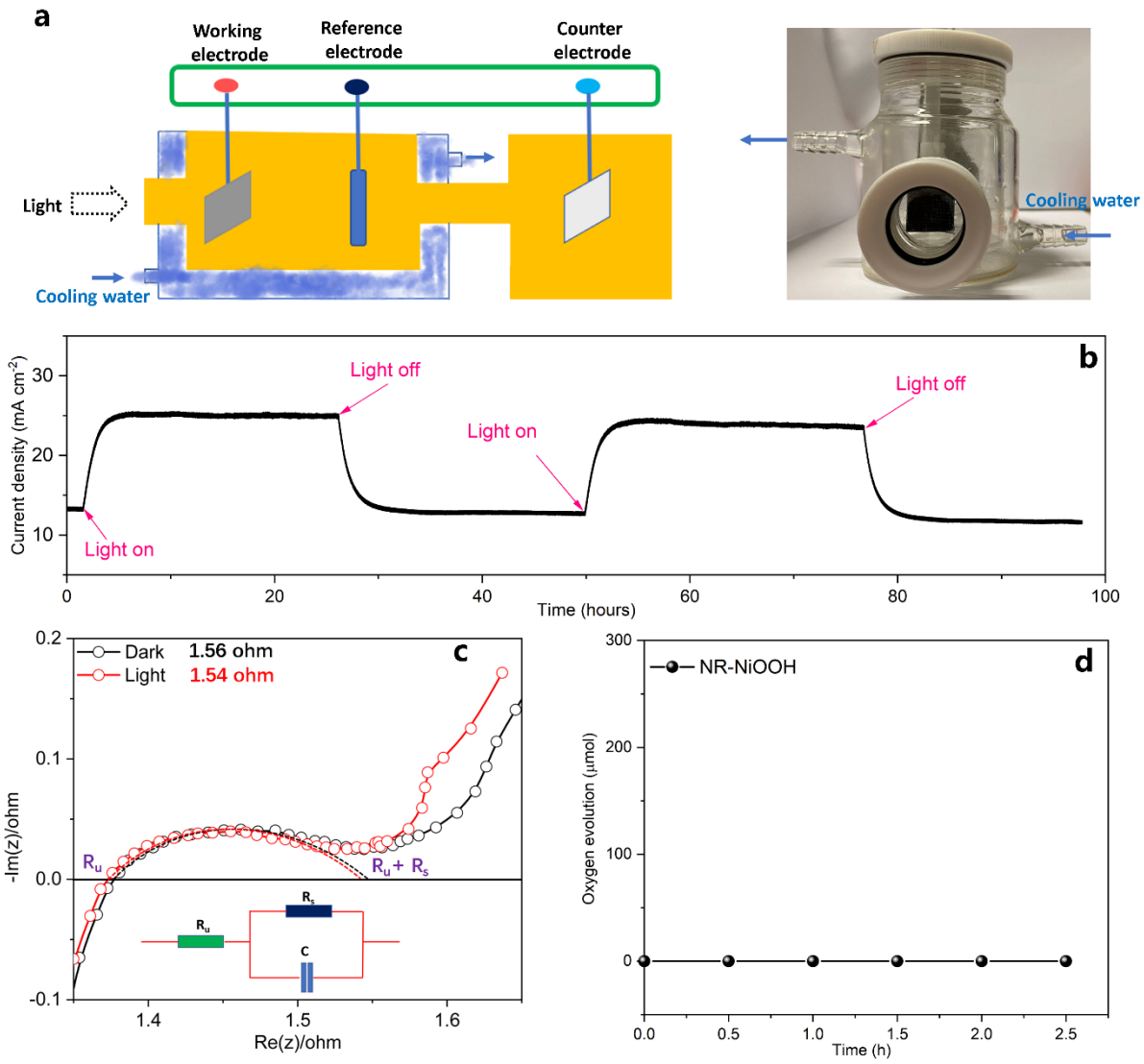

Fig. S4. The electrochemical and photocatalytic measurement of NR-NiOOH. (a) The thermostatic bath device. Left: Schematic illustration of the thermostatic bath, whereby cooling water is used to keep the temperature of the system constant; Right: Photograph of the actual thermostatic bath. (b) Chronoamperometry curves at a constant potential of 1.42 V *vs.* RHE for NR-NiOOH sample. (c) Electrochemical impedance spectroscopy data for NR-NiOOH with and without light. It is measured using a three-electrode configuration in 1 M KOH solution. R_u is the resistance of the catalytic material and R_s is the resistance of the electrolyte. In our work, we used the entire resistance (R_u + R_s) for *iR* correction. After fitting the result, it is found the resistances of NR-NiOOH under dark and in the light were relative similar. (d) The gas chromatograph measurement of NR-NiOOH using $K_2S_2O_8$ as electron acceptor under AM 1.5G condition. Performing a trial OER measurement in the presence of a sacrificial electron

acceptor is one way to assess the suitability the band position of a specific composition as an OER photocatalyst. The result shows that after 2.5 hours of operation, no oxygen is detected, indicating that the enhanced OER activity in NR-NiOOH is not attributed to the generation of light induced holes. More importantly, our *operando* XAFS data show a geometry conversion from octahedral to square planar under light irradiation, which indicates that this type of photon-induced electron transfer is not a photocatalytic behavior (Fig. S10 to 12).

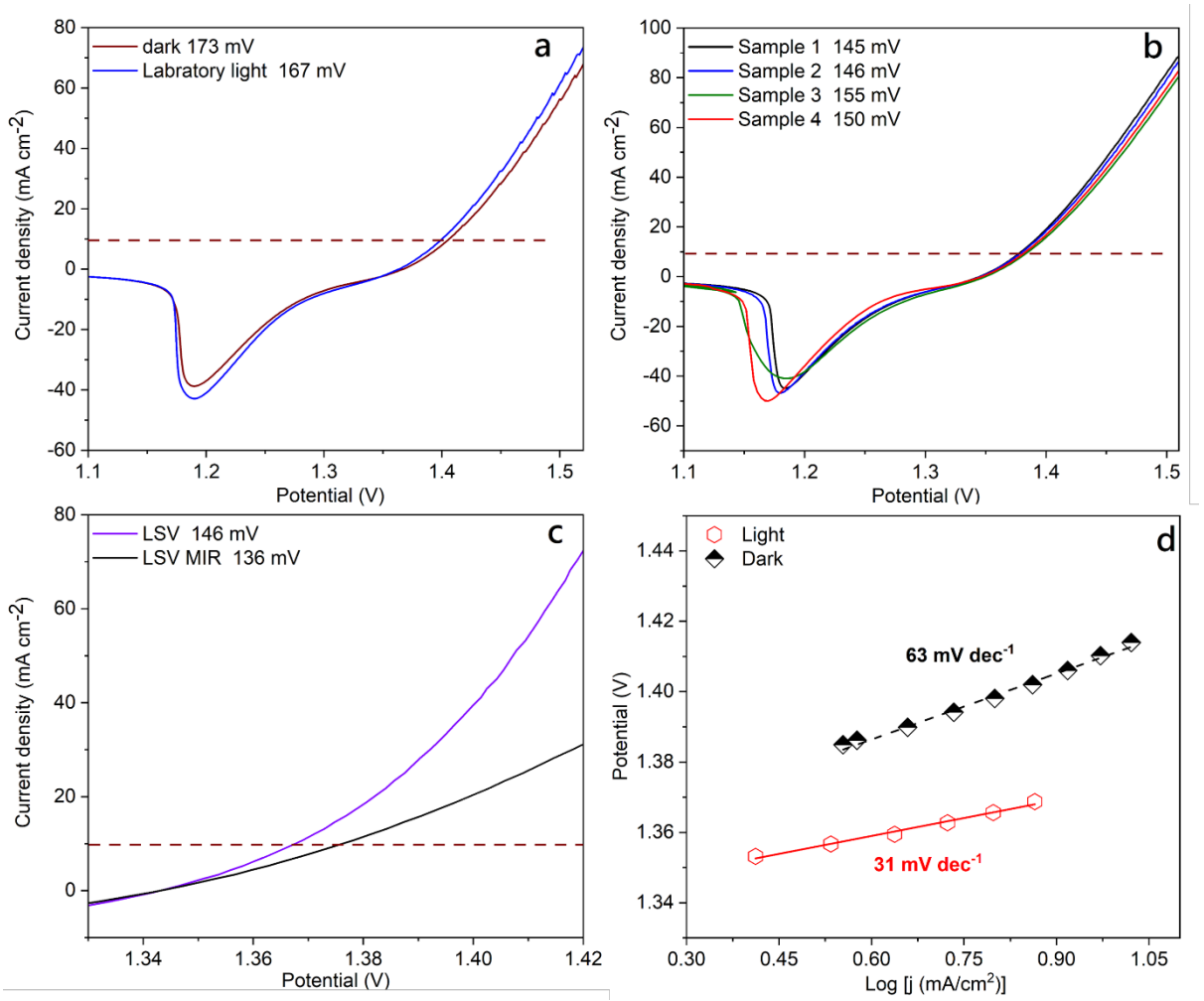

Fig. S5. The electrochemical measurement of NR-NiOOH samples under light irradiation. (a) OER polarization curves of NR-NiOOH recorded under a scan rate of 0.1 mV/s under dark and laboratory light. The experiment shows that when subjected to laboratory light irradiation (12.3 mW cm^{-2}), it requires an overpotential of 167 mV to reach a current density of 10 mA cm^{-2}. This measured overpotential is 6 mV lower than that of NR-NiOOH in the dark, implying the positive effects of laboratory light irradiation on enhancing OER performance for NR-NiOOH. (b) The OER polarization curves of four more NR-NiOOH samples under light irradiation. Their overpotentials recorded at 10 mA cm^{-2} ranged from 145 mV to 155 mV. The standard deviation value of the dataset, *i.e.*, 145, 146, 155, 150, and 147 (Figure 2c), is 3.6, which indicates that the electrochemical experiments are highly repeatable. (c) OER polarization curves of NR-NiOOH sample under light irradiation, with a 0.1 mV s^{-1} scan rate and 90% *iR* correction. It shows that using 90% *iR* correction (R = 1.38 ohm, the resistance of the catalytic material), the overpotential of NR-NiOOH sample under light irradiation at 10

mA cm^{-2} is 136 mV. (d) The Tafel slope of NR-NiOOH under light and dark, respectively. To achieve a better linear fitting, for the sample under light irradiation, the current range value was selected between 0.4 and 0.9, and for the sample under dark conditions, the current range value was selected between 0.5 and 1.0.

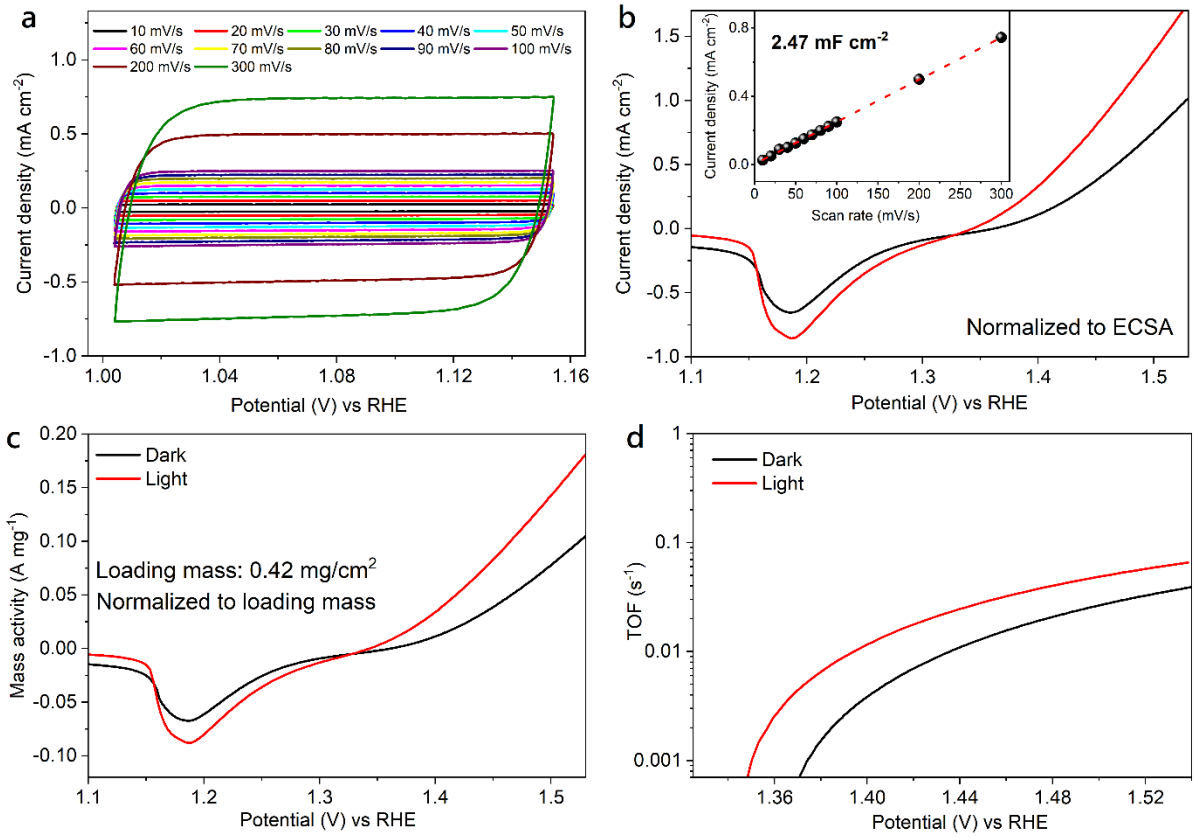

Fig. S6. The intrinsic activities of NR-NiOOH samples under light irradiation. (a) The electrochemical surface area (ECSA) of NR-NiOOH sample; (b) Current density normalized to ECSA; (c) current density normalized to loading mass; (d) Turnover frequency of NR-NiOOH sample under dark and light. Electrochemically active surface areas (ECSAs) of the samples are evaluated through the C_{dl} (double layer capacitance) measurement and the current densities were normalized to ECSAs. The loading mass of NR-NiOOH is 0.42 mg cm^{-2}, which was calculated based on Inductive Coupled Plasma (ICP) analysis. The turnover frequency (TOF) is calculated through the following equation: $TOF=\frac{I}{4*F*m}$ (where I: current in amperes; F: Faraday constant; m: number of moles of the active catalyst). Note that all the catalysts are assumed to be active in this work. The comparison of current normalized to ECSA in our work and previously reported is provided in Table S2; the comparison of current normalized to loading mass in our work and previously reported is seen in Table S3; the comparison of TOF between our work and previously reported is shown in Tables S4. Based on Table S2 to S4, by normalizing to the electrochemical surface area, NR-NiOOH under light irradiation is able to maintain superior activities especially in the low potential range, *i.e.*, <1.45 V *vs.* RHE, as

compared to other OER electrocatalysts. However, when this is normalized to loading mass or when considering the turnover frequency, the merits of NR-NiOOH under light irradiation are not outstanding. Such an observation can be easily understood. In the case of the normalization of current to loading mass and turnover frequency, all catalysts are assumed to be active. However, this is not the real case, since most catalysts are buried within, which remain to be inactive during the OER process. The loading mass of our NR-NiOOH was 0.42 mg/cm^2, while for most of the cited works, the loading mass on the glassy carbon was usually in the range of 0.03 to 0.2 mg/cm^2. Hence, for our NR-NiOOH, the ratio of active catalysts to all catalysts is much lower than that of the one coated on the glassy carbon.

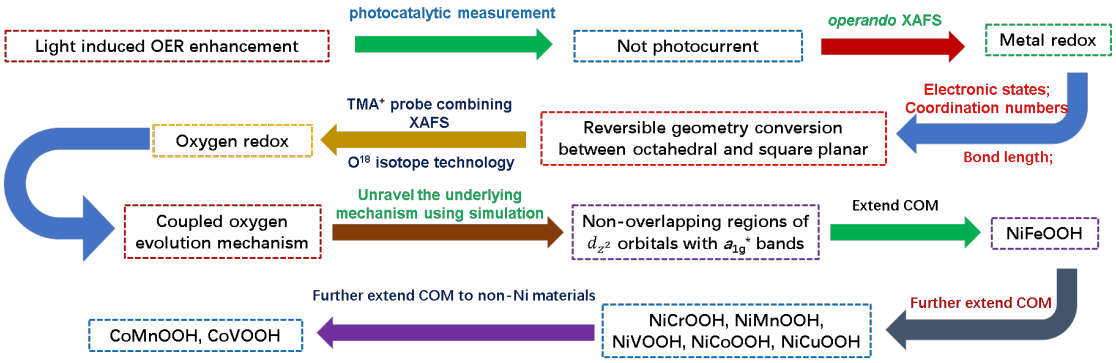

Fig. S7. The organization of our work. The description on the idea flow is shown in the section of Discussion on possible reasons for light enhanced OER activity in Supplementary Discussions.

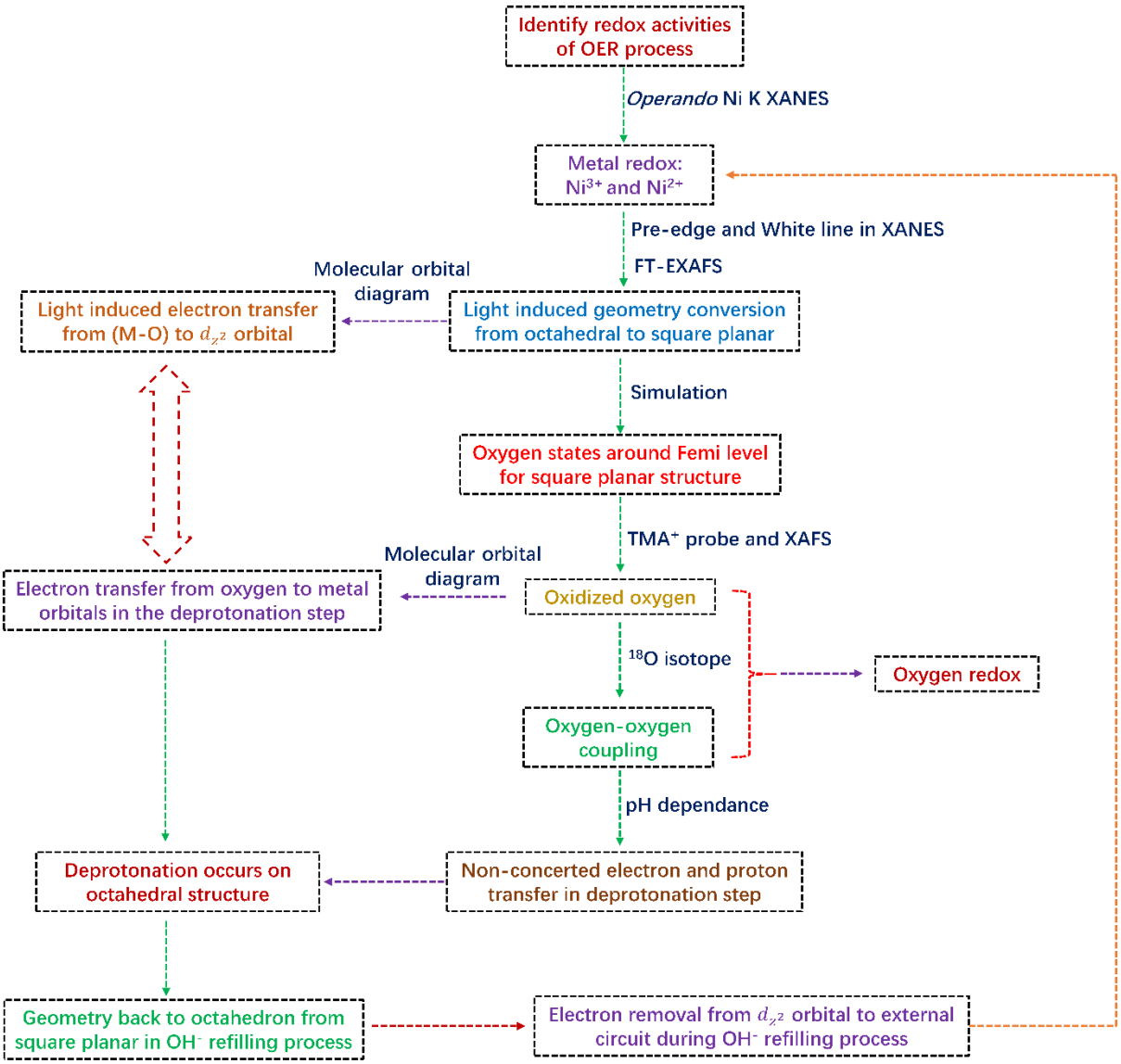

Fig. S8. The idea flow of our experiment to unveil COM route. The detailed description is shown in Supplementary Discussions.

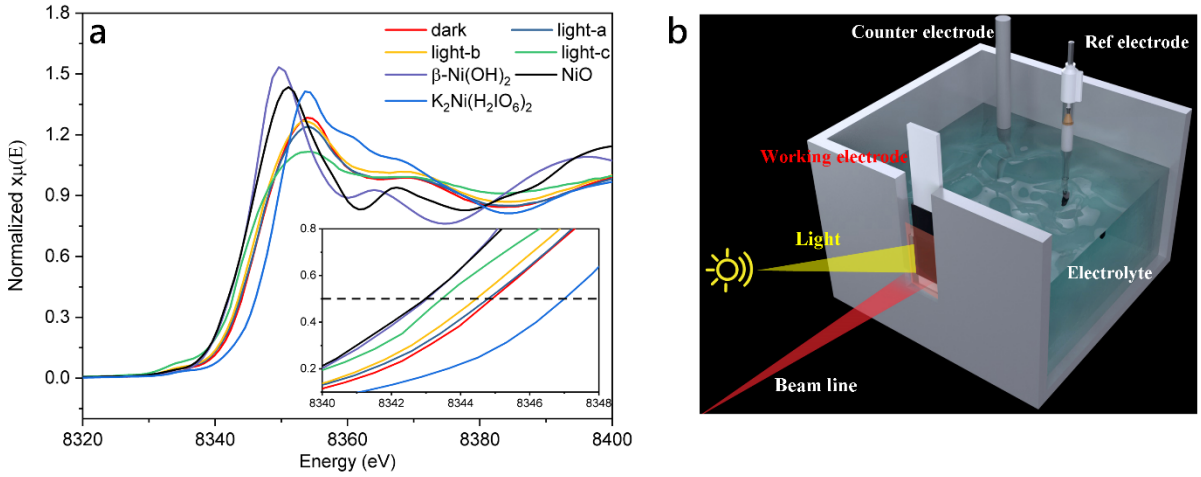

Fig. S9. The Ni *K*-edge XANES spectra. (a) Ni *K*-edge XANES spectra of NR-NiOOH without and subjected to light irradiation using standard β-$Ni(OH)_2$ (Ni^{2+}), NiO (Ni^{2+}) and $K_2Ni(H_2IO_6)_2$ (Ni^{4+}) as the reference (inset showing the absorption edge of these samples). To estimate the 3*d* orbital occupancy, we track the oxidation state of each sample with XANES (absorption edge). (b) The device for *operando* XAFS, using Hg/HgO electrode as the reference electrode and Pt as the counter electrode.

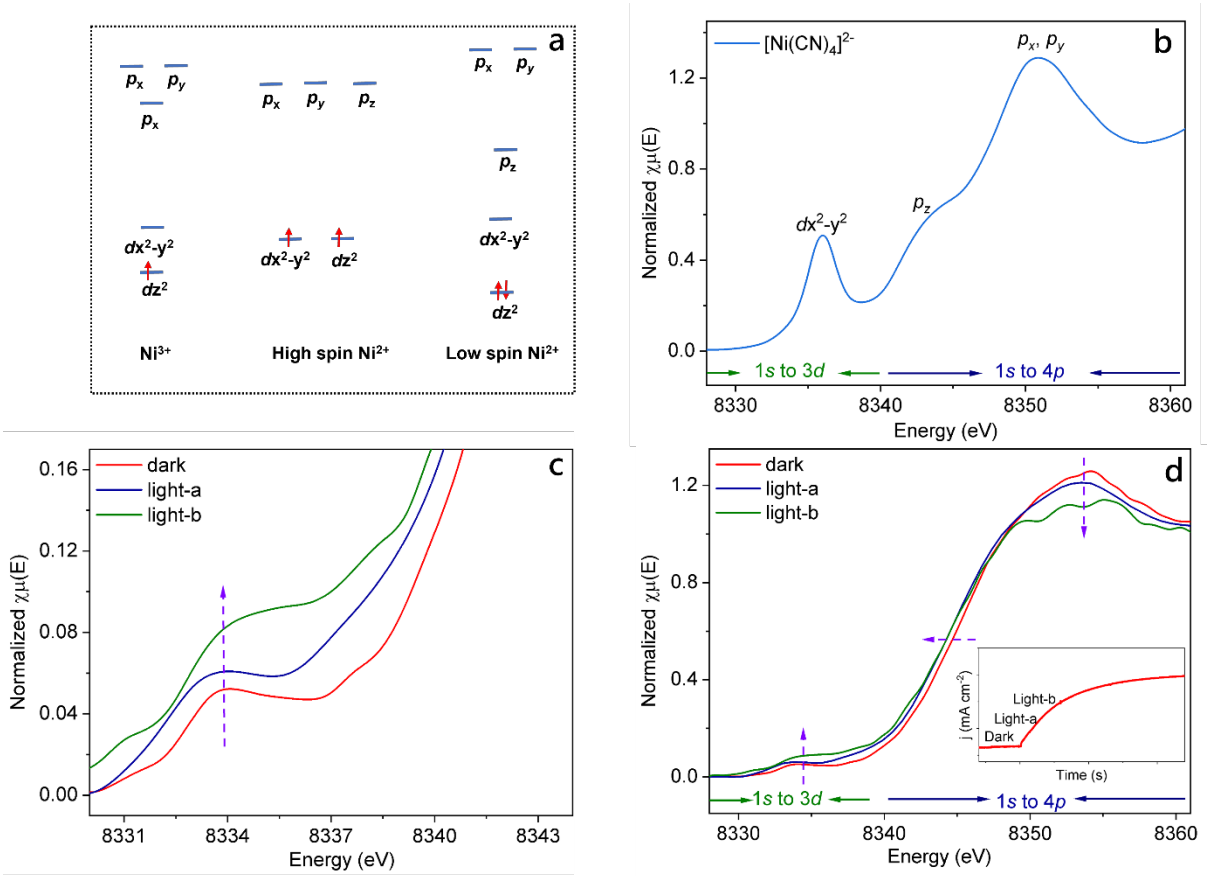

Fig. S10. The *operando* HR-XAFS spectra. (a) The orbital diagram of Ni^{3+}, high spin Ni^{2+} and low spin Ni^{2+}. (b) The HR-XAFS spectra of $[Ni(CN)_4]^{2-}$ ion. To identify the features of low spin Ni^{2+} in HR-XAFS spectra, a material with known low spin Ni^{2+} electronic configuration, *i.e.*, $[Ni(CN)_4]^{2-}$ ion, was investigated with HR-XAFS. A sharp peak is observed in the pre-edge range (8330 to 8340 eV), which corresponds to the localized $d_{x^2-y^2}$ orbital of the low spin Ni^{2+}. The white line (8340 to 8360 eV) is split into two peaks, which corresponds to p_z and p_x, p_y orbitals, respectively. At the same time, the difference between these two peaks is 7.2 eV, which is significantly larger than that of Ni 1s core hole lifetime (1.62 eV). Given that Ni-O and Ni-CN exhibit approximately similar bond strength, the splitting of white line in HR-XAFS spectra is one of the features of low spin Ni^{2+} electronic configuration in NR-NiOOH sample. (c) The pre-edge in HR-XAFS spectra of NR-NiOOH subjected to light irradiation. (d) *Operando* HR-XAFS spectra of NR-NiOOH subjected to light irradiation (inset showing the electrochemical curves accompanying the *operando* HR-XAFS). It should be noted that due to the longer collection time required for HR-XAFS measurement, it is difficult

to capture the spectra at the high current regions, *i.e.* stabilized current state in the inset of Fig. S10d.

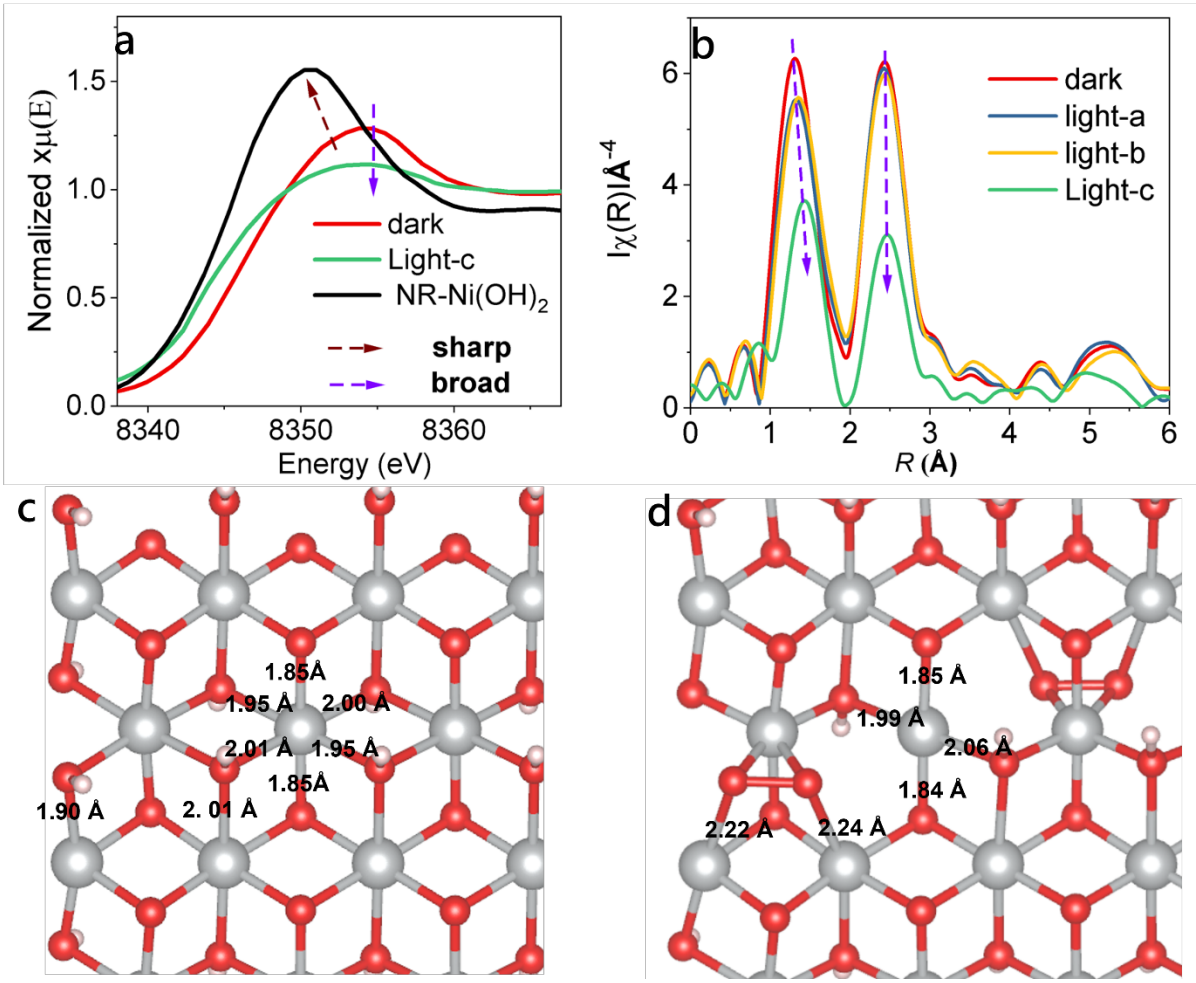

Fig. S11. The white line and FT-EXAFS spectra of NR-NiOOH samples under light irradiation. (a) the white line (corresponding to electronic states of 4*p*) of NR-NiOOH subjected to light irradiation and NR-Ni(OH)$_2$; (b) FT-EXAFS spectra of NR-NiOOH subjected to light. (c) the relaxed model of NR-NiOOH structure. (d) the relaxed model of square planar NR-NiOOH structure.

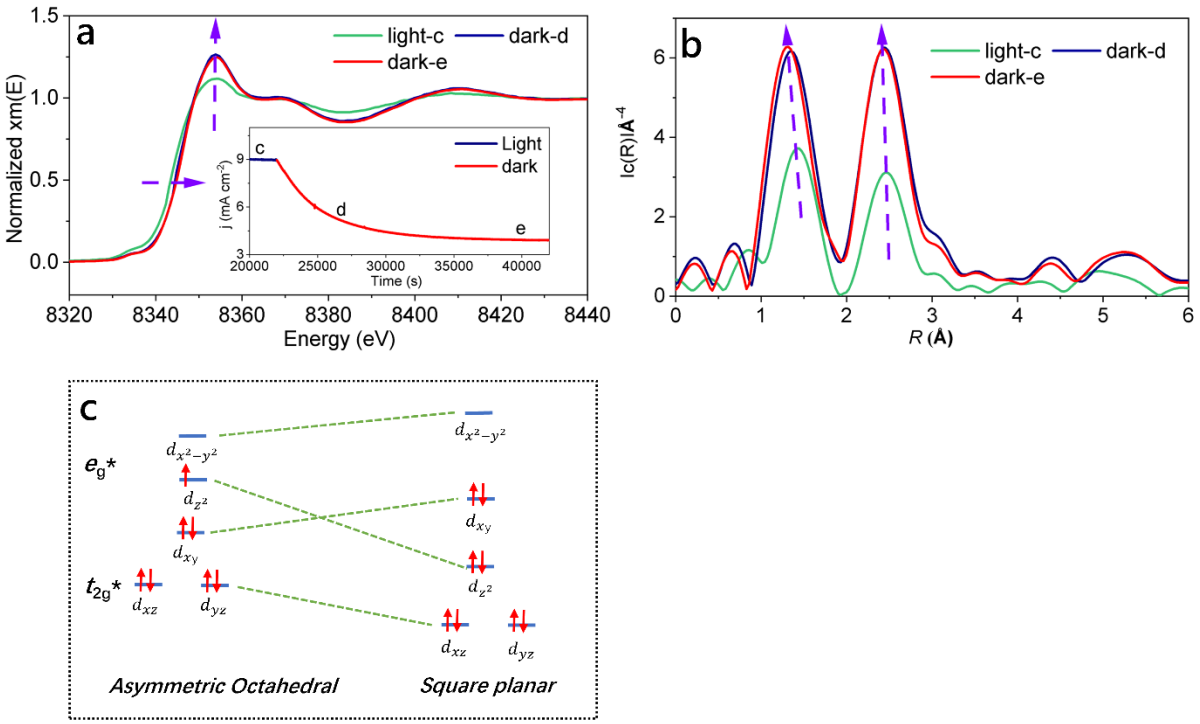

Fig. S12. ***Operando*** **XAFS spectra of NR-NiOOH switching off light irradiation.** (a) *Operando* Ni *K*-edge XANES spectra of NR-NiOOH switching off light irradiation (inset showing the electrochemical curves accompanying the *operando*-XAFS); (b) FT-EXAFS spectra of NR-NiOOH switching off light irradiation. Interestingly, when the light source is switched off, a gradual blue shift in the absorption edge with increased white line intensity for the sample subjected to the light irradiation is observed (Fig. S12a). Furthermore, the intensities of both Ni-O and Ni-Ni bonds gradually increase (Fig. S12b). These results indicate that the structure of the sample gradually reverts to its initial configuration under dark condition, which further confirms that such a geometric conversion triggered by light is highly reversible. The electrochemical curves accompanying the *operando*-XAFS are provided in the inset of Fig. S12a. Thus, based on the XANES and FT-EXAFS results, it is reasonable to conclude that a reversible geometry conversion between the octahedral and square planar occurs during the OER process. Hence, the enhanced OER activity exhibited by NR-NiOOH under light irradiation is related to the reversible geometric conversion between octahedral to square planar. (c) The electron configurations of Ni^{3+} (octahedral) and low spin Ni^{2+} (square planar). It shows that the electronic structure differences between Ni^{3+} octahedral and Ni^{2+} square planar are the configuration of d_{z^2} orbital. Hence, the geometry conversion could be only realized when

there is an electron transfer to d_{z^2} orbital. At the same time, the breakage of Ni-O bond is intrinsically the electron transfer from bonding bands (M-O) exhibiting oxygen character into anti-bonding bands $(M\text{-}O)^*$ showing metal character. Hence, the geometry conversion from octahedral to square planar can be only realized when there is an electron transferred from (M-O) (bonding bands) to d_{z^2} orbital. Noted that in the octahedral structure, $d_{x^2-y^2}$, d_{z^2}, d_{xy}, d_{xz}, and d_{yz} orbitals belong to antibonding bands, and in the square planar structure $d_{x^2-y^2}$ and d_{z^2} orbitals belong to antibonding bands. Hence, accompanied with the geometry conversion from octahedral to square planar, the d_{z^2} orbital is shifted into the lower energy. This indicated the energy difference between the highest occupied and lowest unoccupied electron states within antibonding bands greatly increase when the geometry conversion from asymmetric octahedral to square planar.

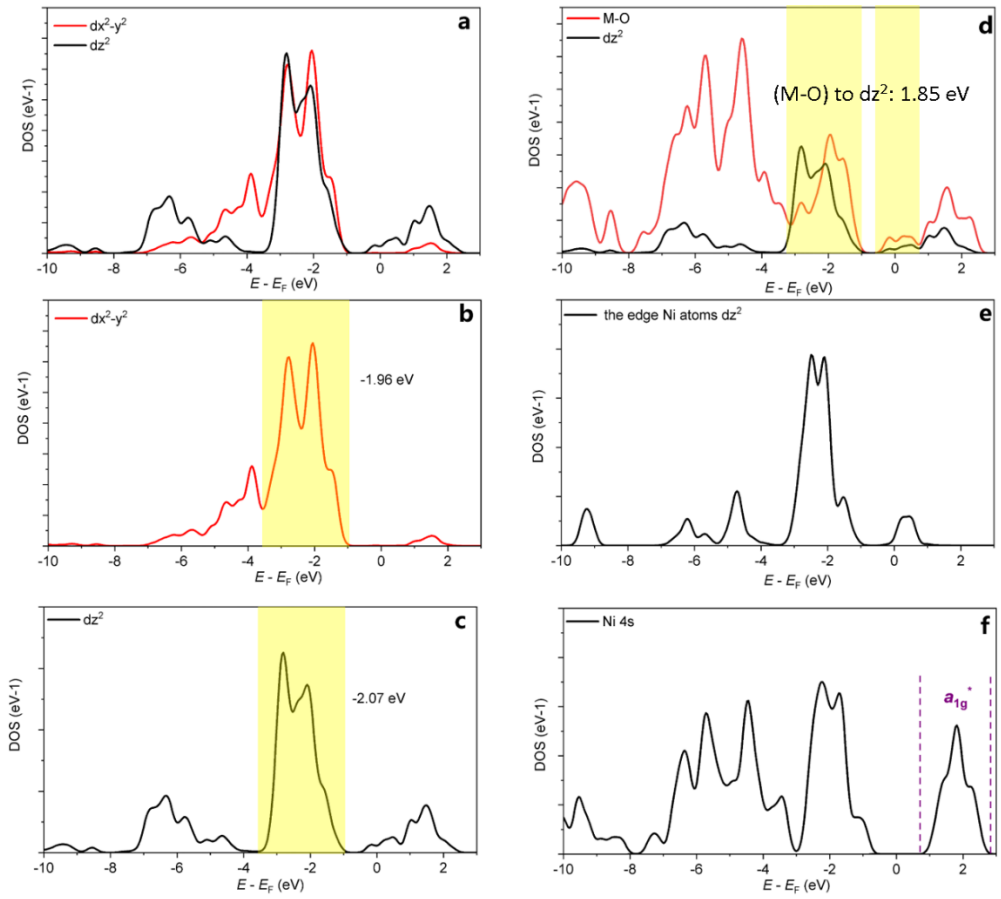

Fig. S13. The projected density of states (PDOS) of NR-NiOOH. (a) PDOS of $d_{x^2-y^2}$ and d_{z^2} orbitals. (b) (c) Schematic illustrations of the band center of $d_{x^2-y^2}$ and d_{z^2} orbitals, obtained from calculations. (d) PDOS of d_{z^2} orbital and (M-O) bands. The calculation result indicates that there is a new hybridization region of (M-O) and d_{z^2} orbital that appears around Fermi level. (e) PDOS of $d_{x^2-y^2}$ and d_{z^2} orbitals for the edge four-coordinated Ni atoms. (f) PDOS of d_{z^2} orbital for the whole Ni atoms and edge Ni atoms. The calculation result indicates that the newly appeared hybridization region is mainly due to the four-coordinated Ni atoms.

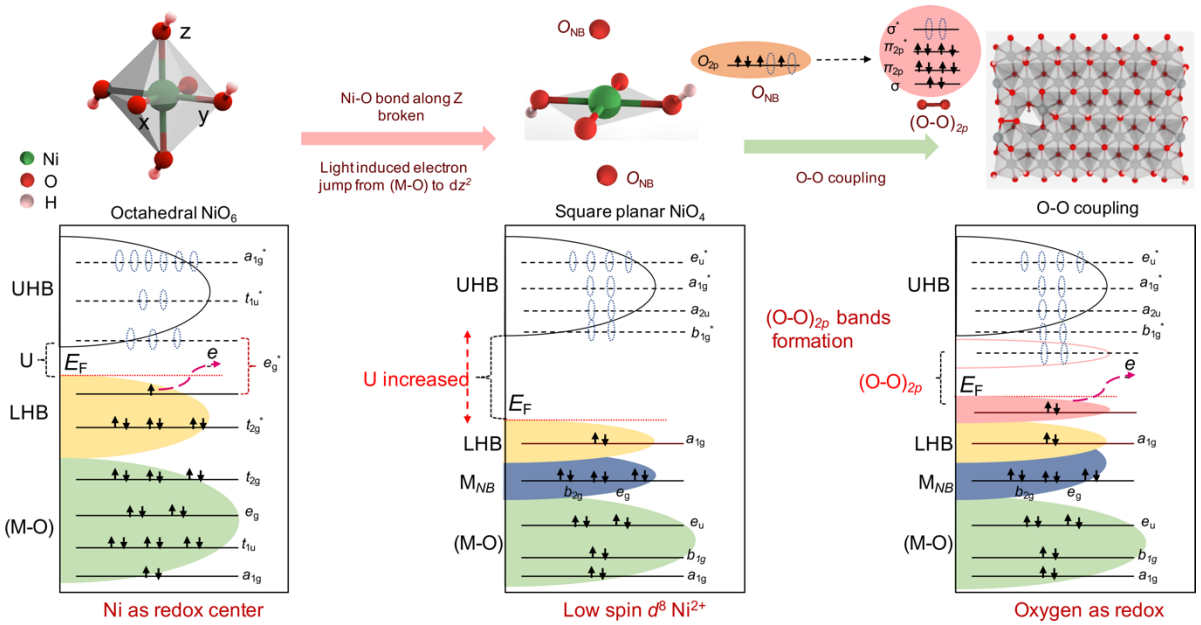

Fig. S14. Illustration of the induced transfer of redox centre from metal to oxygen *via* light irradiation. In this diagram, UHB and LHB denote the upper and lower Hubbard bands, respectively. M_{NB} represents the non-bonding 3*d* orbitals of metal and $(O\text{-}O)_{2p}$ represents the O-O hybridized band. Due to the on-site electron repulsion within the *d* orbitals, antibonding bands will split into an empty upper- and filled lower-Hubbard bands (denoted as UHB and LHB, respectively), with an energy difference U. As electron is transferred from (M-O) to $\boldsymbol{d_{z^2}}$ orbital in the e_g^* band, it triggers the change in the crystal structure of NiO_6 from conventional octahedral to square planar configuration. As a result, Ni-O bond (along z) will be broken, and this leads to the formation of O_{NB}. Then, O_{NB} is stabilized by hybridizing with its neighboring O_{NB} states to form $(O\text{-}O)_{2p}$ band. The previous results indicate that the energy difference between the highest occupied and lowest unoccupied electron states within antibonding bands greatly increase when the structure changes from asymmetric octahedron to square planar (Fig. S12c). As a result, the generated $(O\text{-}O)_{2p}$ band would be around Fermi level due to the significant energy difference. Thus, due to this modulation in the electronic configuration, the redox center is oxygen. This could be further confirmed using PDOS (Fig. S15).

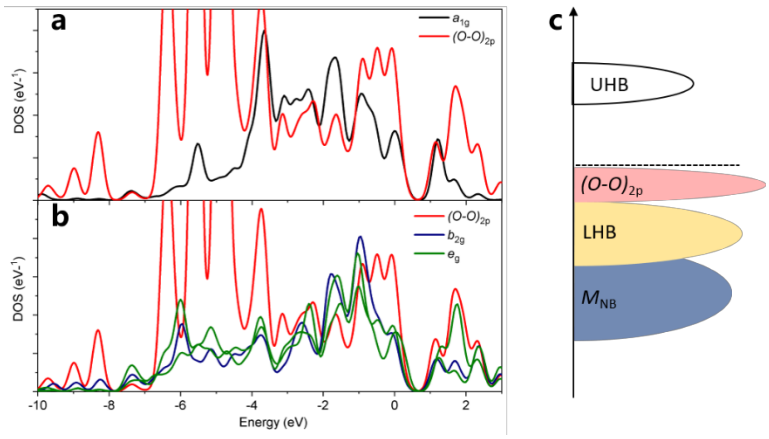

Fig. S15. The PDOS of oxygen-oxygen coupling NR-NiOOH. (a) PDOS of a_{1g} orbital and $(O\text{-}O)_{2p}$ bands; (b) PDOS of b_{2g}, e_g orbitals, and $(O\text{-}O)_{2p}$ bands; (c) The corresponding energy diagram of O-O coupling NR-NiOOH. The O-O coupling NR-NiOOH model is provided in Fig. S14. The calculation result indicates that, as compared with a_{1g}, b_{2g} and e_g bands, $(O\text{-}O)_{2p}$ band is much closer to the Fermi level. In square planar structure, a_{1g} includes d_{z^2}orbital, b_{2g} involves d_{xy} orbital, and e_g consists of d_{xz} and d_{yz} orbitals. As a result, $(O\text{-}O)_{2p}$ band is much closer to Fermi level as compared with d_{z^2}, d_{xy}, d_{xz} and d_{yz} orbitals. Given that LHB of octahedral structure involves d_{z^2}, d_{xy}, d_{xz} and d_{yz} orbitals, this result indicates that oxygen is still the redox center even when NR-NiOOH is the octahedral geometry. Thus, based on these discussions, we could know regardless of the NR-NiOOH structure after O-O coupling, *i.e.*, octahedron, square planar, or the "intermediate" between square planar and octahedral, oxygen is the redox center.

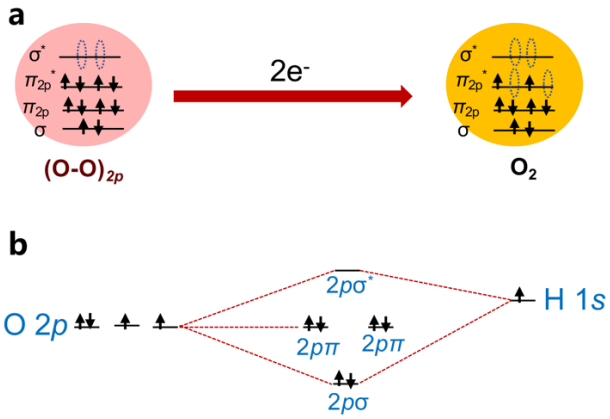

Fig. S16. The electronic configuration of (O-O) coupling. (a) Schematic electronic configuration for (O-O) coupling and O_2 gas. It clearly indicates that, in order to form O_2 gas two electrons are required to be removed from (O-O) coupling bands. (b) The molecular orbital diagram of OH^-. Among the O $2p$ atomic orbitals, the $2p_z$ orbital has overlap with the H $1s$ orbital, forming a bonding molecular orbital $2p\sigma$, and an antibonding molecular orbital $2p\sigma^*$. As for the $2p_x$ and $2p_y$ orbitals, they do not have overlap with the H $1s$ orbital, renamed as $2p\pi$ molecular orbitals.

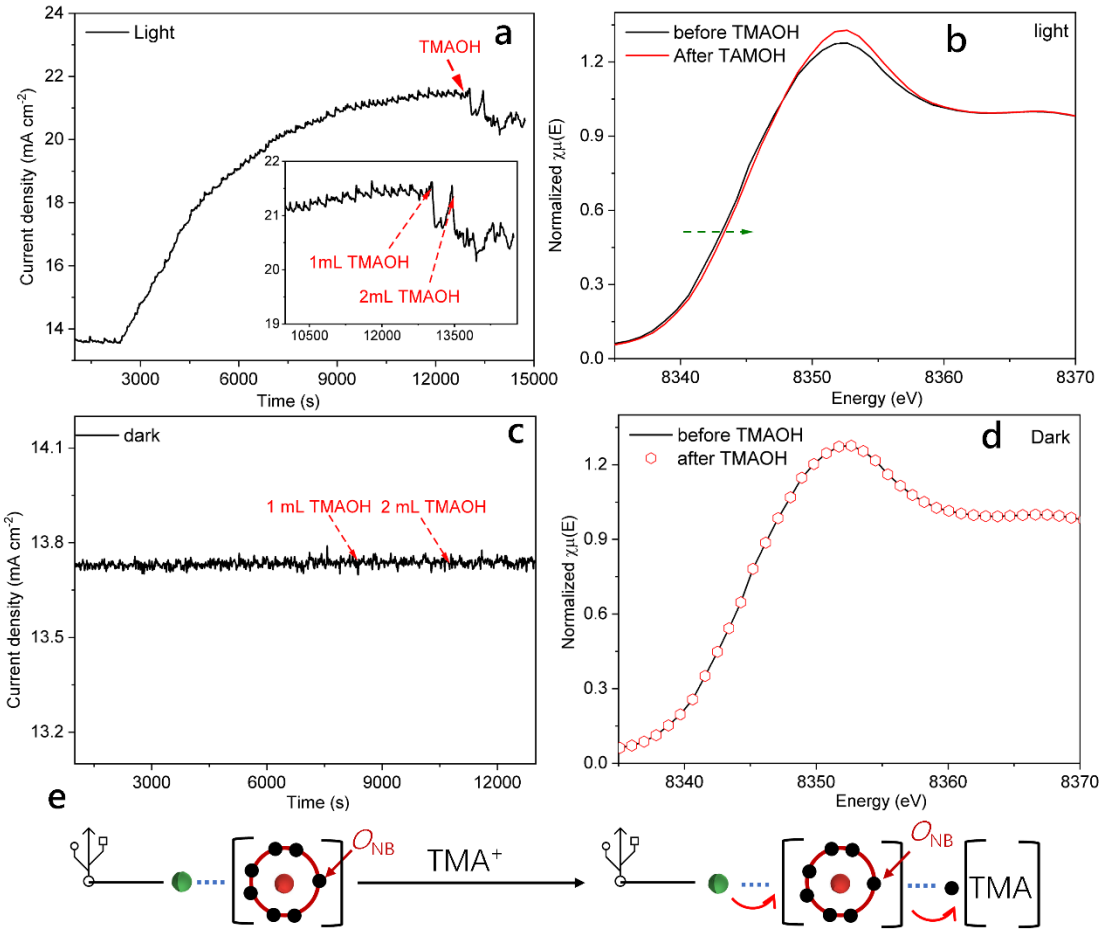

Fig. S17. The electrochemical and XANES results of NR-NiOOH sample before and after TMA^+ under light and dark conditions. (a) (c) TMAOH test of NR-NiOOH using chronoamperometry measurement at a potential of 1.51 V *vs.* reversible hydrogen electrode (RHE) under light and dark conditions. (b) (d) Ni *K*-edge XANES of NR-NiOOH sample before and after TMA^+ under light and dark conditions. (e) The electron transfer for the interaction of oxidized oxygen and TMA^+. As shown in Fig. S17a and c, when TMAOH is added in the electrolyte for the cell under light irradiation, there is an obvious decrease in the current densities, while no variations in the current are observed for the sample under dark conditions. The effect of TMAOH measurement on the OER properties could be shown in LSV curves (Fig. S18). These results clearly indicate that the addition of TMA^+ ion greatly inhibits the oxygen evolution process for the sample under light irradiation. At the same time, this TMA^+ ion addition does not affect the AEM-based OER process, *i.e.*, NR-NiOOH under dark conditions. The interaction of the oxidized oxygen atoms and TMA^+ is shown in Fig. S17e. To satisfy the 8-outermost electron configuration of oxygen, the non-bonding oxygen states of

oxidized oxygen atoms have to hybridize with TMA^+ ions by forming a chemical bond. Since the structure of TMA^+ remains unaltered after interactions (*4, 10*), such a chemical bond has to be realized by the transfer of an inner electron from Ni metal orbital to TMA^+, and this process can increase the valence of the metal. Then, OER measurement was terminated and Ni *K*-edge XANES was performed on NR-NiOOH samples. According to the experimental result, there is a significant increase in the Ni valence in the sample under light irradiation after the addition of TMA^+, while no variations in the Ni valence are observed for NR-NiOOH under dark conditions (Figure S17b and d). This result agrees well with the electron transfer shown in Fig. 17e, which indicates that the oxidized oxygen is formed during the OER process for the sample under light irradiation.

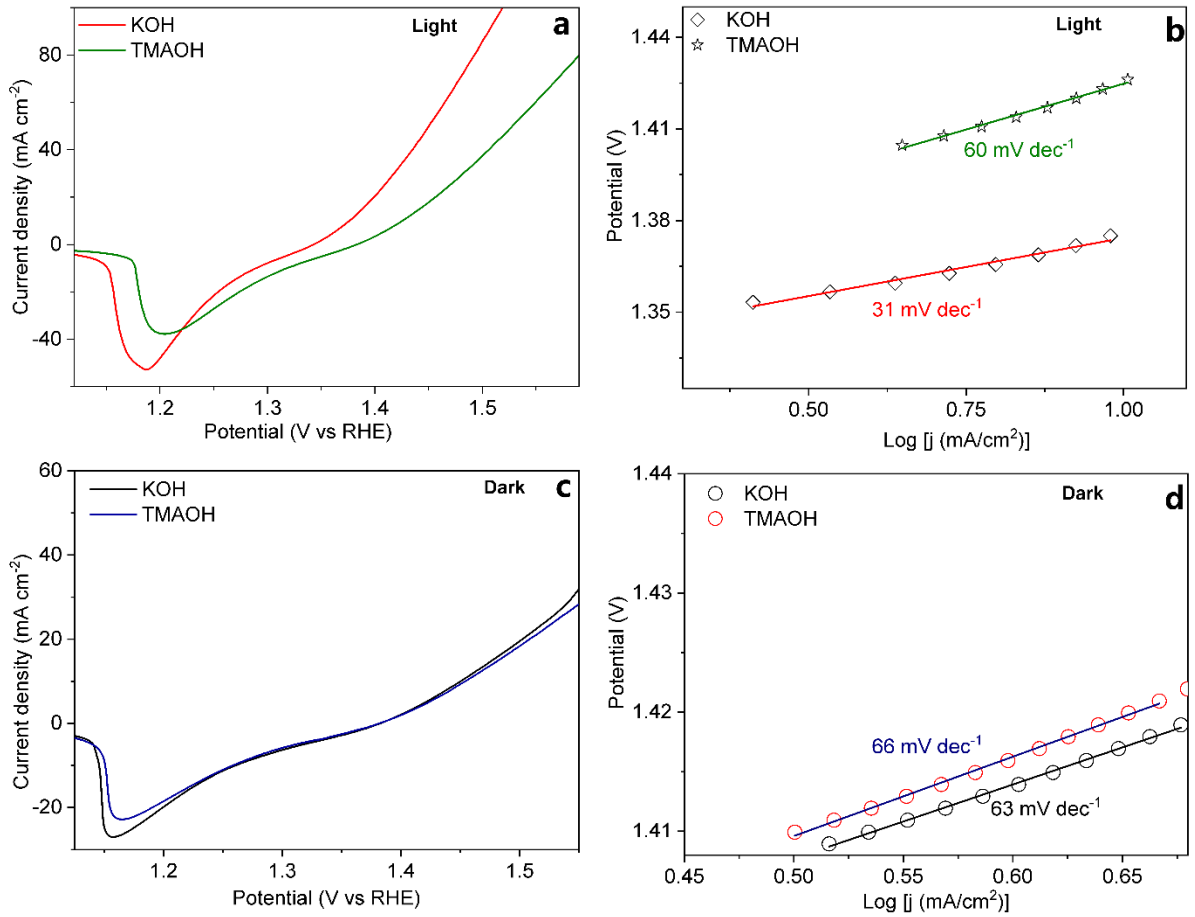

Fig. S18. The LSV and Tafel slopes of NR-NiOOH sample under light and dark conditions, in KOH and TMAOH electrolyte. The LSV and Tafel slopes of NR-NiOOH sample in the dark (a) and (c), and light (b) and (d) in KOH and TMAOH electrolyte. It shows that after additions of TMAOH, the Tafel slope of NR-NiOOH under light irradiation is decreased from 31 mV dec^{-1} to 60 mV dec^{-1}, while the dark sample shows no observable change. It clearly indicates the conversion of OER mechanisms from COM to AEM after addition of TMAOH.

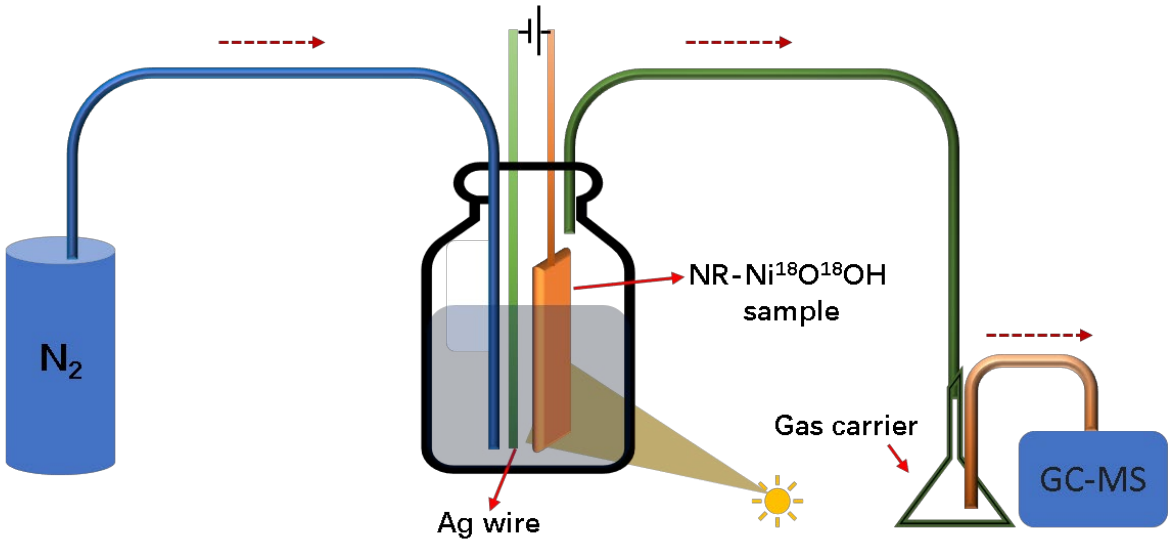

Fig. S19. The Schematic of our isotope devices. The process of ^{18}O isotope technology is summarized as two sections, *e.g.,* ^{18}O labelling electrocatalyst and gas product analysis using mass spectrometry. In the ^{18}O labelling section, NiS_2 precursor was oxidized in 97% $H_2{}^{18}O$ KOH electrolyte for 10 hours under a current density of 10 mA cm^{-2}. Our NR-$Ni^{18}O^{18}OH$ sample was prepared using this method. After which, the sample was washed using distilled water and then it was placed in a $H_2{}^{16}O$ contained gastight electrochemical cell that was connected to a gas carrier and mass spectrometer. In gas product analysis section, a two-electrode configuration was used, with Ag wire as the counter electrode. A 5 mL glass tube was used as the electrochemical cell to achieve the effective utilization of light by the catalyst. The flow rate of N_2 was 3mL/min. Before experiment, the electrolyte was bubbled with N_2 for 24 hours to remove the dissolved oxygen in electrolyte. The experiment was conducted under a constant current density of 2 mA cm^{-2}, with 0 to 4 minutes in dark and 4 to 30 minutes under AM 1.5G light irradiation (100 mW cm^{-2}). To decrease the effect of the remanent gas product (in the electrochemical cell and tube) on the GC-MS (as chromatography-mass spectrometry) analysis, the average ratio of $^{36}O_2$ to $^{32}O_2$ in 120s was used. The gas product during 120s was gradually stored in a gas carrier, and then the stored gas was transferred into GC-MS. By this method, the average ratios of $^{36}O_2$ to $^{32}O_2$ in 120s were obtained.

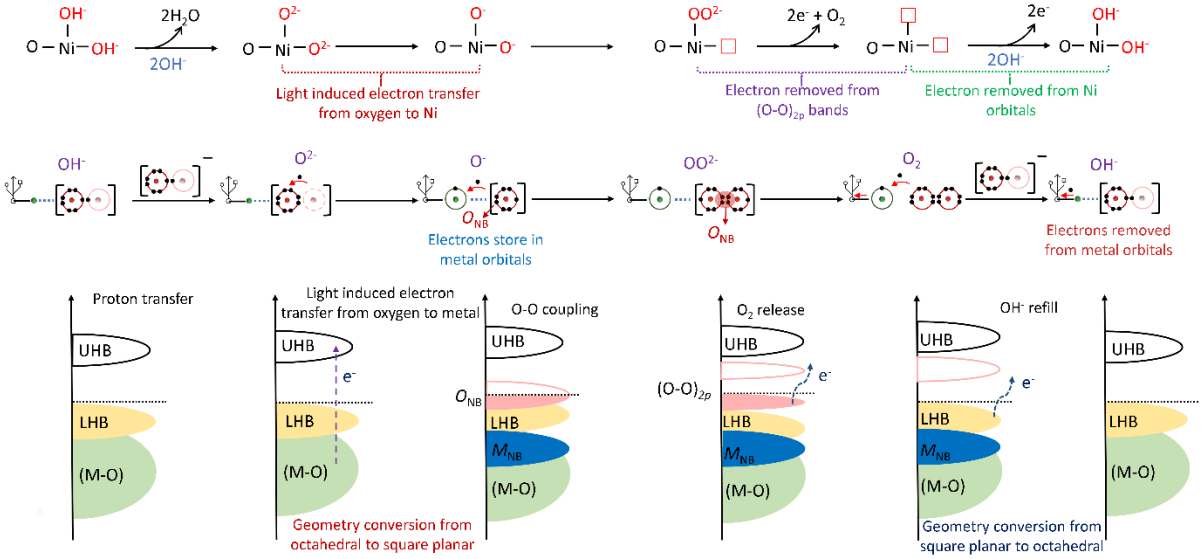

Fig. S20. Electron transfer pathways of our proposed COM routes. The bonding bands exhibiting oxygen character is denoted as (M-O). Due to the on-site electron repulsion within the *d* orbitals, antibonding bands will split into empty upper- and filled lower-Hubbard bands (denoted as UHB and LHB, respectively). OH_{NB} and O_{NB} show the non-bonding hydroxide and non-bonding oxygen states, respectively. $(O\text{-}O)_{2p}$ represents the O-O hybridized band. M_{NB} represents the non-bonding 3*d* orbitals of metal. Detailed orbital diagrams of octahedron and square planar are shown in Fig. S1. Our COM process can be summarized with these sequential steps: (1) Proton transfer occurring in octahedral NiO_6. (2) Under light irradiation, there is a geometric conversion of octahedral NiO_6 to square planar NiO_4 induced by the photon. (3) The hybridization of the formed O_{NB} leads to oxygen-oxygen coupling to form an oxygen band. (4) Release of oxygen resulting in OH^- vacancy sites. (5) Refilling of these vacancy sites with OH^-. (6) As a result of the OH^- refilling process, there is a concomitant geometric conversion of the square planar NiO_4 to octahedral NiO_6 configuration.

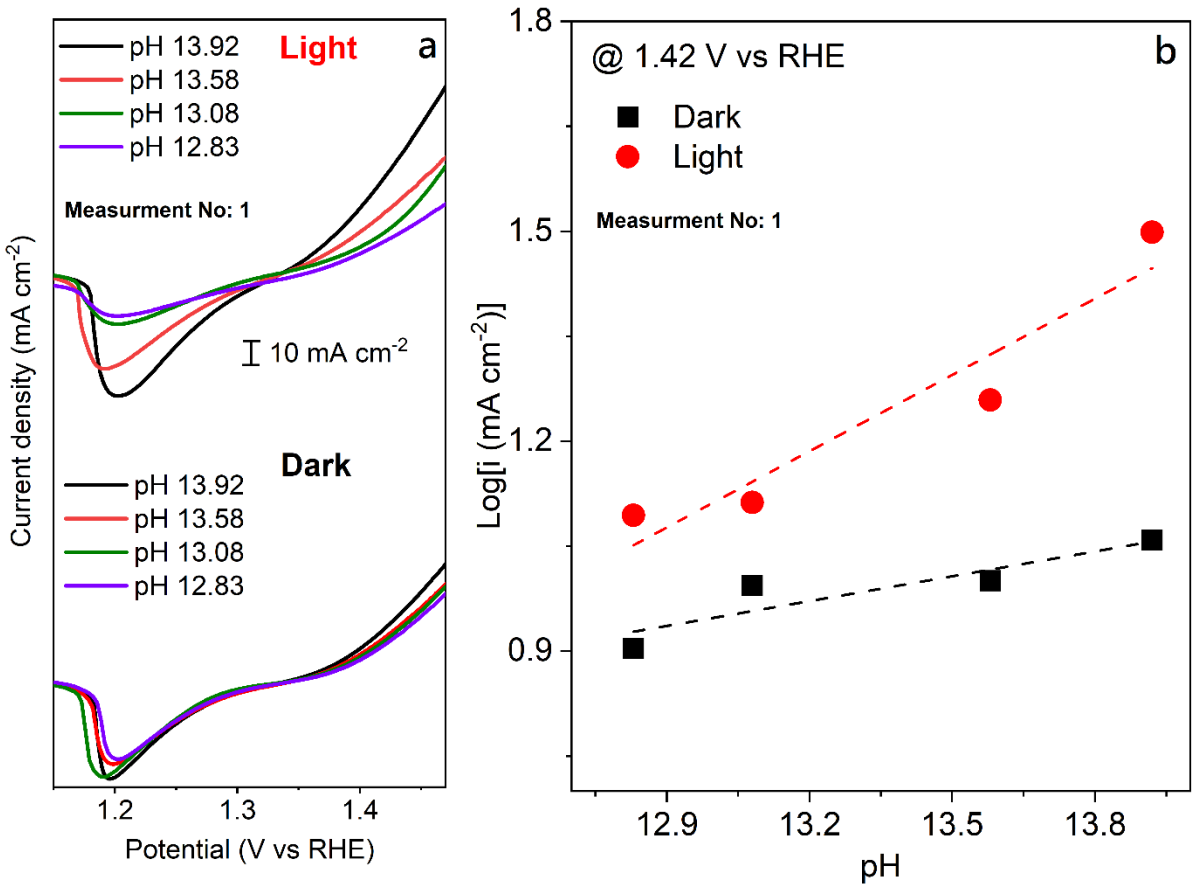

Fig. S21. pH dependence of OER activities of NR-NiOOH exposed to light and stored in dark. The experiment results show that the reaction order of NR-NiOOH subjected to light irradiation is 0.36, which is three times larger than that under dark (0.12). The significant increase in the reaction order indicates the presence of non-concerted proton and electron transfer during the OER process for the sample under light irradiation.

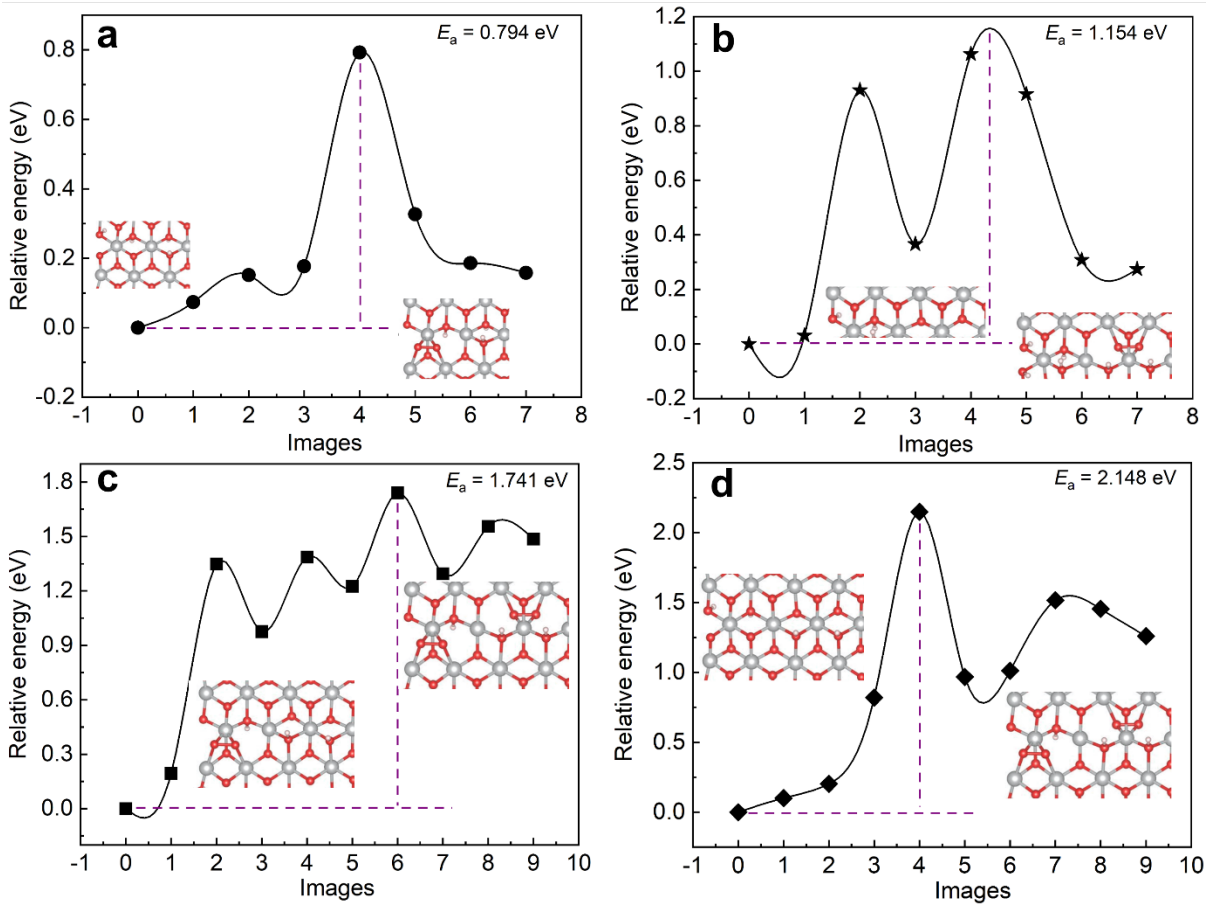

Fig. S22. The kinetic barrier calculation for geometry conversion from octahedral to square planar. To realize the geometry conversion from octahedral to square planar, two neighboring (O-O) coupling will have to occur. For this calculation, two possible pathways were considered, i.e., these two (O-O) couplings occur asynchronously or simultaneously. (a) (b) the energy barrier for (O-O) coupling occurring on edge and inner, respectively. In the asynchronous pathway, the kinetic energy barriers for the (O-O) coupling formation in the edge is 0.794 eV (a) smaller than that of inner (O-O) coupling (b) (1.154 eV), which was believed to be firstly formed. (c)-(d) the energy barrier of asynchronous and simultaneous pathways for geometry from octahedral to square planar, respectively. When the edge (O-O) coupling formed, the energy barrier for the inner (O-O) coupling (c) was 1.741 eV, which was the energy barrier for asynchronous pathway. Since the kinetic barrier based on asynchronous pathway is lower than that of simultaneous pathway, the asynchronous pathway was considered, which means a kinetic energy barrier of 1.741 eV has to be overcome in order for the geometry conversion to occur.

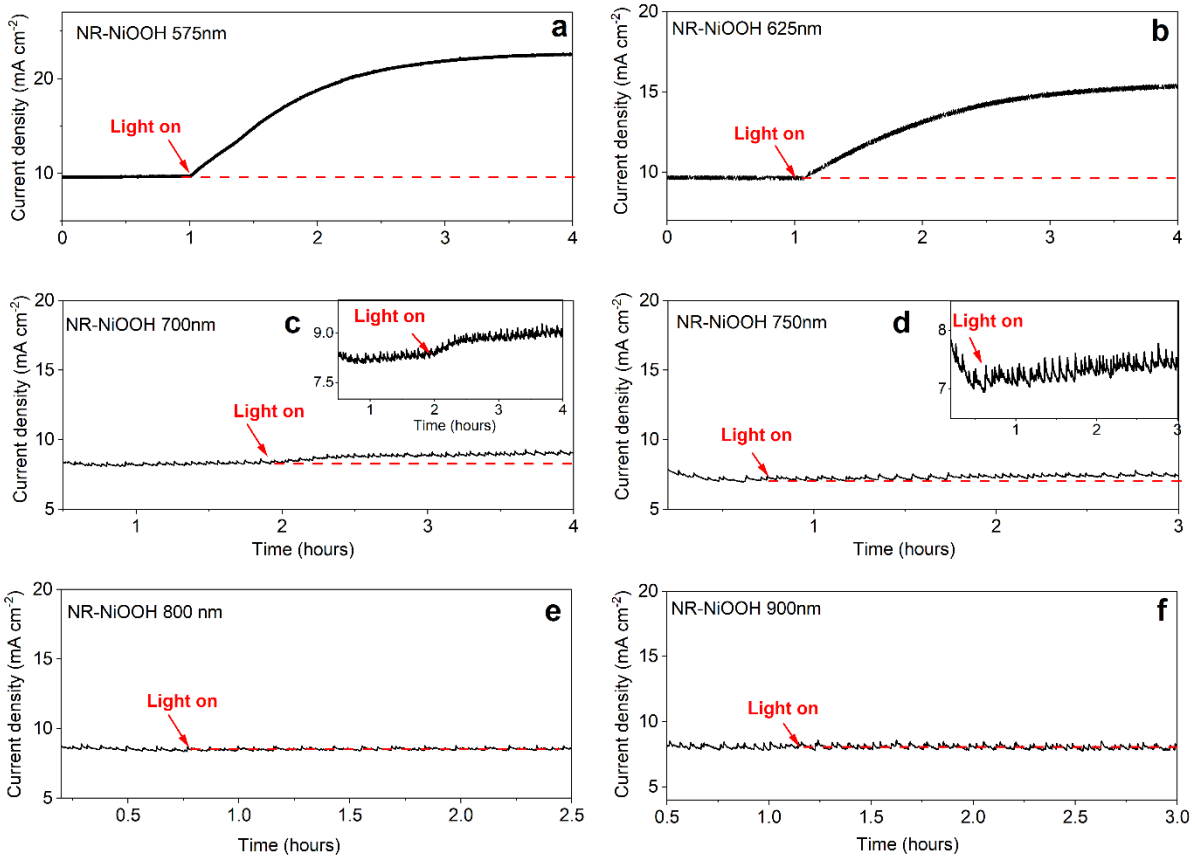

Fig. S23. Photon response measurement. The photon response measurement was equipped with the wavelength filter of 575 nm (a), 625 nm (b), 700 nm (c), 750 nm (d) 800 nm (e) and 900 nm (f), respectively. It is shown that with wavelength of 575 nm and 625 nm, the current increased significantly when light was switch on. As the wavelength used increased to 700 nm, an increase in the current can still be observed. Since the calculated kinetic barrier is about 720 nm, it is expected that the current increment with light source of 750 nm to be greatly weakened. As shown in Fig. S23d, the current increment can be barely observed when a light source of 750 nm was used. This result suggests that the wavelength of 750 nm could trigger COM minimally, which is in good agreement with our calculations. Interestingly, switching on the light source with higher wavelength of 800 nm to 900 nm did not trigger any observable change in the current, which suggests the inability of these wavelengths in triggering COM. This result further validates our calculation of the kinetic energy barrier needed to overcome to trigger COM. Thus, based on these results, it can be concluded that the lowest wavelength that can trigger COM is around 750 nm (1.653 eV), which is relatively close to our calculations (1.741 eV).

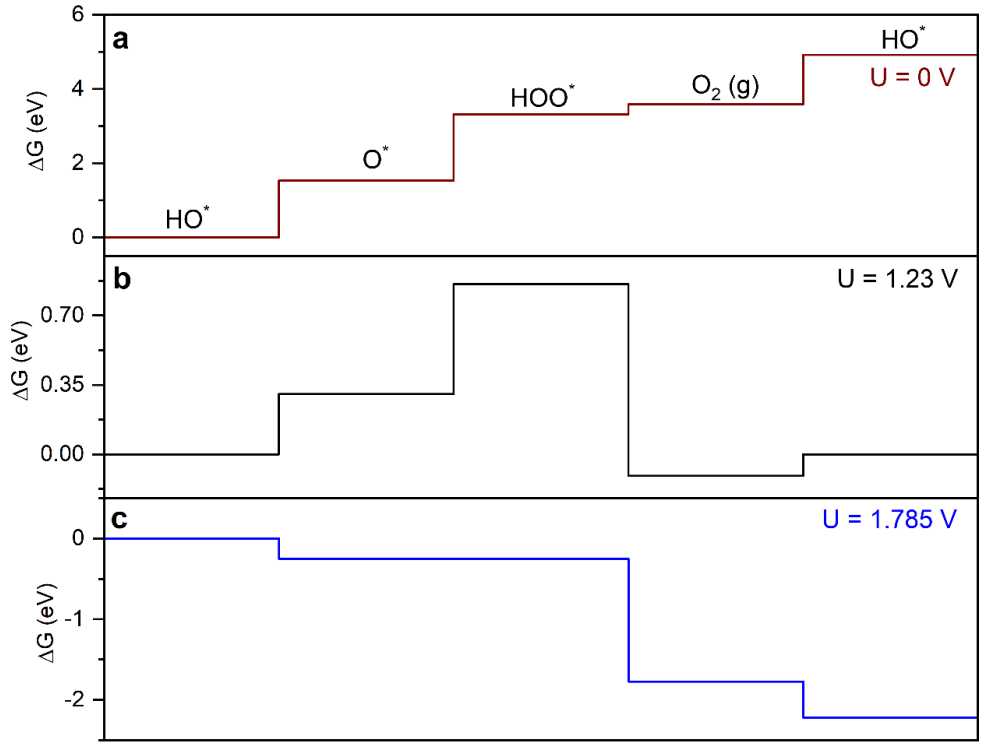

Fig. S24. Calculated reaction free energy change of the AEM route (Solvent) in NR-NiOOH based on the 0V, 1.23 V and the lowest bias potential (1.785 V). The detailed calculation was provided in our previous work (*1*).

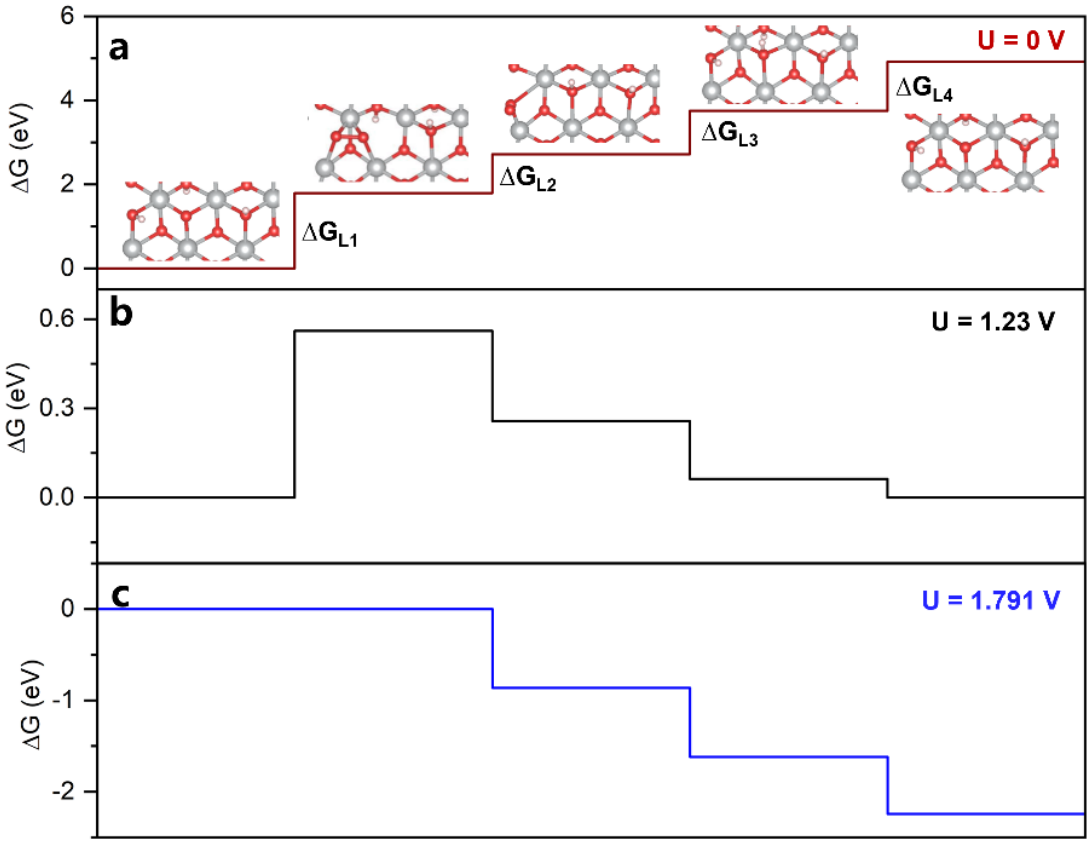

Fig. S25. Calculated reaction free energies of the LOM route based on the 0V, 1.23 V and the lowest bias potential (1.791 V). We conducted the LOM calculations with reference (*4*).

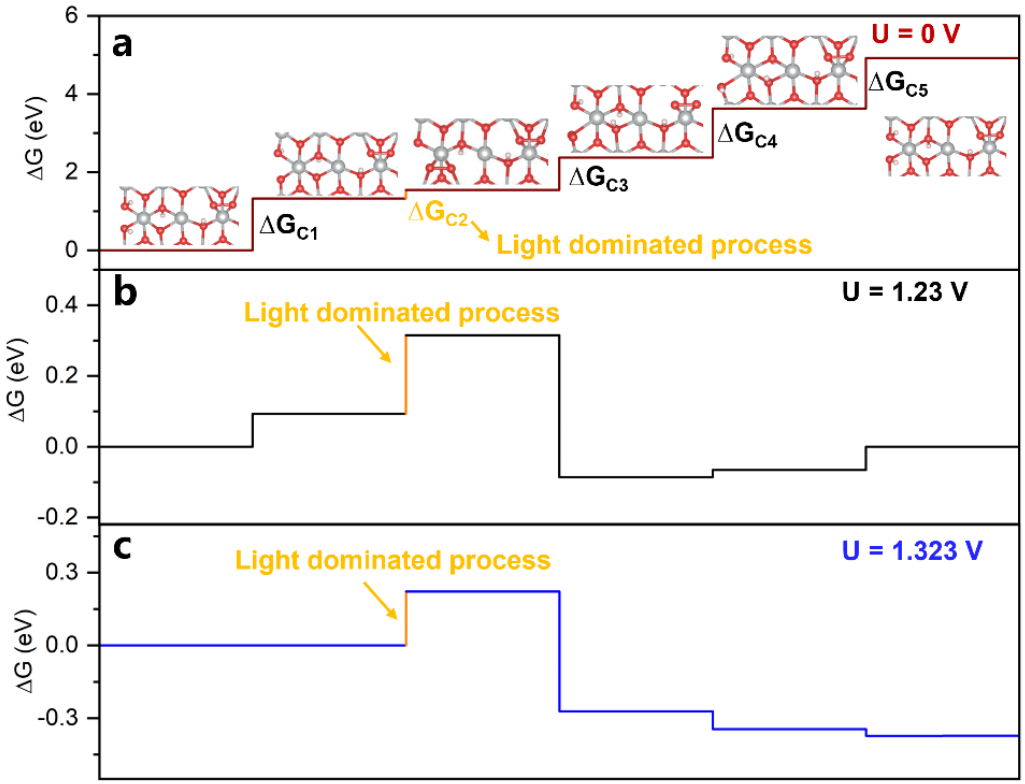

Fig. S26. Calculated reaction free energies of the COM route with a NR-NiOOH with one inner (O-O) coupling as starting models, based on the 0 V, 1.23 V and the lowest bias potential (1.323 V). Here, it should be noted that light-dominated process was a potential independent step. The geometry conversion from octahedral to square planar involves the occurrence of two neighboring (O-O) couplings, and this implies the participation of four oxygen atoms sites in the geometry conversion. Nevertheless, an OER process (with only one O_2 molecule produced) is a four-electron process, and during the OER calculation only one type of O-O bond formation will be considered, *i.e.,* either OOH or (O-O) coupling. To demonstrate the geometry conversion from octahedron to square planar during OER calculation, the following model was employed. A NR-NiOOH with one inner (O-O) coupling was used as the model, whereby it possessed an octahedral configuration with one inner (O-O) coupling. When the OER process follows the COM route, there is a geometry conversion to square planar during the light dominated process. Based on the calculations, the potential limiting step was between C1 to C2, with a calculated overpotential of 0.093 V (Solvent).

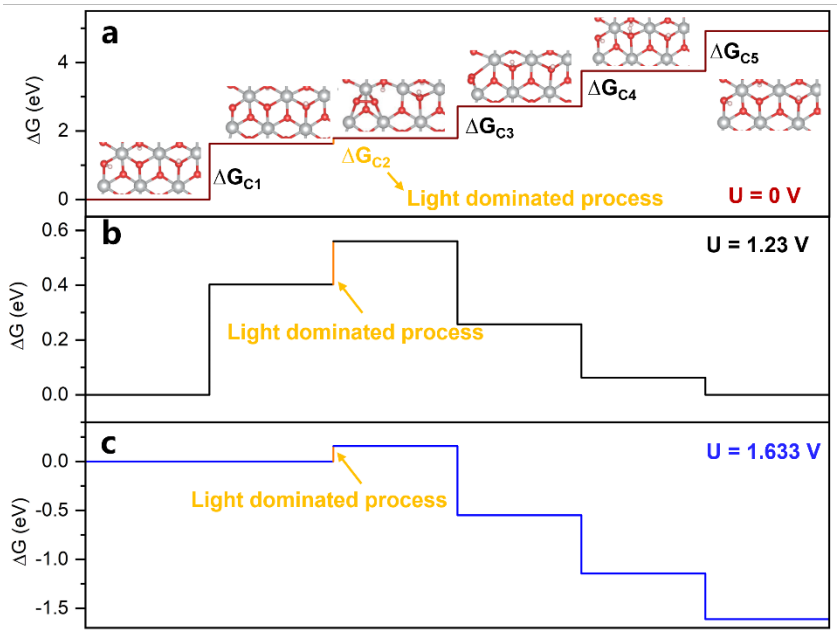

Fig. S27. Calculated reaction free energies (Solvent) of the NR-NiOOH following the same route as COM route, based on the 0V, 1.23 V and the lowest bias potential (1.633 V). Here, it should be noted that light-dominated process was a potential independent step. We performed DFT simulations using NR-NiOOH, i.e., octahedron, as the initial model based on the same route as COM, i.e., the light provides the energy required for (O-O) coupling. It shows that this route follows the same route as COM, while no geometry conversion was demonstrated in the route. In this route, the calculated overpotential was 0.403 V. Since the calculation employed the same model (NR-NiOOH) as that for AEM, we could conclude that it exhibited a lower overpotential (0.403 V) as compared to NR-NiOOH *via* AEM route (0.555 V). Moreover, since the calculation proceeded in the same route as COM, we could conclude that it possessed higher overpotential (0.403 V) as compared to the COM route (0.093 V). Hence, the COM route exhibited a significantly smaller overpotential as compared to the AEM route. In this work, the effect of applied potential on the NR-NiOOH structure was also discussed as shown in Fig. S28, showing that the applied potential does not affect the optimized model and has negligible influence on the DFT calculation results.

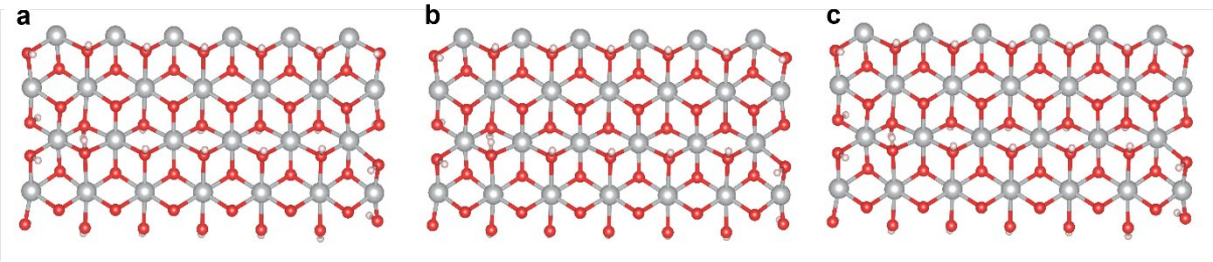

Fig. S28. The relaxed NR-NiOOH structure under the potential of 0 V (a), 1.412 V (b) and 1.785 V (c). The simulation results showed that the surface at 0 V is the same as that at 1.412 V and 1.785 V. Hence, the applied potential does not affect the optimized model and has an ignorable influence on the DFT calculation results.

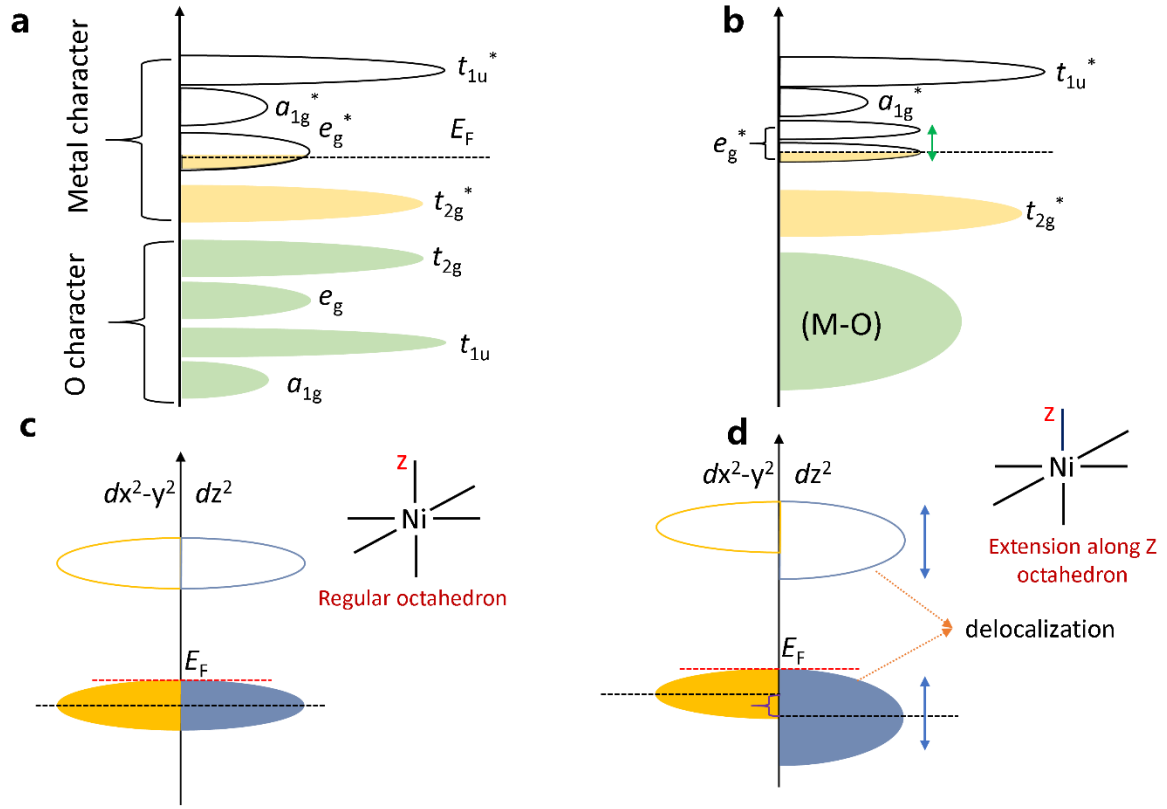

Fig. S29. Schematic illustration of electron variations in consideration of Jahn-Teller distortion. (a) Schematic illustration of the energy bands of octahedral NiO_6. (b) Schematic illustration of the energy bands of NiO_6 with consideration of Jahn-Teller distortion. Due to the [Ar]3d^7 electronic configuration of Ni^{3+}, there is a splitting in the e_g^* band in NiOOH, according to Jahn-Teller distortion. (c) The electronic states of $d_{x^2-y^2}$ and d_{z^2} orbitals for the regular octahedron. (d) The electronic states of $d_{x^2-y^2}$ and d_{z^2} orbitals for the stretched octahedron (extension along z). According to Jahn-Teller distortion, the extension along z would lead to the delocalization of the electronic states of d_{z^2} orbitals (thus becoming broader). As a result, $d_{x^2-y^2}$ and d_{z^2} are no longer considered to be degenerate states as there is a splitting in the e_g^* band in NiOOH. Hence, the energy difference between these two non-degenerate orbitals is associated with the degree of asymmetry in the octahedral configuration.

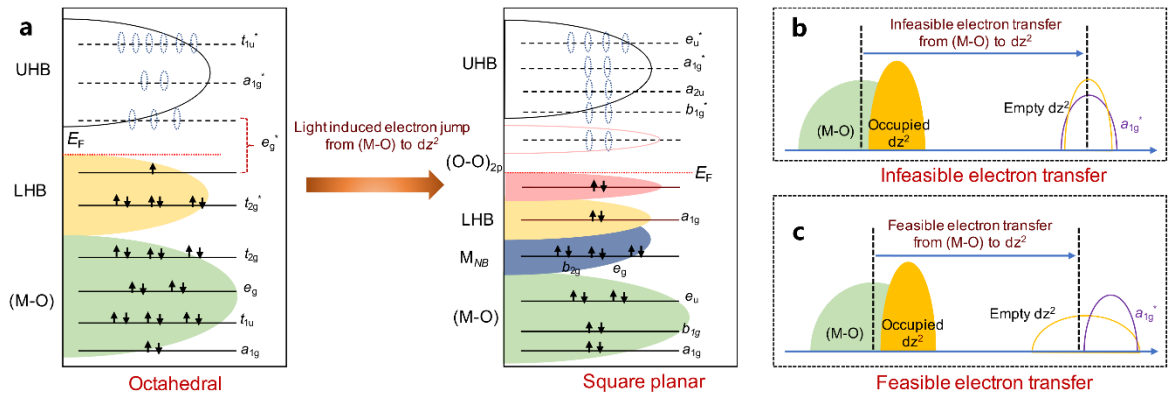

Fig. S30. The origins of the light-induced oxygen evolution route based on an electron transfer pathway that involves switchable metal and oxygen redox centers. (a) schematic electronic configuration of the induced geometry conversion from octahedral to square planar *via* light irradiation. (b) Infeasible electron transfer from (M-O) to d_{z^2} due to the overlapping of d_{z^2} orbital and a_{1g}^* band, and (c) feasible electron transfer from (M-O) to d_{z^2} due to the partial overlapping of empty d_{z^2} orbital and a_{1g}^* band. Based on the position of the empty d_{z^2} orbitals, two types of electron configurations are possible: (1) d_{z^2} orbitals completely overlap with a_{1g}^* bands (Fig. S30b). In this case, the electronic states in the overlapping region mainly originate from the contribution of Ni 4*s* orbitals. However, the electron transfer from (M-O) to 4*s* orbitals is unlikely to occur since electron will fill the 3*d* orbitals rather than 4*s* orbitals to achieve a more stable electronic configuration, *i.e.*, [Ar]$3d^8$. Consequently, the electron transfer from (M-O) to d_{z^2} orbital in this case is difficult. (2) d_{z^2} orbitals partially overlap with a_{1g}^* bands, of which the electronic states in the non-overlapping region are contributed from Ni 3*d* orbitals (Fig. S30c). In this case, the electron transfer from (M-O) to d_{z^2} orbital can be realized since electron will fill the 3*d* orbitals preferentially. Thus, to realize COM, it is necessary that there is a non-overlapping region of d_{z^2} orbitals with a_{1g}^* bands so that electron can be transferred from (M-O) to d_{z^2} orbitals.

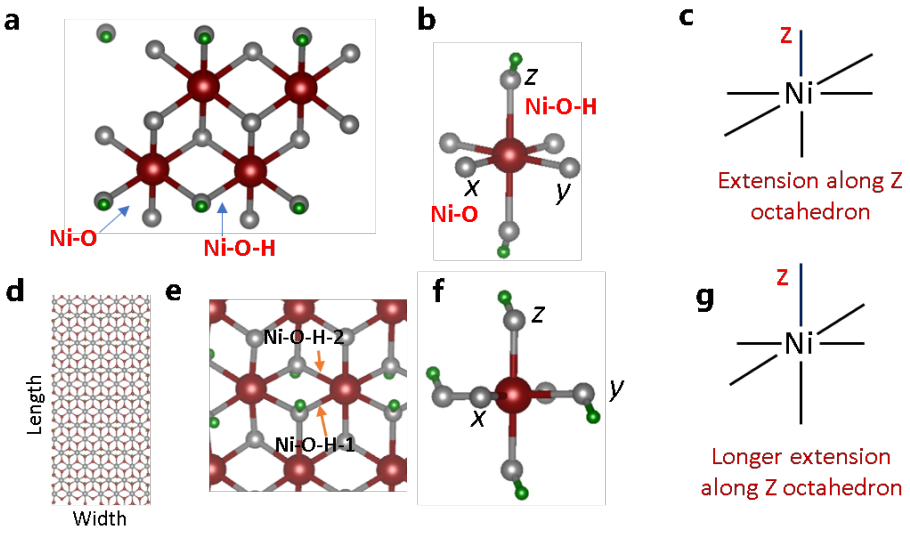

Fig. S31. The structures of bulk NiOOH and NR-NiOOH. (a) The structure of traditional NiOOH. (b) The Ni-O configurations in traditional NiOOH. According to the relaxed bulk NiOOH model, there are two types of Ni-O bond configurations, *i.e.*, Ni-O (1.98 Å) and Ni-O-H (1.88 Å). (c) The schematic of bulk NiOOH structure. (d) The model of NR-NiOOH. NR-NiOOH is a strain stabilized double/triple layer nickel oxyhydroxide nanoribbon structure, with 2-5 nm in width and 10-20 nm in length (*l*). (e) The enlarged NR-NiOOH structure. (f) The Ni-O configurations in NR-NiOOH. According to the relaxed NR-NiOOH model, three types of Ni-O bond configurations are present, *i.e.*, Ni-O (1.84 Å), Ni-O-H-1 (1.95 Å), and Ni-O-H-2 (2.01 Å) for the edge octahedron of NR-NiOOH structure (d to f). This is in contrast to the two types of Ni-O bond configurations, *i.e.*, Ni-O (1.98 Å) and Ni-O-H (1.88 Å), present in bulk NiOOH. This result indicates that our NR-NiOOH possesses a greater degree of asymmetry as compared to the bulk NiOOH. (g) The schematic of bulk NiOOH structure. Obviously, the structure of NR-NiOOH is a more extended (along z) octahedron, as compared with the structure of traditional NiOOH.

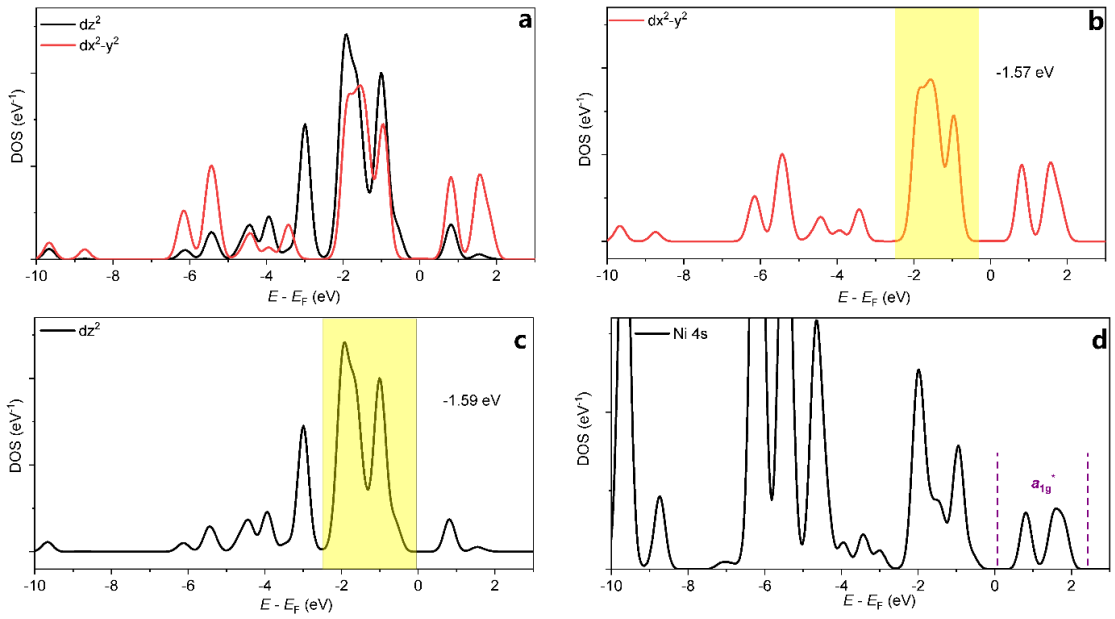

Fig. S32. The projected density of states (PDOS) of bulk NiOOH. (a) PDOS of $d_{x^2-y^2}$ and d_{z^2} orbitals. (b) (c) The schematic illustration of the band centre of $d_{x^2-y^2}$ and d_{z^2} orbitals, obtained from calculations. The orbital energy difference value for bulk NiOOH is determined to be 0.02 eV. (d) PDOS of $a_{1g}{}^{*}$ bands. The region above Fermi level completely overlaps with that of d_{z^2} orbitals, which indicates that the electronic states above Fermi level mainly show the character of Ni 4*s* orbital.

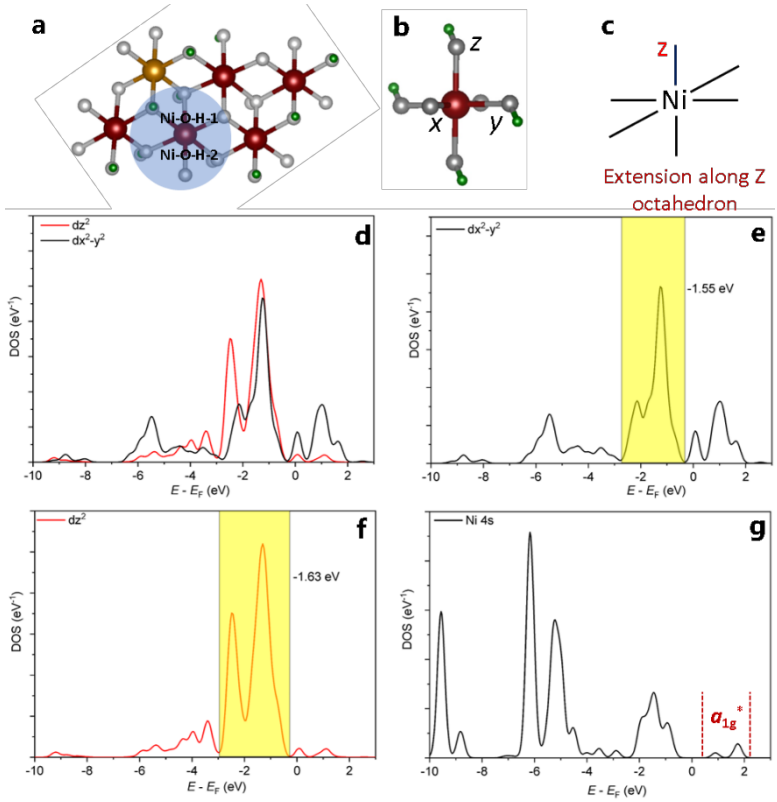

Fig. S33. The PDOS of NiFe LDH. (a) The structure of NiFe LDH. Brown circles show Ni atoms and yellow circle represents Fe atoms, respectively. (b) The Ni-O configurations in NiFe LDH. According to the relaxed NiFe LDH model, three types of Ni-O bond configurations are present, *i.e.*, Ni-O (1.95 Å), Ni-O-H-1 (2.08 Å), and Ni-O-H-2 (1.93 Å) for the Ni octahedron near Fe atoms. (d) The PDOS of $d_{x^2-y^2}$ and d_{z^2} orbitals. (e) (f) The schematic illustration of the band centre of $d_{x^2-y^2}$ and d_{z^2} orbitals, obtained from calculations. The orbital energy difference value of NiFe LDH is 0.08 eV. (g) The PDOS of $a_{1g}{}^{*}$ bands.

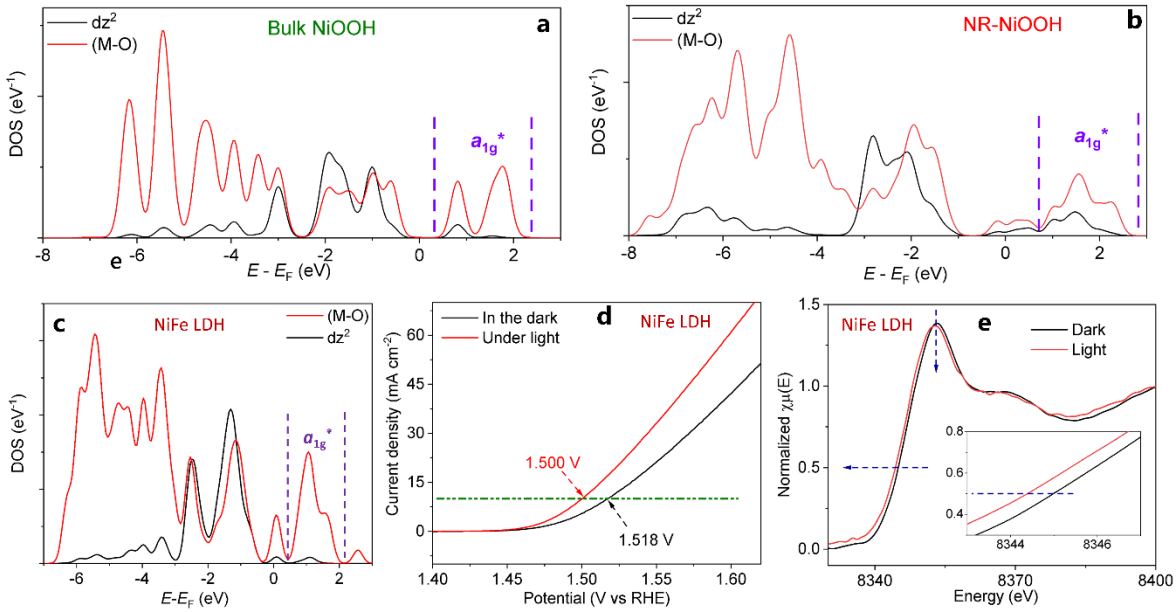

Fig. S34. The PDOS, electrochemical and XANES spectra of NiFe LDH. (a) (b) PDOS of d_{z^2} orbital and (M-O) bands for traditional NiOOH and NR-NiOOH. (c) The PDOS of d_{z^2} orbital and (M-O) bands for traditional NiFe LDH. (d) OER polarization curves of NiFe LDH subjected to and without light irradiation, respectively; (e) *Operando* Ni *K*-edge XANES spectra of NiFe LDH subjected to light and in dark condition (inset showing the enlarged Ni *K*-edge XANES spectra in the range of 8343 to 8347 eV).

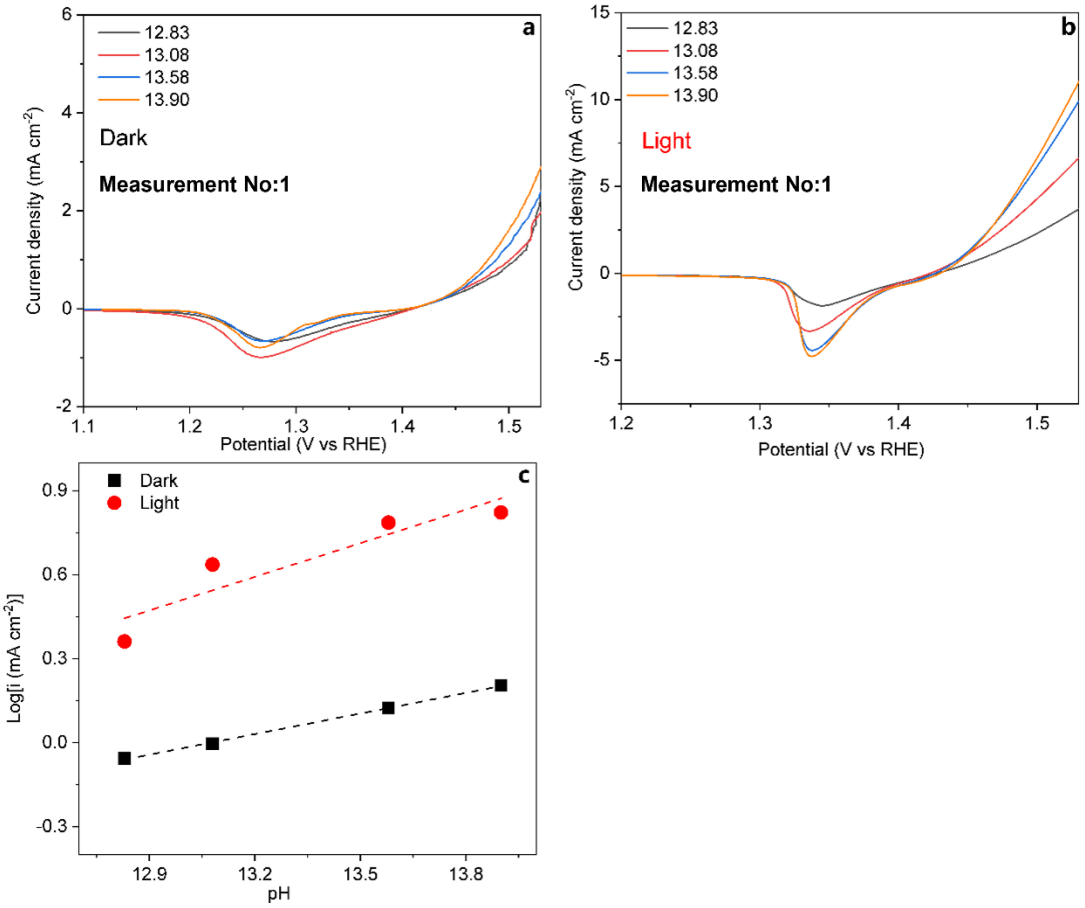

Fig. S35. The pH dependence NiFe LDH in the dark (a) and light (b). (c) current densities of NiFe-LDH subjected to and without light irradiation at 1.50 V vs RHE as a function of pH. According to the results, NiFe LDH exhibits a more obvious pH dependency (0.40) when subjected to light irradiation as compared to that in dark condition (0.15).

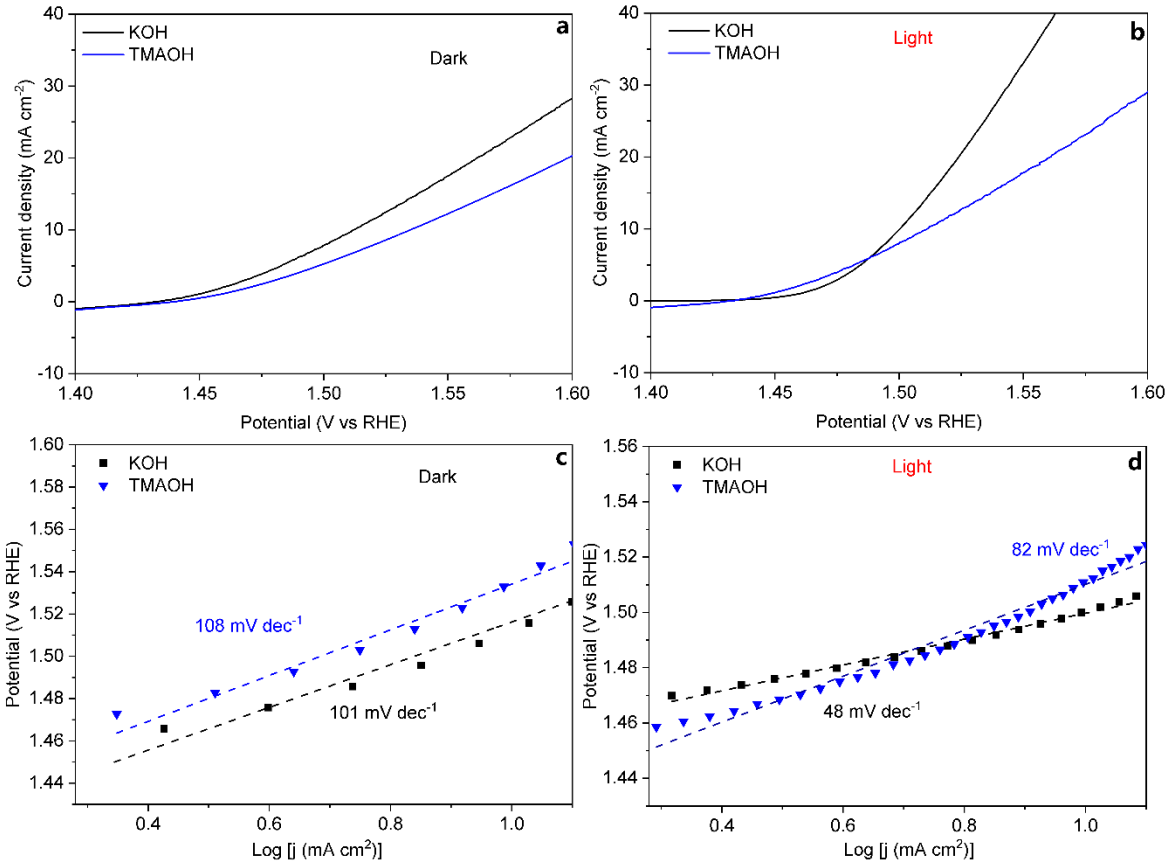

Fig. S36. The LSV and Tafel slopes of NiFe LDH in the dark (a) and (c), and light (b) and (d) in KOH, and TMAOH electrolyte.

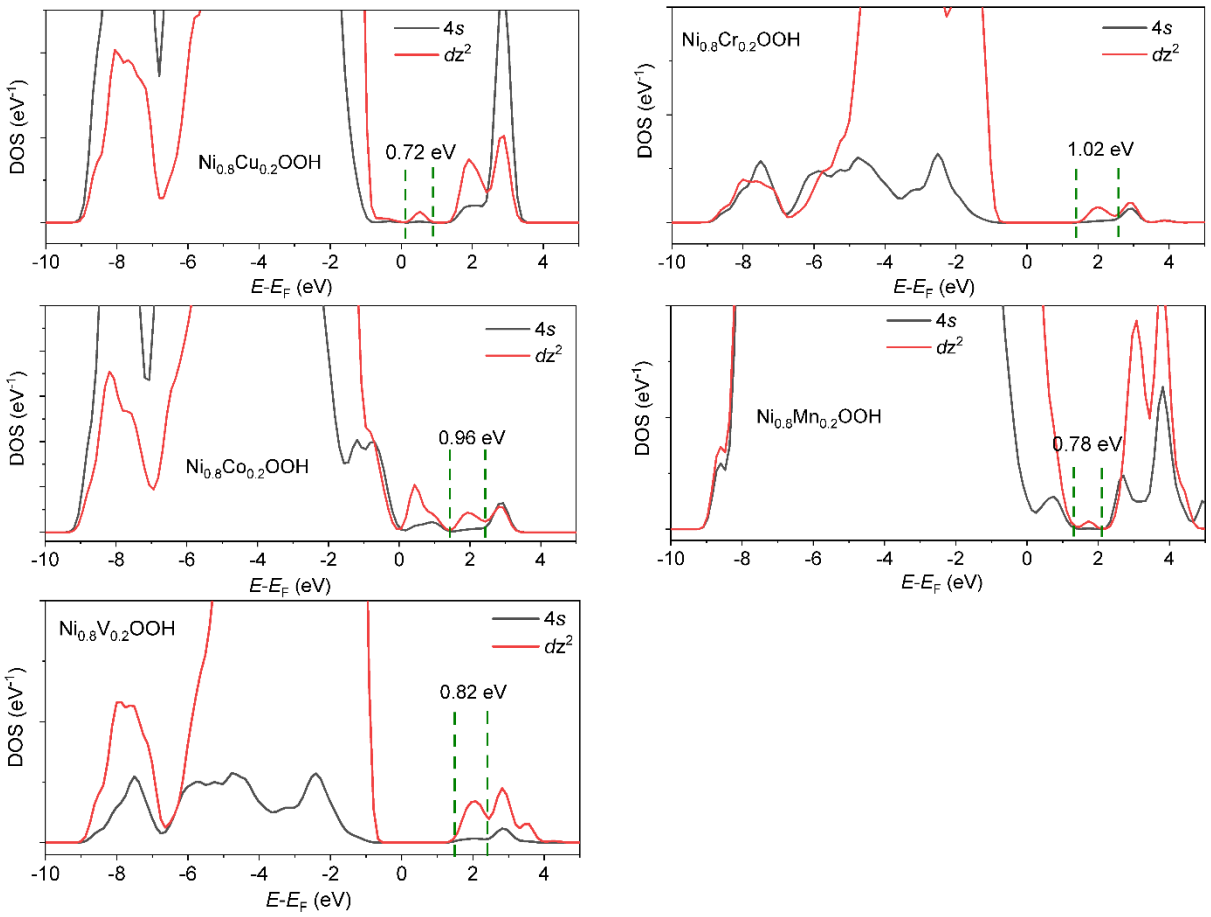

Fig. S37. The PDOS of $Ni_{0.8}Cu_{0.2}OOH$, $Ni_{0.8}Cr_{0.2}OOH$, $Ni_{0.8}Co_{0.2}OOH$, $Ni_{0.8}Mn_{0.2}OOH$, and $Ni_{0.8}V_{0.2}OOH$. Here, the PDOS of 4*s* orbital above Fermi level shows the electronic states of a_{1g}^* bands. According to the simulation results, non-overlapping regions were observed in all materials due to the partial overlapping of d_{z^2} orbitals with a_{1g}^* bands.

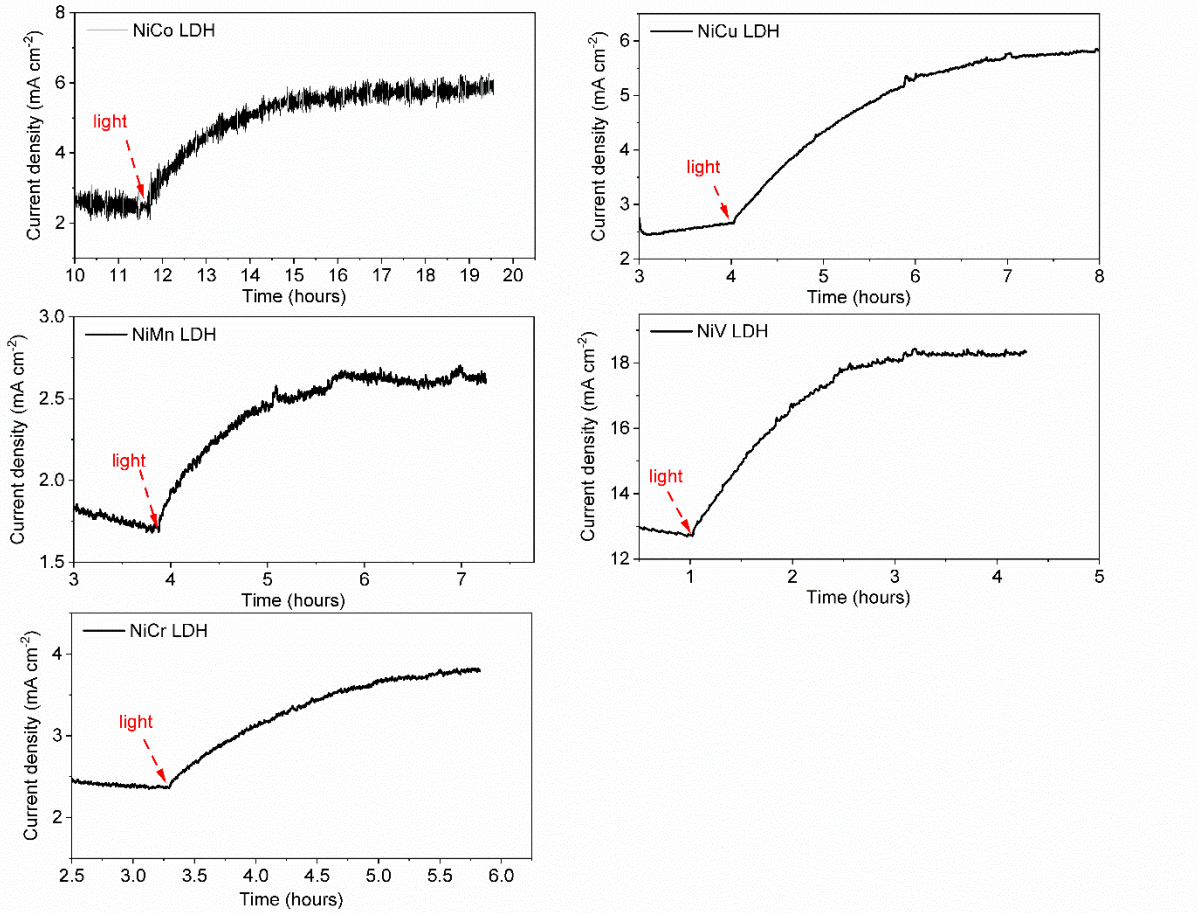

Fig. S38. Photon response measurements in NiCrOOH, NiMnOOH, NiVOOH, NiCoOOH, and NiCuOOH measured at the potential of 1.50 V vs RHE. It is shown that COM can be successfully triggered in NiCrOOH, NiMnOOH, NiVOOH, NiCoOOH, and NiCuOOH. Such a result clearly demonstrates the universality of our proposed COM in various electrocatalysts.

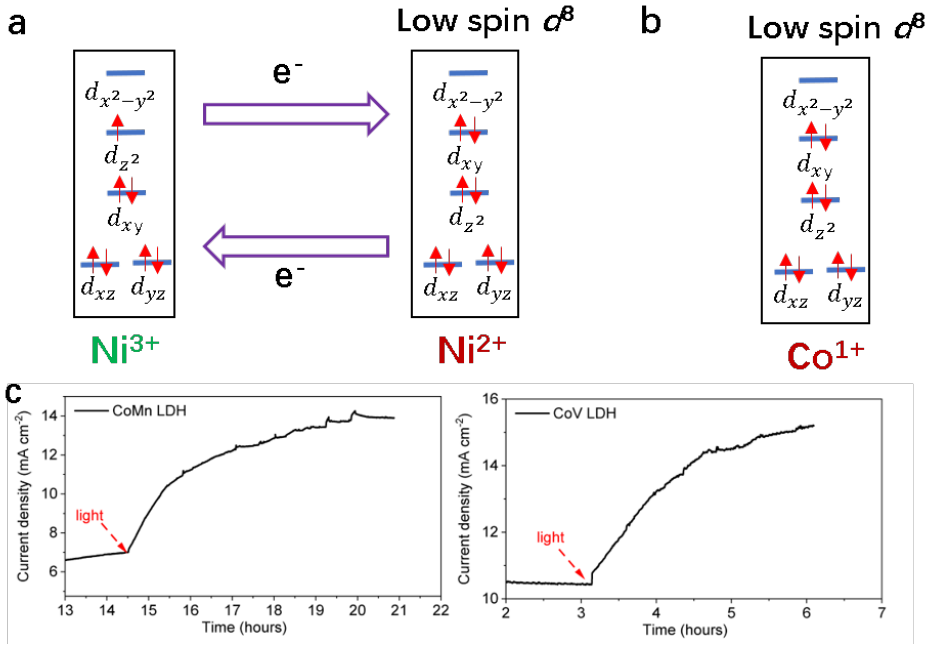

Fig. S39. The analysis of COM mechanism in Co based oxyhydroxides species. (a) Electronic configurations of Ni^{3+} and low spin Ni^{2+}. (b) Possible electronic configuration of low spin Co^{1+}. (c) Photon response measurements in CoMn and CoV LDH. According to our work, the key in triggering COM route is to realize the geometry conversion from octahedron to square planar (Fig. S39a). This means that COM may be triggered when such a geometry conversion is fulfilled in non-Ni-based compositions. When compared to Ni electronic configuration, *i.e.*, [Ar]3*d*84*s*2, Co follows the configuration of [Ar]3*d*74*s*2, which has one less electron. As a result, Co^{1+} may also possess a low spin d^8 electronic configuration while exhibiting the square planar geometry, which is similar to that of the low spin Ni^{2+}. More importantly, both Co^{2+} and Co^{3+} follow the octahedral configuration. Interestingly, we also found light-triggered OER performance enhancement in Co-base compositions, *i.e.*, CoMn LDH and CoV LDH, as shown in Fig. S39c. These results implies that photon-induced COM might be triggered in Co-base compositions. The mechanism of photon-induced COM in Co-based compositions has to be further studied.

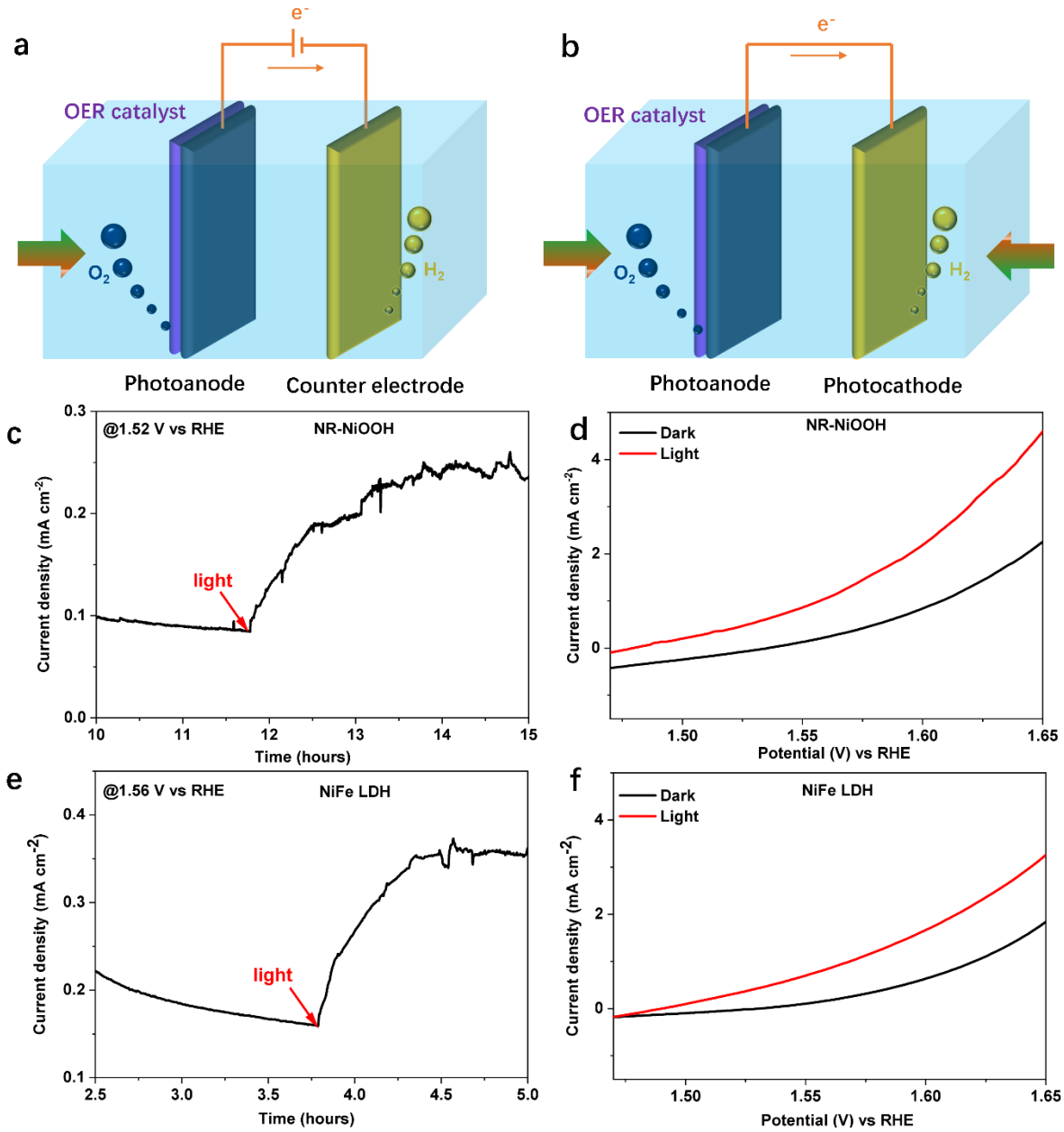

Fig. S40. OER activities of NR-NiOOH and NiFe LDH in neutral conditions, with and without light irradiation. (a) and (b) show the schematic illustrations of photoanode and tandem configurations. (c) and (e) light response test of NR-NiOOH and NiFe LDH using chronoamperometry measurement at the potential of 1.52 V and 1.56 V vs. reversible hydrogen electrode (RHE), respectively. (d) and (f) OER polarization curves of NR-NiOOH and NiFe LDH recorded under a scan rate of 0.1 mV/s with and without light irradiation. These artificial photosynthesis devices usually operate under neutral conditions. To determine the feasibility of COM actualization under neutral conditions, photon response measurement of NR-NiOOH and NiFe LDH was conducted in phosphate buffer solution (0.1 M, pH = 7). The experiment

results obtained under neutral conditions exhibited the same behavior as that in alkaline conditions, whereby there was an obvious increase in current density under light irradiation. As such, based on this result, COM can still be triggered by light irradiation under neutral conditions. Thus, it is believed that our proposed COM can benefit the development of artificial photosynthesis devices.

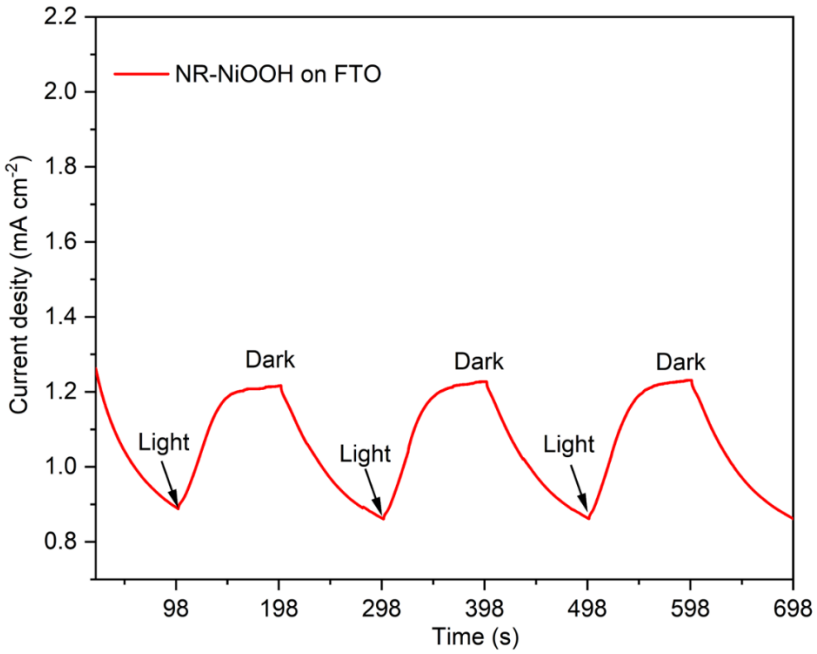

Fig. S41. The light response test of NR-NiOOH on FTO (Fluorine-doped Tin Oxide) glass.

In our work, the light response test on FTO was conducted using chronoamperometry measurement at a potential of 1.40 V *vs.* reversible hydrogen electrode (RHE). For the NR-NiOOH that is grown on a FTO (fluorine-doped tin oxide) glass, the activation process still requires a long time (>50 s).

Table S1. Comparison of the OER catalytic performances of NR-NiOOH under light irradiation and selected previously reported OER catalysts.

Catalyst	Electrolytes	Loading mass (mg)	Overpotential (mV) at 10 mA cm^{-2}	Tafel slope	Ref
G-FeCoW	1 M KOH	0.210	191	-	*Science* **352,** 333-337, 2016
$Ni_xFe_{1-x}Se_2$-DO	1M KOH	4.100	195	28	*Nat. Commun.* **7,** 12324, 2016
Ni_3N COF	1M KOH	0.005	230	79	*Adv. Energy. Mater.* **6,** 1601189, 2016
Co_3O_4/N-rmGO	1 M KOH	0.100	310	67	*Nat. Mater.* **10,** 780-786, 2011
CoZnOOH	1M KOH	0.204	285	35	*Nat. Ener.* **4,** 329-338, 2019
PBSCF-III	0.1M KOH	0.202	358	52	*Nat. Commun.* **8,** 14586, 2017
$Ba_{0.5}Sr_{0.5}Co_{0.8}Fe_{0.2}O_3$	0.1M KOH	0.250	370	-	*Science* **334,** 1383-1385, 2011
$CaFeO_3$	0.1M KOH	0.250	390	47	*Nat. Commun.* **6,** 8249, 2015
NiCo-UMOFENs	1 M KOH	0.200	189	65	*Nat. Ener.* **1,** 16184, 2016
IrO_2	1M KOH	-	325	54	*J. Am. Chem. Soc.* **135,** 16977-16987, 2013
NiFe/NF	1M KOH	0.450	215	28	*Nat. Commun.* **6,** 6616, 2015
FeNi-rGO LDH	1M KOH	0.250	206	39	*Angew. Chem. Int. Ed.* **53,** 7584, 2014
$NiFeO_x$/C	0.1M KOH	0.008 (only metals)	290	-	*Catal. Today.* **65,** 262, 2016
NiFe LDH	1 M NaOH	0.050	260	21	*Nanoscale Horiz.,* **1,** 156, 2016
NR-NiOOH under light irradiation	1 M KOH	0.420	135	31	Our work

Table S2. Comparison of the current normalized to actual surface area of NR-NiOOH under light irradiation and selected previously reported OER catalysts. C_s is specific capacitance calculated from ECSA measurement; j (mA $cm^{-2}_{specific}$) is the normalized current at a potential 1.50 V vs RHE (if not, the potential was provided).

Catalyst	Electrolytes	Method/(C_s)	j (mA $cm^{-2}_{specific}$)	Ref
IrO_2 NP	0.1 M $HClO_4$	TEM	0.010	*J. Phys. Chem. Lett.* **3,** 399, 2012
RuO_2 NP	0.1 M $HClO_4$	TEM	0.020	
RuO_2/C	0.5 M H_2SO_4	ECSA (0.035)	0.800	*Nat. Commun.* **10,** 4849, 2019
Ru-N-C	0.5 M H_2SO_4	ECSA (0.035)	0.850	
$Cr_{0.6}RuO_2$ (550)	0.5 M H_2SO_4	ECSA (0.035)	0.04 (1.45 V)	*Nat. Commun.* **10,** 162, 2019
$Ru_{0.7}Ni_{0.3}O_{2-y}$	0.1 M $HClO_4$	SEM	0.080	*J. Solid State Electrochem.* **13,** 959, 2009
La_2LiIrO_6	0.05 M H_2SO_4	TEM	0.600	*Nat. Energy* **2,** 16189, 2016
Sputter RuO_2	0.05 M H_2SO_4	Geometric surface area	1.050	*ChemElectroChem* **1,** 2075, 2014
$IrO_x/SrIrO_3$	0.5 M H_2SO_4	Geometric surface area	7.300 0.32 (1.45 V)	*Science* **353,** 1011, 2016
$LaCoO_3$	0.1M KOH	BET	0.009	*Nat. Chem.* **9,** 457, 2017
$La_{0.5}Sr_{0.5}CoO_{3-\delta}$	0.1M KOH	BET	0.017	
$SrCoO_{3-\delta}$	0.1M KOH	BET	0.300	
$CaCu_3Fe_4O_{12}$	0.1M KOH	BET	0.045	*Nat. Commun.* **6,** 8249, 2015
Co_3O_4/CeO_2	0.5 M H_2SO_4	ECSA (0.035)	0.024 (1.68V)	*Nat. Commun.* **12,** 3036, 2021
$NaNiO_2$	1 M KOH	ECSA (0.04)	0.35 (1.58 V)	*Energy Environ. Sci.,* **10,** 121, 2021
$NaNi_{0.9}Fe_{0.1}O_2$	1 M KOH	ECSA (0.04)	1.15 (1.58 V)	
IrO_x/9R-$BaIrO_3$	0.5 M H_2SO_4	ECSA (0.035)	0.50 (1.49 V)	*J. Am. Chem. Soc.* **143,** 18001, 2021
CoO_x	1 M KOH	ECSA (0.04)	0.09 ± 0.04 (1.58 V)	
$CoFeO_x$	1 M KOH	ECSA (0.04)	0.4 ± 0.2 (1.58 V)	

NiO_x	1 M KOH	ECSA (0.04)	0.12 ± 0.05 (1.58 V)	*J. Am. Chem. Soc.* **135,** 16977, 2013
$NiCoO_x$	1 M KOH	ECSA (0.04)	0.2 ± 0.1 (1.58 V)	
NR-NiOOH under light irradiation	1 M KOH	ECSA (0.04)	1.230 0.730 (1.45V)	**Our work**

Table S3. Comparison of the current normalized to loading mass of NR-NiOOH under light irradiation and selected previously reported OER catalysts.

Catalyst	Electrolytes	j (A mg^{-1}) at potential 1.50 V vs RHE	Ref
IrO_2 NP	0.1 M $HClO_4$	0.007	*J. Phys. Chem. Lett.* **3,** 399, 2012
RuO_2 NP	0.1 M $HClO_4$	0.030	
$IrNi_{3.3}$ NP	0.05 M H_2SO_4	0.180	*Chem. Sci.* **5,** 2955, 2014
$2.9*10^6$ u Ru NP	0.05 M H_2SO_4	0.040 (1.40 V)	*Chem. Sci.* **6,** 190, 2015
BCFSn-721	0.1 M KOH	0.081 (1.68 V)	*Adv. Sci.* **3,** 1500187, 2016
Co-Fe-O frames	1 M KOH	0.170 (1.53 V)	*Chem* **4,** 1967-1982, 2018
$LaCo_{0.8}Fe_{0.2}O_3$	0.1M KOH	0.004 (1.52 V)	*Energy Environ. Sci. 11, 2945-2953, 2018*
SrCoO0.85-δFe0.15	1M KOH	0.093 (1.65 V)	*J. Mater. Chem. A* **7,** 12538-12546, 2019
NR-NiOOH under light irradiation	1 M KOH	0.036 (1.40 V) 0.140 (150 V)	**Our work**

Table S4. Comparison of turnover frequency (TOF) of NR-NiOOH under light irradiation and selected previously reported OER catalysts.

Catalyst	Electrolytes	turnover frequency (s^{-1})	Ref
Co_3O_4	1 M KOH	0.09 (1.62 V) 0.02 (1.56 V)	*J. Phys. Chem. Lett.* **113,** 33, 2009
CoO	1 M KOH	0.040 (1.74 V)	*ChemSusChem.* **4,** 1566-1569, 2011
RuO_2	0.5 M H_2SO_4	0.005 (1.46 V)	*Nat. Commun.* **10,** 162, 2019
$Cr_{0.6}Ru_{0.4}O_2$	0.5 M H_2SO_4	0.080 (1.46 V)	
Graphene-NiFe	1 M KOH	0.030 (1.53 V)	*Sci. Adv.* **4,** eaap7970, 2018
IrO2-RuO_2	0.5 M H_2SO_4	0.003 (1.55 V)	*J. Mater. Chem. A* **5,** 17221-17229, 2017
NR-NiOOH under light irradiation	1 M KOH	0.030 (1.45 V) 0.050 (150 V)	**Our work**

Table S5. EXAFS fitting results of NR-NiOOH under dark and NR-NiOOH under light irradiation (light-c in Fig. 3a), where CN is the coordination number, R is the bond length and σ^2 is the Debye-Waller factor.

Samples	Bond species	CN	R (Å)	σ^2 (Å^2)	R factor
NR-NiOOH under dark	Ni-O	5.1±0.5	1.85±0.01	0.0056±0.0006	0.0050
NR-NiOOH under light	Ni-O	3.8±0.6	1.87±0.01	0.0074±0.0029	0.0110

Table S6. Corrections to the Gibbs free energies (in eV) for LOM and COM routes. Note that the correction of AEM is provided in our previous work (*1*).

COM		Solvent	
		energy (eV)	ΔZPE-TΔS (eV)
1	$E(OH^* + OH^*)$	-510.7089	0.2440
2	$E(O^* + OH^*)$	-505.7059	0.2187
3	$E(O^* + O^*)$	-499.5704	0.0485
4	$E(O\text{-}O)$	-499.7879	0.0437
5	$E(OO^* + OH^*)$	-510.2358	0.0601

LOM		Solvent	
		Energy (eV)	ΔZPE-TΔS (eV)
1	$E(OH^* + OH^*)$	-511.6323	0.2127
2	$E(O^* + OH^*)$	-506.2403	0.2914
3	$E(O\text{-}O)$	-501.3309	0.0529
4	$E(OO^* + OH^*)$	-511.7353	0.0748

Supplementary References:

1. Wang, X. *et. al.* Strain stabilizing nickel hydroxide nanoribbons for efficient water splitting. *Energy Environ. Sci.* **13**, 229 (2020).

2. Mathew, K., Sundararaman, R., Letchworth-Weaver, K., Arias, T. & Hennig, R. Implicit solvation model for density-functional study of nanocrystal surface and reaction pathways. *J. Chem. Phys.* **140**, 084106 (2014).

3. Mueller, D. N., Machala, M. L., Bluhm, H., Chueh, W. C. Redox activity of surface oxygen anions in oxygen-deficient perovskite oxides during electrochemical reactions. *Nat. Commun.* **6**, 6097 (2015).

4. Huang, Z. F. *et. al.* Chemical and structural origin of lattice oxygen oxidation in Co-Zn oxyhydroxide oxygen evolution electrocatalysts. *Nat. Ener.* **4**, 329-338 (2019).

5. Nitopi, S. *et. al.* Progress and perspectives of electrochemical CO_2 reduction on copper in aqueous electrolyte. *Chem. Rev*. **119**, 7610-7672 (2019).

6. Nong, H. N. *et. al.* Key role of chemistry versus bias in electrocatalytic oxygen evolution. *Nature* **587**, 408-413 (2020)

7. Fletcher, S. Tafel Slopes from first principles. *J. Solid. State Electrochem.* **19**, 537-549 (2009).

8. Shinagawa, T., Garcia-Esparza, A. & Takanabe, K. Insight on tafel slopes from a microkinetic analysis of aqueous electrocatalysis for energy conversion. *Sci. Rep.* **5**, 13801 (2015).

9. Giordano, L. *et al.* pH-dependence of OER activity of oxides: current and further perspectives. *Catal. Today.* **262**, 2-10 (2016).

10. Yang, C., Fontaine, O., Tarascon, J. & Grimaud, A. Chemical recognition of active oxygen species on the surface of oxygen evolution reaction electrocatalysts. *Angew. Chem*. **129**, 8778-8782 (2017).

11. Trzesniewski, B. J. *et. al.* In situ observation of active oxygen species in Fe-containing Ni-based oxygen evolution catalysts: the effect of pH on electrochemical activity. *J. Am. Chem. Soc.* **137**, 15112-15121 (2015).

12. Hao, Y. *et al.* Recognition of surface oxygen intermediates on NiFe oxyhydroxide oxygen-evolving catalysts by homogeneous oxidation reactivity. *J. Am. Chem. Soc.***143**, 1493-1502 (2021).

13. Roy, C. *et al.* Impact of nanoparticles size and lattice oxygen on water oxidation on $NiFeO_xH_y$. *Nat. Catal.* **1**, 820-829 (2018).

14. Zhang, F. *et al.* Decoupled redox catalytic hydrogen production with a robust electrolyte-Borne electron and proton carrier. *J. Am. Chem. Soc.* **143**, 223-231 (2021).

Appendix: All models: Optimized POSCARs (CONTCARs)

LOM process: NR-NiOOH CONTCAR

1.00000000000000

30.0000000000000000 0.0000000000000000 0.0000000000000000

0.0000000000000000 10.1043996811000003 0.0000000000000000

0.0000000000000000 0.0000000000000000 25.0000000000000000

Ni O H

26 52 28

Direct

0.2198606994368229 0.2562480745653937 0.1366069927738013

0.2209363111622197 0.7553940197889879 0.1444886102471935

0.2616623406009637 0.0058360154066346 0.1396460262727998

0.2641516071341274 0.5055608004640191 0.1402495967087032

0.3125865176103171 0.2519644277127170 0.1386566277694262

0.3132615940528166 0.7574185872167595 0.1408135734675511

0.3605028883257202 0.0041056923729190 0.1393626643945755

0.3606141271829005 0.5041642017436917 0.1394667013542762

0.4093951923358513 0.2521269472424256 0.1394757742739901

0.4096958757828185 0.7533719718444051 0.1389612912290804

0.4581177171937008 0.0016499646174838 0.1392373694066567

0.4577528745989080 0.5018796221485596 0.1390167135746649

0.5068028987231479 0.2504235824180964 0.1394198870708072

0.5065850679067795 0.7507097891102908 0.1392311639190142

0.5554923550317392 -0.0006906949982616 0.1399675261226559

0.5552265332070725 0.4993253787571725 0.1391694087593199

0.6043382824953757 0.2485365480471437 0.1397797854820464

0.6034759114927853 0.7486604327332693 0.1399512410412951

0.6529849641214265 0.9968006820949270 0.1412596539945523

0.6528968925835009 0.4978365239864759 0.1389331730932306

0.7015254079006835 0.2474394446928243 0.1397496831206023

0.7002629857300179 0.7474620888747101 0.1399058681047632

0.7506979753602067 0.9950200839254875 0.1381839368194406

0.7508857610608652 0.4984284992838769 0.1405528346547955

0.7925868184014323 0.2464440688971917 0.1384704027773893

0.7932564934625077 0.7471076016945299 0.1389186729990960

0.2092489042454757 0.0946694648041198 0.0987527653307042

0.2180550609999484 0.5865708944129642 0.1009868632836846

0.2661780826525157 0.1648537641620614 0.1767556744695839

0.2690525733687152 0.6610208447371215 0.1797754449109663

0.2181127562736397 0.4260710162961330 0.1801041514784004

0.2139216119922844 0.9205955098775987 0.1829070617750664

0.3097327777903163 0.0785485884212830 0.0955005327969382

0.3085204435476455 0.5705941402292101 0.0948664479646645

0.2681282913369250 0.3502025427247756 0.1008565140086314
0.2666599375078982 0.8457203096463266 0.1032185881064744
0.3607108446537260 0.1654897820718505 0.1741003590564069
0.3612719763368685 0.6657579030874203 0.1735776350846303
0.3096250928627696 0.4391927915691015 0.1842717048125403
0.3138632527922713 0.9318892074211097 0.1837677700565849
0.4075060081380557 0.0756976631902943 0.0950214961910442
0.4075815387790457 0.5755274564193354 0.0943708588391997
0.3609871218054198 0.3421652086501624 0.1055468193616951
0.3613396430115396 0.8424726954012749 0.1048170624733016
0.4578665726220187 0.1636851957113825 0.1736593910708780
0.4576890127146458 0.6637385535294313 0.1732293789538785
0.4099124091092008 0.4321454279277377 0.1836299634710334
0.4111756541063019 0.9301678564294006 0.1835178426082544
0.5055465107083063 0.0726392168073376 0.0952164932421884
0.5048192573697426 0.5727910179725112 0.0945317939223363
0.4581602220829570 0.3391692284101153 0.1052671235471130
0.4584631743906262 0.8400806276050991 0.1047022411627949
0.5553203501126273 0.1619380841023224 0.1738914399199063
0.5545690273180242 0.6609464003895357 0.1736570440173329
0.5081860103455024 0.4288165781810250 0.1834828508743296
0.5078473705454415 0.9276622806589013 0.1839780738574110
0.6041018795724775 0.0696801486745614 0.0963833958534233
0.6019496230201445 0.5706879781329854 0.0948406984850336
0.5558807472004493 0.3366036348379702 0.1051925077592379
0.5554409891921847 0.8380297005864759 0.1053430960207585
0.6531618663461767 0.1606873123673719 0.1744904508404896
0.6516555492107809 0.6586242201721697 0.1739448970418219
0.6062588732424052 0.4262669258454166 0.1834948937788898
0.6043135285294897 0.9247625698247463 0.1851232903774823
0.7024604077657873 0.0668752587654539 0.0964898700889989
0.6996200903557536 0.5720206022199170 0.0951159140766702
0.6533917697198339 0.3343537945192018 0.1050747963725143
0.6519552366002963 0.8368334864596462 0.1058804702975731
0.7487505729838332 0.1541178449411239 0.1765839486179620
0.7462104952458454 0.6548079784703097 0.1778737695466688
0.7041629582249668 0.4249339748387175 0.1833604449978804
0.7014728832499529 0.9198299097275479 0.1849090621143286
0.7983066318739038 0.1113825154847125 0.0913648285354824
0.8006677399189472 0.5753270067806814 0.1031839101173616
0.7483076534763196 0.3396826435347376 0.1017091142788771
0.7457444897421756 0.8388902450206367 0.1007650107268278
0.8000930281859195 0.3815427255315042 0.1851784868053385
0.8018561448033029 0.9192507747537639 0.1737636547824168

0.2139105573160478 0.1018764970449991 0.0603487980936288
0.2313127363910049 0.6102841776201468 0.0665093089670632
0.3071780654045688 0.0527372219848693 0.0581632980452160
0.3068282151025822 0.5085353619822086 0.0646852623839002
0.2228909172517241 0.9140525762321913 0.2202575687121384
0.4049635094438540 0.0534012092060856 0.0573155800872531
0.4058746866814213 0.5518479893681452 0.0567383087545229
0.3155650657492486 0.9592971350620195 0.2210038645428586
0.5040159680729255 0.0479126056729378 0.0576742146540322
0.5026073350049904 0.5494299148814463 0.0569058685850395
0.4111261942228930 0.4603476296696061 0.2208107150318867
0.4132811811714253 0.9532681550259342 0.2211811792276673
0.6038175652566676 0.0428343969710484 0.0590254090469082
0.5994922571239710 0.5477555971591499 0.0571867244742920
0.5102362806406479 0.4542077013323062 0.2209209354762800
0.5094048506835867 0.9504110933820082 0.2217032094437203
0.7027656672954620 0.0261808316572019 0.0611326937285939
0.6978184887910961 0.5497905969134010 0.0573386013187930
0.6086687888531779 0.4502277681721821 0.2210506492720214
0.6047844452814919 0.9454968604055578 0.2230633625903325
0.7844988521542751 0.1380393354188633 0.0576543110546035
0.7945145573837767 0.5778356328624716 0.0649348834264781
0.7057115807596036 0.4603237243708535 0.2195442497825688
0.7011044993771082 0.9364731384697393 0.2231696835817325
0.7874150652568664 0.3553505798620497 0.2195765410754432
0.7968214029867683 0.9178919350992141 0.2122546149795639
0.2307421958786052 0.4039629265437469 0.2150481112788323
0.3084963005880786 0.4988581466512551 0.2152589997888640

LOM process: (O-O) CONTCAR

1.00000000000000
30.0000000000000000 0.0000000000000000 0.0000000000000000
0.0000000000000006 10.1043996811000003 0.0000000000000000
0.0000000000000015 0.0000000000000015 25.0000000000000000
Ni O H
26 52 26
Direct
0.2221380857653946 0.2479464816397141 0.1404821831771901
0.2218654130580479 0.7505357233235298 0.1415515233709211
0.2623705976984372 -0.0014459044705714 0.1367552255847817
0.2656462256695112 0.5022063063470267 0.1409098976415429
0.3113764899991581 0.2487594294166136 0.1402799211020342
0.3143589093755552 0.7556427765168255 0.1376590603765555
0.3609779571670426 0.0024728114627173 0.1381135963028134

0.3623442081047701	0.5051125247877102	0.1366574727815913
0.4086170723245146	0.2505192449819155	0.1400377986744490
0.4108216868664230	0.7542136382872261	0.1367689021199526
0.4585175389470209	0.0026234812426286	0.1387328794144040
0.4580350056933076	0.5026887470580583	0.1381973478752117
0.5062687359681703	0.2512265985734435	0.1398959964829286
0.5075039505220224	0.7517892033536833	0.1382782182377371
0.5557619276991795	0.0006237838909405	0.1399493794288635
0.5553795772495369	0.5006408135047018	0.1390683775935918
0.6039634531787554	0.2497955467379046	0.1399932003611761
0.6041721497630435	0.7497444369621873	0.1395614955708849
0.6532007570803158	0.9980022008701487	0.1413731415556200
0.6530057265280533	0.4996107722824325	0.1387435913162859
0.7012364243983228	0.2487987766839161	0.1397550847790002
0.7007995305731229	0.7486109826175799	0.1397993123513186
0.7508266518252148	0.9960693081310389	0.1382265944130495
0.7508994937378067	0.4997972052132459	0.1405501459678405
0.7922428041907370	0.2477492276131693	0.1385720348903577
0.7937240811066779	0.7480993143670318	0.1389601577968847
0.2082481537949798	0.0961550083216944	0.0983536796181836
0.2145800705947579	0.5744956944126435	0.1071505817165396
0.2672019415178824	0.1505417841268119	0.1765358936618006
0.2711915459569671	0.6607251512530536	0.1766034339363466
0.2416992432387954	0.4083669970749377	0.1964864672740028
0.2149412237993666	0.9163963909746558	0.1793756983699903
0.3100367032666128	0.0744128847635590	0.0940783664086232
0.3123433618926880	0.5598814496882437	0.0955216485674241
0.2664170240130622	0.3462175012502564	0.1017251183724524
0.2674581677861676	0.8406136253064147	0.0995395190231388
0.3602702963347205	0.1622763793773281	0.1743962437757007
0.3625882943562812	0.6657370798481799	0.1706380178567528
0.2884457975383687	0.4041678019509724	0.1976701147149884
0.3147126535836588	0.9251612204260068	0.1813609852620530
0.4077429106820514	0.0779741713921118	0.0945886288016533
0.4112160794200690	0.5752017228342486	0.0917675283412654
0.3595615775344295	0.3394551013116110	0.1072241336654281
0.3627146953007226	0.8425754662956383	0.1021474989571529
0.4575184952469807	0.1636972536106548	0.1740630834112071
0.4585423897171506	0.6648807977748797	0.1718425680041226
0.4058762029693029	0.4381283809465158	0.1834747215024436
0.4118133186218840	0.9294965500700001	0.1821139792016198
0.5054448895768879	0.0750376217408352	0.0952081973340541
0.5074652083518645	0.5732669443631873	0.0938900675527622
0.4571738604095794	0.3388688975498934	0.1058391882001850

0.4596904882991688 0.8418151649250726 0.1034135732472648
0.5550251815662471 0.1630615148977694 0.1742410309509111
0.5552884079433580 0.6621502810433798 0.1732355378824079
0.5055228449178746 0.4308999336646365 0.1833249304304083
0.5085650290878858 0.9284530500713070 0.1835355214137273
0.6036097849272222 0.0714322844234717 0.0964775597193238
0.6038843598383722 0.5726478719539619 0.0945133671206039
0.5552570297866016 0.3377653038138111 0.1055901165734891
0.5562812086324493 0.8396493758528389 0.1049462658341628
0.6530111764918325 0.1620409438472355 0.1745632376721045
0.6522050402770238 0.6597429437297504 0.1738675852271715
0.6046256145351842 0.4284752282947932 0.1832965069361314
0.6051288028473786 0.9261122404845721 0.1850959264003537
0.7020375412286767 0.0674769067514768 0.0967018611738645
0.7008848312151386 0.5747807018986401 0.0949473654348986
0.6530177590903767 0.3359396631198500 0.1052502878846427
0.6525470508865958 0.8383691595264346 0.1057821966106517
0.7484994092020818 0.1549847764405410 0.1765819566369231
0.7466233240039625 0.6559025525201573 0.1779479869990347
0.7032956990364931 0.4271396460445072 0.1830107259731889
0.7021914795782105 0.9199791481129960 0.1850001704144003
0.7978292255870935 0.1125130700726693 0.0913376291516464
0.8013844822139833 0.5759136164419824 0.1038040623015118
0.7480679513639032 0.3413807044277765 0.1017831112584391
0.7462765018804783 0.8402654881020920 0.1007332527608809
0.7992879435541311 0.3826473170858153 0.1855926817666062
0.8023479110326163 0.9205779549941242 0.1734892165764839
0.2128836649628960 0.1128997616234548 0.0604067105983057
0.2181604168792896 0.5713963738721193 0.0684072219487482
0.3083290260768072 0.0453145751798282 0.0570232786127330
0.3097828832363896 0.4965814684648204 0.0657877077960455
0.2241179221418143 0.9109124374894352 0.2166945275392892
0.4049481921162861 0.0603717941215163 0.0565210110905008
0.4124203792817388 0.5499617100533426 0.0542643968799926
0.3158138200644863 0.9465453594724350 0.2192644247412853
0.5032414168172040 0.0518497607498053 0.0575582655655969
0.5081538684503256 0.5495508677359272 0.0562272229735420
0.4038717801099627 0.4806953326896701 0.2184367463149212
0.4135127112884280 0.9519941356741202 0.2198764649744598
0.6026020115681251 0.0450003257718636 0.0590870312495977
0.6033050391945973 0.5505037648094611 0.0566973659448710
0.5049989796838940 0.4580614632180009 0.2206462892543018
0.5105473350041296 0.9512433338063949 0.2212388200812541
0.7019943752369620 0.0261719824795367 0.0614453877711654

0.6997881844690842 0.5551314171112436 0.0569188585074796
0.6053722134833174 0.4545297027029735 0.2207313306914444
0.6065116279550105 0.9469540155361065 0.2230066929293173
0.7840791983276432 0.1390986690833308 0.0575814542466317
0.7957869299607743 0.5774114867343225 0.0654267426266582
0.7044120812145600 0.4626386977043979 0.2192089799465370
0.7025629787292607 0.9345905376581751 0.2233891390580829
0.7865329247575873 0.3557617541234202 0.2198686087752343
0.7976970299696798 0.9195919955334516 0.2120477878338631

LOM process: (OO^* + OH^*) CONTCAR

1.0

30.0000000000 0.0000000000 0.0000000000

0.0000000000 10.1043996811 0.0000000000

0.0000000000 0.0000000000 25.0000000000

Ni O H

26 53 25

Direct

0.221245006 0.244042993 0.132419005
0.222645000 0.756717980 0.133846000
0.265107006 0.000000000 0.133812994
0.267224997 0.511762023 0.134075999
0.313757002 0.254732996 0.137254000
0.315728009 0.754750013 0.138362005
0.362538010 0.000000000 0.140153006
0.364021003 0.506758988 0.140880004
0.410872012 0.252332002 0.141745999
0.411053985 0.746994972 0.144783005
0.458718002 0.000000000 0.143941998
0.458869994 0.504593015 0.148715004
0.506582975 0.251931012 0.144206002
0.506488025 0.744035006 0.147540003
0.555396974 0.000000000 0.142542005
0.554008007 0.503793001 0.144994006
0.603164971 0.250425994 0.139925003
0.603084981 0.747937024 0.141966999
0.652265012 0.000000000 0.139059007
0.651982009 0.501972020 0.137656003
0.700707972 0.251197994 0.136972994
0.699721992 0.750635982 0.137759000
0.750110984 0.000000000 0.134682000
0.750061989 0.502871990 0.137408003
0.791787028 0.251282007 0.135087997
0.792689025 0.750850022 0.135137007

0.215629995	0.103069998	0.085807003
0.214256003	0.579335988	0.102435999
0.266306996	0.161411002	0.172263995
0.268743008	0.663918018	0.173921004
0.203707993	0.374004006	0.182686999
0.214505002	0.925375998	0.170705006
0.313389987	0.077522002	0.093101002
0.317330986	0.586969018	0.092083000
0.266864985	0.350255996	0.100059003
0.271277994	0.845551014	0.097337000
0.361018002	0.166973993	0.173978999
0.362179995	0.666886985	0.177172005
0.312025994	0.439823985	0.179856002
0.314419001	0.931738019	0.182368994
0.410587996	0.074598998	0.097120002
0.415116996	0.570137978	0.106201999
0.364235997	0.342379004	0.106578000
0.365476996	0.840171993	0.106973998
0.458768994	0.160074994	0.176934004
0.459690988	0.663707972	0.185352996
0.413078994	0.425747007	0.189689994
0.411587000	0.934265971	0.188012004
0.506947994	0.058804002	0.100185998
0.503688991	0.585650027	0.109417997
0.459933013	0.344974011	0.110541001
0.459681004	0.829285979	0.111253999
0.555687010	0.159714997	0.175852999
0.555620015	0.663134992	0.181215003
0.505074024	0.425063014	0.191229999
0.507620990	0.903015971	0.188728005
0.604049027	0.073186003	0.095779002
0.601068020	0.577875972	0.097108997
0.553331971	0.342121989	0.109231003
0.553417981	0.830100000	0.109155998
0.653257012	0.163898006	0.172763005
0.652319014	0.661449015	0.174037993
0.604488015	0.429827988	0.184048995
0.603110015	0.930800974	0.185622007
0.702103972	0.072332002	0.093392000
0.699141026	0.577979028	0.092969999
0.651449978	0.338775009	0.104037002
0.650044978	0.838262975	0.105246000
0.748418987	0.157805994	0.173377007
0.746190012	0.658980012	0.175120994

0.702908993	0.429771006	0.180546999
0.700348020	0.925478995	0.181797996
0.797864020	0.115689002	0.088156998
0.800180972	0.578969002	0.099863999
0.747209013	0.344668001	0.098618999
0.744643986	0.842472970	0.097686000
0.798771977	0.386763006	0.181958005
0.801108003	0.922802985	0.170149997
0.199401006	0.342693001	0.231918007
0.226209998	0.124940000	0.050021000
0.214730993	0.567876995	0.063786000
0.312474012	0.046145000	0.056311000
0.320068985	0.576770008	0.053606998
0.221318007	0.918175995	0.208681002
0.408228993	0.054765999	0.059161000
0.314354002	0.961561978	0.219353005
0.506285012	0.013906000	0.065585002
0.415241987	0.444606006	0.227789998
0.412858009	0.972693980	0.223691002
0.605401993	0.054777998	0.057658002
0.596993029	0.567224979	0.058821999
0.503278017	0.445327014	0.229204997
0.507408023	0.887157977	0.227100000
0.702699006	0.036674000	0.057216000
0.697134018	0.561986029	0.054729000
0.606172025	0.456050992	0.221440002
0.601734996	0.964814007	0.221999004
0.784694016	0.141870007	0.054026000
0.794346988	0.579828978	0.061547000
0.704335988	0.466351002	0.216545001
0.699774027	0.945603013	0.219796002
0.786418974	0.360092998	0.216464996
0.796424985	0.921555996	0.208691999
0.309248000	0.484504998	0.214328006

LOM process: (OH^* + OH^*) CONTCAR

1.0

30.0000000000	0.0000000000	0.0000000000
0.0000000000	10.1043996811	0.0000000000
0.0000000000	0.0000000000	25.0000000000

Ni	O	H
26	52	26

Direct

0.222250000	0.257041991	0.131565005

0.222259998	0.754317999	0.140226007
0.263395995	0.000000000	0.136772007
0.266440988	0.505432010	0.136775002
0.314437002	0.251691997	0.136684000
0.314401001	0.755457997	0.140587002
0.361833006	0.000000000	0.139792994
0.363685012	0.504769027	0.141977996
0.410795003	0.250138998	0.141599998
0.410120010	0.746928990	0.144203007
0.458162993	0.000000000	0.142716005
0.458261013	0.503704011	0.147701994
0.506305993	0.250308007	0.143298998
0.505693972	0.743143976	0.145904005
0.554857016	0.000000000	0.141152993
0.553453028	0.502878010	0.143609002
0.602882981	0.249173000	0.139198005
0.602392018	0.746834993	0.140599996
0.651669979	0.000000000	0.138479993
0.651284993	0.500729024	0.137103006
0.699998975	0.250041991	0.137202993
0.698760986	0.749520004	0.137762994
0.749369025	0.000000000	0.135414004
0.749288023	0.501519978	0.138354003
0.791136026	0.250158995	0.136664003
0.791863024	0.749873996	0.136593997
0.213297993	0.096808001	0.093229003
0.220311001	0.584329009	0.097163998
0.266943991	0.165018007	0.173374996
0.269046992	0.659479976	0.177689001
0.220585003	0.422526985	0.175656006
0.213842005	0.920136988	0.177589998
0.312813997	0.076862998	0.093928002
0.311749011	0.577901006	0.094975002
0.271593988	0.351419002	0.097161002
0.269026995	0.845044971	0.100984000
0.361259013	0.163788006	0.174142003
0.361544013	0.666257024	0.177193999
0.311432987	0.440820009	0.182211995
0.313823998	0.931623995	0.183024004
0.410046995	0.072984003	0.096516997
0.413776994	0.568302989	0.105784997
0.364365011	0.341717988	0.107074000
0.363815993	0.838284016	0.106741004
0.458793998	0.157376006	0.176257998

0.458963990	0.663516998	0.183976993
0.413042992	0.425022990	0.189696997
0.411038011	0.932510018	0.187085003
0.506431997	0.058713999	0.099105000
0.502704024	0.584821999	0.107896999
0.459562004	0.343589008	0.110058002
0.458664000	0.828534007	0.109823003
0.555405021	0.158216998	0.174778998
0.554823995	0.662361026	0.179582998
0.504814982	0.425365001	0.190052003
0.506964982	0.901979029	0.187107995
0.603805006	0.072145998	0.094791003
0.600359023	0.576653004	0.095807001
0.553085029	0.340777010	0.108374000
0.552783012	0.829132020	0.107597001
0.652460992	0.162095994	0.172379002
0.651183009	0.660202980	0.173337996
0.604001999	0.429170996	0.183173001
0.602195024	0.929114997	0.184474006
0.701824009	0.070913002	0.093346998
0.698585987	0.576168001	0.093048997
0.651085973	0.337633997	0.103642002
0.649589002	0.837351024	0.104438998
0.747240007	0.156664997	0.174232006
0.744808972	0.657875001	0.175764993
0.701942027	0.428602993	0.180992007
0.699191988	0.924044013	0.181894004
0.797640979	0.114220999	0.089860998
0.799618006	0.577826977	0.101543002
0.746810019	0.343472004	0.099515997
0.744095981	0.841385007	0.098424003
0.797733009	0.385803014	0.183626994
0.799813986	0.921746016	0.171805993
0.220021993	0.104961000	0.055294000
0.232823998	0.604939997	0.062024999
0.311174989	0.050205000	0.056625001
0.312243015	0.532630026	0.060421001
0.220670998	0.915506005	0.215616003
0.407651991	0.053890001	0.058515999
0.314361989	0.961163998	0.220025003
0.505863011	0.016733000	0.063946001
0.415499002	0.446532011	0.227546006
0.412353009	0.971639991	0.222636998
0.605741978	0.054195002	0.056669999

0.595888972	0.565617025	0.057592001
0.503651977	0.448688000	0.227789998
0.506285012	0.886116982	0.225483000
0.702969015	0.033776000	0.057413999
0.696419001	0.559553981	0.054846998
0.606015980	0.456559986	0.220413998
0.600486994	0.963027000	0.220849007
0.784578025	0.140415996	0.055675998
0.794282019	0.578200996	0.063116997
0.703262985	0.466226012	0.216838002
0.697768986	0.943449020	0.219934002
0.784694016	0.359055012	0.217761993
0.794489980	0.920623004	0.210233003
0.233448997	0.398086011	0.210229993
0.308961004	0.501672983	0.212755993

COM process: NR-NiOOH with one inner (O-O) coupling

1.0

30.0000000000	0.0000000000	0.0000000000
0.0000000000	10.1043996811	0.0000000000
0.0000000000	0.0000000000	25.0000000000

Ni	O	H
26	52	25

Direct

0.220951006	0.250414997	0.130767003
0.222591996	0.741819024	0.140561998
0.261426985	0.000000000	0.137860999
0.266465008	0.492352009	0.133802995
0.313066006	0.250672013	0.136779994
0.314166009	0.751730025	0.138501003
0.360989004	0.000000000	0.142038003
0.358592987	0.494130999	0.143326998
0.409837008	0.250593007	0.143049002
0.410310000	0.758284986	0.143462002
0.458602995	0.000000000	0.147131994
0.459071994	0.503566027	0.143821001
0.506869018	0.249460995	0.144824997
0.505057991	0.754176021	0.143994004
0.555276990	0.000000000	0.144371003
0.556023002	0.499002010	0.145506993
0.604349017	0.249439001	0.142783001
0.602217019	0.752349973	0.141396999
0.652702987	0.000000000	0.141073003
0.652042985	0.500235975	0.139442995

0.701412022	0.249813005	0.138503999
0.699340999	0.750406027	0.137867004
0.750530005	0.000000000	0.134893999
0.749987006	0.502116978	0.137482002
0.792378008	0.250900000	0.134821996
0.792522013	0.749848008	0.134692997
0.213117003	0.081656002	0.095296003
0.220659003	0.579672992	0.093952999
0.265949994	0.163211003	0.173756003
0.271189004	0.645717978	0.174435005
0.219614998	0.417986006	0.173217997
0.211641997	0.902706027	0.179354995
0.314038008	0.091706999	0.095891997
0.312049001	0.565805972	0.091835000
0.270570010	0.336066008	0.093872003
0.267816007	0.840923011	0.101039998
0.359898001	0.168210000	0.176635996
0.362361014	0.668703020	0.172459006
0.307217002	0.403032005	0.176330999
0.310755998	0.934746027	0.181492999
0.411013007	0.073113002	0.101102002
0.437029004	0.587701023	0.084619999
0.363523006	0.327987999	0.104271002
0.362922013	0.845250010	0.106462002
0.458541006	0.167721003	0.180682003
0.458153009	0.663926005	0.179552004
0.412485003	0.435876012	0.185378999
0.408392996	0.929966986	0.189471006
0.507673025	0.076853998	0.101420999
0.483617991	0.591355026	0.085970998
0.459814012	0.339657992	0.110555999
0.458925992	0.846835017	0.111093000
0.556538999	0.162986994	0.179120004
0.553656995	0.663478971	0.176021993
0.506850004	0.442905992	0.187673002
0.506875992	0.929654002	0.190461993
0.604717016	0.073053002	0.098719999
0.597971022	0.567731023	0.097071998
0.554854989	0.338867009	0.110688999
0.553286016	0.841055989	0.108663999
0.654326975	0.162549004	0.175353006
0.651175022	0.662078023	0.173506007
0.606927991	0.427940011	0.187304005
0.603493989	0.925836980	0.186866000

0.702279985	0.072746001	0.094686002
0.697448015	0.575369000	0.093576998
0.651973009	0.336576998	0.105989002
0.650081992	0.839505017	0.105503999
0.749572992	0.156920001	0.173925996
0.745934010	0.658630013	0.174862996
0.704117000	0.429190993	0.181828007
0.700976014	0.924139023	0.182532996
0.798110008	0.114967003	0.088021003
0.799106002	0.578428984	0.098773003
0.747129023	0.343288988	0.099086002
0.744364023	0.841959000	0.097703002
0.799902976	0.387171000	0.181133002
0.801563978	0.921267986	0.169652998
0.220742002	0.081166998	0.057447001
0.234548002	0.608223975	0.060509998
0.318037003	0.108062997	0.057817999
0.313154012	0.514859974	0.058607999
0.215642005	0.896107018	0.217852995
0.411554009	0.044966999	0.063890003
0.308398008	0.971616030	0.217426002
0.507210016	0.055249002	0.063548997
0.412351012	0.473881990	0.221269995
0.406502008	0.941758990	0.227965996
0.605041027	0.049279999	0.061037999
0.593711019	0.531726003	0.061246999
0.506026983	0.496149987	0.220382005
0.506811976	0.953055024	0.228158996
0.702511013	0.039329998	0.058164999
0.694848001	0.555750012	0.055635002
0.610204995	0.452960998	0.224649996
0.602428973	0.943463981	0.225034997
0.785053015	0.141075000	0.053833000
0.792738020	0.579945028	0.060580999
0.706640005	0.465932995	0.217712000
0.700345993	0.942992985	0.220642000
0.788514018	0.360834986	0.216143996
0.797366023	0.920792997	0.208279997
0.234555006	0.395958990	0.206971005

COM process: ($O^* + O^*$)

1.0

30.0000000000	0.0000000000	0.0000000000
0.0000000000	10.1043996811	0.0000000000

0.0000000000 0.0000000000 25.0000000000

Ni O H

26 52 24

Direct

0.224105000	0.254702002	0.137411997
0.225378007	0.740486026	0.139101997
0.262335002	0.000000000	0.138503999
0.265410006	0.492024988	0.136222005
0.314285010	0.250441998	0.138512000
0.315328002	0.750424981	0.138778999
0.361200988	0.000000000	0.141362995
0.358738005	0.494704992	0.143747002
0.411047995	0.249794006	0.142860994
0.411431998	0.754694998	0.142669007
0.458597004	0.000000000	0.145587996
0.458855987	0.502996027	0.144024998
0.507640004	0.249059007	0.144332007
0.505666018	0.754867017	0.143950999
0.555610001	0.000000000	0.143868998
0.556472003	0.498364002	0.145252004
0.604856014	0.249164000	0.142199993
0.602616012	0.751700997	0.140990004
0.653038979	0.000000000	0.140860006
0.652480006	0.500321984	0.138995007
0.701786995	0.249732003	0.138231993
0.699672997	0.750181973	0.137930006
0.750963986	0.000000000	0.134941995
0.750518978	0.502240002	0.137392998
0.792641997	0.250452995	0.134948000
0.792913973	0.749796987	0.134939000
0.215850994	0.096208997	0.098572999
0.215612993	0.589227974	0.097179003
0.266227007	0.156798005	0.175733998
0.268902004	0.652220011	0.176118001
0.222610995	0.403800011	0.172750995
0.206084996	0.888715982	0.173681006
0.314415008	0.072140001	0.095968001
0.311922014	0.572910011	0.094155997
0.268260986	0.340379000	0.095870003
0.267022014	0.839362025	0.100312002
0.361167014	0.164487004	0.176126003
0.362845987	0.668074012	0.173305005
0.307350993	0.419705003	0.178815007
0.308486015	0.924565017	0.182804003

0.412149996	0.076823004	0.099270999
0.436067998	0.588824987	0.085225001
0.363783985	0.331712991	0.105990998
0.363238007	0.839263976	0.105887003
0.458932996	0.166815996	0.180125996
0.458299011	0.664084017	0.179853007
0.411940008	0.435294986	0.185473993
0.407117009	0.930850983	0.187684000
0.508275986	0.076554000	0.100644998
0.482679009	0.590426028	0.085892998
0.459867001	0.339841992	0.110215001
0.458781987	0.845062017	0.110179000
0.556891024	0.163176998	0.178789005
0.553763986	0.666904986	0.176116005
0.505555987	0.440256000	0.187588006
0.506138980	0.930051029	0.189593002
0.605130970	0.072792001	0.098223999
0.599694014	0.570640981	0.096542001
0.555105984	0.334939986	0.109614998
0.553520977	0.840412021	0.108199999
0.654685020	0.162860006	0.175052002
0.651503026	0.661836982	0.173613995
0.607309997	0.426252007	0.186866000
0.603534997	0.926245987	0.186443999
0.702692986	0.072301000	0.094567999
0.698477983	0.576426029	0.093456000
0.652527988	0.336567998	0.105421998
0.650420010	0.838702977	0.105296999
0.749786973	0.156697005	0.174061000
0.746390998	0.658456028	0.175175995
0.704383016	0.429491013	0.181557000
0.701341987	0.923618019	0.182517007
0.798321009	0.114391997	0.088045001
0.799852014	0.578822017	0.098774999
0.747604012	0.343136996	0.098944001
0.744804978	0.842172980	0.097831003
0.800203025	0.386893988	0.181278005
0.801928997	0.921096027	0.170037001
0.224978998	0.108296998	0.061427999
0.224195004	0.605404019	0.060075000
0.317299008	0.048485000	0.058408000
0.312586993	0.540966988	0.057388000
0.200645998	0.881663024	0.211979002
0.415060014	0.059774000	0.061183002

0.305148989	0.943464994	0.220760003
0.509195030	0.058081001	0.062518001
0.412386000	0.470218003	0.221865997
0.404078007	0.951641977	0.225483999
0.605822027	0.050207000	0.060440999
0.596491992	0.541583002	0.059609000
0.504756987	0.489582002	0.221241996
0.505775988	0.952139020	0.227423996
0.703069985	0.038067002	0.058168001
0.695978999	0.559116006	0.055337001
0.611232996	0.447127014	0.224511996
0.602517009	0.943875015	0.224622995
0.784783006	0.140707999	0.054150999
0.792976022	0.581561983	0.060718998
0.706668973	0.467527986	0.217253998
0.700641990	0.942143023	0.220657006
0.788275003	0.360762000	0.216058999
0.797182977	0.919749975	0.208565995

COM process: (O-O)

1.0

30.0000000000	0.0000000000	0.0000000000
0.0000000000	10.1043996811	0.0000000000
0.0000000000	0.0000000000	25.0000000000

Ni	O	H
26	52	24

Direct

0.222019002	0.246527001	0.139939994
0.221765995	0.747416973	0.139755994
0.262167007	0.000000000	0.135881007
0.265161991	0.499687999	0.138612002
0.311125010	0.245277002	0.139401004
0.314496011	0.753014982	0.135597005
0.361119986	0.000000000	0.138800994
0.361162007	0.500926018	0.138876006
0.408953011	0.249577999	0.142312005
0.411489010	0.758337021	0.139102995
0.458808988	0.000000000	0.142261997
0.459493995	0.504226029	0.140845999
0.506464005	0.248992994	0.142160997
0.505957007	0.754310012	0.139972001
0.555518985	0.000000000	0.141310006
0.556227028	0.498216003	0.142848998
0.604182005	0.248026997	0.141182005

0.602922022	0.751358986	0.139603004
0.653023005	0.000000000	0.140942007
0.652261972	0.498344004	0.138870001
0.701363981	0.247736007	0.139253005
0.699904978	0.748673975	0.138738006
0.750860989	0.000000000	0.136915997
0.750223994	0.499662995	0.139374003
0.792348027	0.248309001	0.137358993
0.793058991	0.747653008	0.137631997
0.208311006	0.094346002	0.097852997
0.214102000	0.572305024	0.104638003
0.266918987	0.148402005	0.175950006
0.271144986	0.657876015	0.174785003
0.240436003	0.406614989	0.194187000
0.214229003	0.911814988	0.178320006
0.310968995	0.072797000	0.093842998
0.310658991	0.562434971	0.093666002
0.266530007	0.342211008	0.100139000
0.267304003	0.838328004	0.097879998
0.359887004	0.161134005	0.175536007
0.363579005	0.668416023	0.168494001
0.287328005	0.402765989	0.196034998
0.314074010	0.922447979	0.180198997
0.409471005	0.077832997	0.097450003
0.438603014	0.586974025	0.080697998
0.361027986	0.334158987	0.108891003
0.364250004	0.842267990	0.101934001
0.458306998	0.165327996	0.177707002
0.458810002	0.666167021	0.175569996
0.412874013	0.441437989	0.183748007
0.410892010	0.929332972	0.184889004
0.506541014	0.078474000	0.097607002
0.485172004	0.588854015	0.082892999
0.458855003	0.339417994	0.108934000
0.459731996	0.846943974	0.106376998
0.555821002	0.162076995	0.176499993
0.553825021	0.663295984	0.173044994
0.506895006	0.442086995	0.184934005
0.508328974	0.929754972	0.186065003
0.604103029	0.071158998	0.097296998
0.598909974	0.566094995	0.095063001
0.554964006	0.337805986	0.108328998
0.554670990	0.840426981	0.105517998
0.653605998	0.160172001	0.174863994

0.651024997	0.660310984	0.172940999
0.606396019	0.426573008	0.185741007
0.604619026	0.924212992	0.185204998
0.702230990	0.068887003	0.095962003
0.698507011	0.572982013	0.094237998
0.652529001	0.334470987	0.105469003
0.651455998	0.838397026	0.105058998
0.749044001	0.154596999	0.175702006
0.745746017	0.656108975	0.176631004
0.703538001	0.426515013	0.182633996
0.701689005	0.920637012	0.183699995
0.798147023	0.112452000	0.090475999
0.800135016	0.575941980	0.102026001
0.747703016	0.341066986	0.100786000
0.745523989	0.839761019	0.099476002
0.799349010	0.383960009	0.184044003
0.802071989	0.919414997	0.172171995
0.213189006	0.111592002	0.059994999
0.218823001	0.572703004	0.066055998
0.309816003	0.048870001	0.056200001
0.308914989	0.508287013	0.061268002
0.223252997	0.904677987	0.215630993
0.408389986	0.061283000	0.059172999
0.313933015	0.942088008	0.218254000
0.504315972	0.061576001	0.059447002
0.412425011	0.489710003	0.217630997
0.410360008	0.946259975	0.223132998
0.603211999	0.045942001	0.059767000
0.595283985	0.529578984	0.059220001
0.506143987	0.493184000	0.218172997
0.509703994	0.954725027	0.223578006
0.702242970	0.032719001	0.059841000
0.696731985	0.551934004	0.056352001
0.609254003	0.451837987	0.223107994
0.605108976	0.941120982	0.223444000
0.785109997	0.138870001	0.056306001
0.794605017	0.577235997	0.063648999
0.705417991	0.461955994	0.218777999
0.701472998	0.936361015	0.222029999
0.787299991	0.357201993	0.218695000
0.797865987	0.919735014	0.210789993

COM process: ($OO^* + OH^*$)

1.0

30.0000000000 0.0000000000 0.0000000000
0.0000000000 10.1043996811 0.0000000000
0.0000000000 0.0000000000 25.0000000000
Ni O H
26 53 25
Direct
0.222349003 0.245828003 0.131638005
0.221386999 0.748871982 0.138404995
0.262766004 0.000000000 0.136859998
0.267024010 0.504450977 0.134849995
0.313497007 0.248554006 0.138488993
0.314530998 0.752921999 0.138609007
0.361135006 0.000000000 0.142034993
0.360608011 0.498358011 0.142019004
0.410643011 0.249051005 0.143344000
0.410531998 0.757202029 0.143490002
0.458747000 0.000000000 0.145843998
0.459509999 0.503033996 0.143609002
0.507409990 0.248530999 0.144249007
0.505037010 0.753629029 0.143102005
0.555440009 0.000000000 0.143323004
0.556178987 0.498436987 0.144684002
0.604626000 0.249099001 0.142156005
0.602065980 0.751958013 0.140387997
0.652706981 0.000000000 0.140340999
0.652054012 0.500117004 0.138987005
0.701524019 0.249676004 0.138334006
0.699028015 0.750373006 0.137361005
0.750560999 0.000000000 0.134792000
0.749975979 0.502238989 0.137499005
0.792393982 0.250941008 0.135185003
0.792312980 0.749761999 0.134620994
0.215650007 0.094697997 0.091058001
0.218832001 0.583119988 0.095115997
0.264860004 0.158248007 0.173522994
0.269486010 0.655865014 0.175024003
0.212375000 0.390899003 0.176771998
0.210868999 0.913317025 0.175095007
0.313917994 0.072526000 0.095716000
0.317472994 0.572713017 0.090666004
0.268501014 0.344312996 0.098344997
0.268500000 0.840858996 0.099716999
0.360783011 0.164441004 0.176538005
0.362866998 0.670260012 0.174103007

0.308346987	0.429527998	0.183185995
0.310773998	0.926783025	0.183820993
0.412286997	0.074879996	0.100143000
0.436879992	0.586292982	0.084671997
0.363694996	0.329672009	0.106795996
0.363404989	0.841817975	0.106385998
0.459482014	0.166196004	0.180334002
0.458469987	0.663811028	0.179394007
0.413132995	0.436811000	0.185950994
0.408006996	0.930383980	0.188632995
0.508724988	0.076273002	0.100203000
0.483451009	0.590402007	0.085447997
0.460168004	0.338986009	0.110596001
0.458593011	0.845129013	0.110164002
0.556973994	0.162310004	0.178385004
0.553705990	0.663450003	0.175113007
0.507260978	0.442454010	0.187415004
0.506245017	0.928857982	0.189347997
0.605404019	0.073196001	0.097732998
0.598114014	0.567125022	0.096156001
0.555113971	0.338144004	0.109925002
0.553196013	0.840243995	0.107533999
0.654433012	0.162268996	0.174927995
0.650813997	0.662279010	0.172932997
0.606957018	0.427621990	0.186771005
0.602878988	0.925590992	0.185940996
0.702657998	0.073096000	0.094250999
0.697542012	0.575266004	0.093263999
0.652243018	0.336492985	0.105602004
0.649873972	0.839262009	0.104688004
0.749459982	0.156826004	0.174033001
0.745588005	0.659075022	0.174833998
0.703996003	0.429625988	0.181766003
0.700473011	0.924226999	0.182045996
0.798385024	0.115057997	0.088361003
0.799247980	0.578337014	0.098911002
0.747268021	0.343134999	0.099161997
0.744259000	0.841861010	0.097352996
0.799579978	0.386997014	0.181674004
0.801276982	0.920656979	0.170013994
0.215302005	0.377292007	0.228002995
0.223802000	0.094747998	0.053442001
0.231471002	0.606387973	0.060316999
0.316404998	0.046123002	0.058394998

0.316332996	0.524761975	0.056896001
0.215090007	0.907931030	0.213607997
0.414725006	0.053660002	0.062318999
0.307772011	0.951472998	0.221238002
0.509694993	0.055551998	0.062252998
0.413837999	0.478298992	0.221230999
0.404179990	0.947107971	0.226619005
0.606624007	0.049856000	0.060033999
0.593912005	0.530466020	0.060431998
0.506736994	0.496618003	0.219901994
0.504794002	0.952247977	0.227010995
0.703240991	0.040259998	0.057647001
0.694908977	0.555401981	0.055346999
0.610225976	0.452914000	0.224089995
0.600776970	0.943576992	0.224034995
0.785327971	0.141378999	0.054194000
0.792748988	0.579809010	0.060748000
0.706425011	0.467756003	0.217434004
0.699380994	0.944127023	0.220063001
0.787576020	0.360365003	0.216355994
0.796388984	0.918799996	0.208520994
0.302738994	0.474415988	0.217085004

COM process: (OH^* + OH^*)

1.0

30.0000000000	0.0000000000	0.0000000000
0.0000000000	10.1043996811	0.0000000000
0.0000000000	0.0000000000	25.0000000000

Ni	O	H
26	52	26

Direct

0.223680004	0.251273990	0.133587003
0.221454993	0.748652995	0.134578004
0.262928009	0.000000000	0.135672003
0.263814986	0.501677990	0.136950999
0.314523011	0.248512998	0.139392003
0.314731002	0.750908017	0.138753995
0.361624002	0.000000000	0.142912000
0.360451013	0.498317003	0.143124998
0.410843998	0.248834997	0.144130006
0.411204994	0.756327987	0.144250005
0.459172010	0.000000000	0.146529004
0.459787995	0.502637029	0.143831998
0.507628024	0.248361006	0.144789994

0.505721986	0.753614008	0.143617004
0.555923998	0.000000000	0.143787995
0.556569993	0.498302013	0.145061001
0.604951978	0.248993993	0.142484993
0.602707028	0.751828015	0.140862003
0.653223991	0.000000000	0.140766993
0.652478993	0.499893010	0.139170006
0.701901019	0.249532998	0.138358995
0.699654996	0.750029027	0.137701005
0.751012027	0.000000000	0.134845003
0.750442982	0.501784027	0.137443006
0.792786002	0.250591993	0.134821996
0.792859972	0.749514997	0.134774998
0.209116995	0.107943997	0.092455000
0.216793999	0.582028985	0.094598003
0.265419006	0.159220994	0.174309000
0.267616004	0.657224000	0.175311998
0.206478998	0.394012004	0.173927993
0.212329000	0.916701019	0.171949998
0.312525988	0.072031997	0.096234001
0.316711009	0.577479005	0.094213001
0.269286007	0.340894014	0.098618999
0.269685000	0.841207027	0.098047003
0.361110002	0.163499996	0.177612007
0.363413990	0.669669986	0.175283000
0.308521003	0.424771011	0.183530003
0.312213004	0.923812985	0.183375999
0.411219001	0.074234001	0.101200998
0.437400997	0.586499989	0.084707998
0.364266008	0.330395997	0.107352003
0.364427000	0.840196013	0.106894001
0.459589988	0.166117996	0.180950001
0.459015995	0.663357973	0.179738998
0.413221002	0.437507004	0.186188996
0.409860998	0.928512990	0.189680994
0.508257985	0.076287001	0.100992002
0.483985007	0.590080023	0.085694999
0.460278004	0.338382006	0.110982001
0.459174007	0.844660997	0.110706002
0.557286978	0.162310004	0.178841993
0.554259002	0.663456976	0.175587997
0.507441998	0.442140013	0.187638998
0.507640004	0.928027987	0.189829007
0.605416000	0.072906002	0.098270997

0.598564982	0.567475975	0.096551999
0.555366993	0.337619007	0.110316001
0.553865016	0.840232015	0.107964002
0.654835999	0.162246004	0.175154999
0.651417971	0.661846995	0.173286006
0.607393980	0.427289993	0.187004000
0.603950977	0.925109982	0.186384007
0.702892005	0.072438002	0.094420001
0.697881997	0.575034976	0.093372002
0.652496994	0.336151987	0.105724998
0.650511026	0.839075983	0.105088003
0.749929011	0.157120004	0.173941001
0.746206999	0.658427000	0.174940005
0.704505026	0.428975999	0.181795999
0.701273978	0.923797011	0.182429001
0.798528016	0.115065001	0.087990001
0.799564004	0.578266025	0.098705001
0.747550011	0.342527986	0.098968998
0.744760990	0.841440976	0.097571000
0.800302029	0.386375993	0.181210995
0.801922023	0.920837998	0.169901997
0.211780995	0.125411004	0.054246999
0.227588996	0.593546987	0.058139998
0.313008010	0.043841001	0.059018999
0.318300009	0.557446003	0.056244001
0.218499005	0.910842001	0.210116997
0.411974013	0.053865999	0.063196003
0.311666012	0.939132988	0.221726999
0.508239985	0.057052001	0.062910996
0.413778007	0.481505990	0.220973000
0.408003002	0.944260001	0.227926999
0.606046975	0.049619999	0.060547002
0.594443977	0.532332003	0.060580999
0.506783009	0.495889992	0.220239997
0.507373989	0.949908018	0.227669001
0.703109980	0.038300999	0.058005001
0.695226014	0.555198014	0.055461999
0.610714018	0.451972991	0.224377006
0.602505028	0.942366004	0.224559993
0.784913003	0.141259998	0.054118000
0.792770982	0.580780983	0.060616001
0.706927001	0.466547996	0.217556998
0.700381994	0.943340003	0.220471993
0.788269997	0.359921992	0.215911999

0.797155023 0.919353008 0.208434001
0.304183990 0.451788992 0.220507994
0.207716003 0.374666989 0.212098002

(O^*+O^*) in Fig. S27

1.0

30.0000000000 0.0000000000 0.0000000000
0.0000000000 10.1043996811 0.0000000000
0.0000000000 0.0000000000 25.0000000000

Ni O H
26 52 24

Direct

0.225125000 0.263437986 0.136540994
0.223115996 0.747923970 0.140680999
0.263013989 0.000000000 0.139153004
0.268112004 0.498706013 0.133249000
0.315384001 0.256718010 0.135799006
0.314480990 0.751011014 0.139332995
0.361831009 0.000000000 0.141051993
0.363261014 0.498849988 0.138816997
0.410982996 0.249775007 0.140989006
0.409498990 0.743878007 0.144338995
0.457760006 0.000000000 0.144203007
0.457982004 0.502514005 0.147745997
0.506090999 0.249519005 0.143639997
0.505423009 0.741764009 0.147040993
0.554467976 0.000000000 0.142221004
0.553089023 0.501859009 0.144341007
0.602500021 0.248928994 0.139597997
0.602140009 0.746111989 0.141436994
0.651363015 0.000000000 0.138859004
0.651189983 0.500424981 0.137318999
0.699989974 0.249982998 0.137079000
0.698819995 0.749405980 0.137829006
0.749256015 0.000000000 0.135188997
0.749284029 0.501909018 0.137895003
0.791095972 0.250449985 0.136031002
0.791827023 0.750191987 0.136007994
0.214077994 0.106101997 0.099183999
0.220736995 0.584379017 0.095399000
0.268151999 0.171084002 0.175179005
0.270617008 0.649159014 0.175059006
0.226076007 0.412499994 0.172022000
0.213523000 0.912653983 0.178636000

0.313423991	0.094352998	0.096419998
0.313964009	0.581371009	0.091678001
0.271669000	0.340218991	0.093819000
0.268633991	0.848288000	0.102020003
0.361097008	0.169554994	0.174655005
0.360837996	0.661270976	0.175763994
0.313551992	0.416321009	0.172266006
0.312907010	0.935196996	0.182572007
0.409741014	0.070023000	0.097423002
0.413969994	0.568625987	0.105401002
0.364877999	0.334764987	0.102675997
0.363467008	0.840245008	0.107612997
0.458200991	0.157940000	0.176780000
0.458716989	0.660498977	0.184744000
0.412214994	0.421826988	0.187775001
0.410246015	0.930060983	0.188399002
0.505954981	0.057255000	0.100147001
0.502678990	0.584116995	0.108639002
0.459517986	0.342004001	0.109481998
0.458382994	0.827055991	0.111134000
0.555018008	0.157892004	0.175578997
0.554627001	0.660979986	0.180478007
0.504194021	0.423335999	0.190303996
0.506590009	0.900638998	0.188438997
0.603209972	0.071363002	0.095454000
0.600183010	0.575843990	0.096556000
0.552617013	0.340310007	0.108682998
0.552357018	0.828356981	0.108719997
0.652356982	0.162461996	0.172576994
0.651289999	0.659882009	0.173682004
0.603690982	0.428501993	0.183485001
0.602038980	0.928837001	0.185317993
0.701466978	0.071374997	0.093555003
0.698423028	0.576506019	0.093020998
0.650824010	0.337136000	0.103739999
0.649195015	0.836750984	0.105021998
0.747437000	0.156997994	0.173910007
0.745083988	0.658086002	0.175530002
0.701964021	0.428433001	0.180603996
0.699176013	0.924331009	0.181879997
0.797478974	0.114644997	0.089293003
0.799515009	0.578351974	0.100846998
0.746694028	0.343605995	0.099118002
0.743924022	0.841544986	0.098158002

0.797877014	0.386049986	0.182831004
0.799898982	0.921941996	0.171214998
0.220565006	0.116379000	0.061195999
0.233247995	0.609790981	0.060784001
0.313152999	0.104736999	0.057714000
0.314283997	0.560043991	0.053695999
0.217853993	0.907088995	0.217145994
0.407523006	0.043467000	0.060112000
0.312703013	0.966633022	0.219435006
0.505638003	0.014818000	0.065067999
0.411466986	0.443529010	0.225714996
0.411742985	0.963864982	0.224822000
0.604833007	0.053096000	0.057333998
0.596144974	0.565638006	0.058223002
0.501864016	0.443859994	0.228240997
0.506232023	0.884302020	0.226787999
0.702486992	0.036630999	0.057247002
0.696579993	0.560122013	0.054788999
0.605262995	0.454609990	0.220901996
0.600558996	0.962925017	0.221682996
0.784848988	0.140837997	0.054889999
0.794131994	0.578877985	0.062433001
0.703225970	0.464489013	0.216694996
0.698212981	0.944319010	0.219883993
0.785537004	0.359571010	0.217354000
0.794977009	0.920939028	0.209716007